Development of Cell-Based Neurotransmitter Fluorescent Reporters (CNiFERs) for In Vivo Detection of Somatostatin

by
Macit Emre Laçin

A dissertation submitted to the Graduate Faculty of the Graduate School of Biomedical Sciences, Neuroscience Doctoral Program, in partial fulfillment of the requirements for the degree of Doctor of Philosophy, Icahn School of Medicine at Mount Sinai

2019

This manuscript has been read and accepted by the Graduate Faculty of the Graduate School of Biomedical Sciences, in satisfaction of the dissertation requirement of the degree of Doctor of Philosophy.

Paul A. Slesinger

Dissertation Advisor — Paul A. Slesinger

9/24/2019

Date

Marta Filizola

Dean — Marta Filizola

10/28/19

Date

Examination Committee:
Dr. Lakshmi Devi
Dr. Graham Ellis-Davies
Dr. Hirofumi Morishita
Dr. Bernardo Rudy

Icahn School of Medicine at Mount Sinai

Abstract

Development of Cell-Based Neurotransmitter Fluorescent Reporters (CNiFERs) for *in vivo* Detection of Somatostatin

by
Macit Emre Laçin

Advisor: Paul A. Slesinger

Neuropeptides form a large group of transmitter molecules involved in diverse biological functions including sleep, reward, feeding, learning and memory. Investigation into the specifics of neuropeptide release *in vivo*, such as timing and location, has been a challenge due to lack of *in vivo* detection methods for neuropeptides. Microdialysis is currently the only available option to monitor neuropeptide levels.

Cell-based neurotransmitter fluorescent reporter (CNiFER) is an alternative method for *in vivo* detection of neuropeptides with high spatial and temporal resolution. The method relies on human embryonic kidney (HEK) cells that are genetically modified to express (1) a G-protein coupled receptor (GPCR) specific for the neuropeptide of interest and (2) a fluorescent calcium (Ca^{2+})-sensor. CNiFER converts neuropeptide binding into a fluorescence signal which can be detected by microscopy.

Somatostatin (SST) is a neuropeptide which has been used as a molecular marker to classify a group of interneurons in the cortex. However, studies in other parts of the brain suggested SST can be released into the extracellular medium and function as a neurotransmitter. In the present study, CNiFER clones were developed with physiological level sensitivity to SST. One of these clones was used to show that endogenous SST can be released by optogenetic stimulation of cortical somatostatin-expressing interneurons (SST-INs). Subsequent experiments revealed that the amount of SST released

was dependent on the frequency of light delivery. A second CNiFER clone was used to show SST can also be released by cholinergic stimulation of SST-INs.

In conclusion, in vivo application of SSTR2 CNiFER clones demonstrated that SST is not only a molecular marker that define a group of cortical interneurons but can be released into the extracellular medium by direct (optogenetic) or indirect physiological (cholinergic) stimulation of SST-INs. Application of CNiFER methodology to neuropeptides can help study into neuropeptide transmission in vivo.

Acknowledgement

I would like to acknowledge the contributions of Erin Aisenberg, Tyler Kern and Marian Fernando for the development and in vitro characterization of SSTR2 CNiFER clones (Chapter 2). Marian Fernando generated and characterized the SSTR2.46 CNiFER in vitro. This work involved lentiviral transduction of HEK cells with TN-XXL, Gqi5 adapter, and SSTR2, and subsequent antibiotic selection, single-cell sorting, and plate reader screening. Plate reader tests of SSTR2.46 CNiFER with somatostatin and non-specific agonists were performed by Marian (Fig.2.2B). Erin Aisenberg developed and characterized the control (Gqi5 Tw2B UR1D6 pre-CRiSPR) and SSTR2.6 (pre-CRiSPR) CNiFERs in vitro. This worked involved lentiviral transduction of HEK cells with Gqi5 adapter, Tw2B, and SSTR2, and subsequent antibiotic selection, single-cell sorting and plate reader screening. Plate reader tests of control (Gqi5 Tw2B UR1D6 pre-CRiSPR) and SSTR2.6 (pre-CRiSPR) CNiFERs with somatostatin and non-specific agonists were performed by Erin (Fig.2.2A, Fig.2.3). Tyler Kern developed and characterized the control 128C3 (HM4 CRiSPR-edited) and SSTR2 5F3 (HM4 CRiSPR-edited) CNiFERs. This work involved CRiSPR-editing HM4 receptor in control (Gqi5 Tw2B UR1D6 pre-CRiSPR) CNiFER and subsequent lentiviral transduction with SSTR2, selection, single-cell sorting, and plate reader screening (Fig.2.4). Plate reader tests of control 128C3 (HM4 CRiSPR-edited) and SSTR2 5F3 (HM4 CRiSPR-edited) CNiFERs with somatostatin and non-specific agonists were performed by Tyler (Fig.2.4, Fig.2.5). In vitro perfusion test of SSTR2 5F3 (HM4 CRiSPR-edited) CNiFER with somatostatin was performed by Tyler (Fig.2.6). The plots in Chapter 2 were generated by Marian (Fig.2.2B), Erin (Fig. 2.2A, 2.3), and Tyler (Fig.2.4, Fig.2.5, and Fig.2.6).

Table of Contents

Figures

Chapter 1: Introduction and Background

Neuropeptide Transmission Has Unique Features

Neuropeptides are molecules that can function as a neurotransmitter in the nervous system[1]. Neuropeptides typically signal through G protein-coupled receptors (GPCRs), which have a slower time course than ionotropic receptors[1]. While postsynaptic voltage changes follow glutamate release by milliseconds, postsynaptic responses to neuropeptides are on the order of seconds to minutes[1]. Neuropeptides can affect excitatory and inhibitory synaptic neurotransmission by increasing/decreasing presynaptic transmitter release or modulating the response of postsynaptic receptor to a transmitter[2]. Neuropeptides can also change neuronal excitability by acting on multiple channels and receptors to induce depolarization or hyperpolarization of the membrane potential[2].

In contrast to amino acid neurotransmitters (glutamate and GABA), which are generated at the site of release, neuropeptides are produced in the cell body[1]. Neuropeptide production begins as an inactive precursor (preprohormone) on the rough endoplasmic reticulum (ER)[3]. Precursor protein is converted into a prohormone by the cleavage of signal sequence[3]. Prohormone is then transferred to the Golgi apparatus, where it is targeted to regulated secretory pathway in a large dense core vesicle (LDCV)[3] LDCV travels to the release site on a microtubule track driven by motor proteins[4]. During this travel prohormone is converted to the physiologically active form of the neuropeptide by multiple enzymatic modifications [3](Fig1.1).

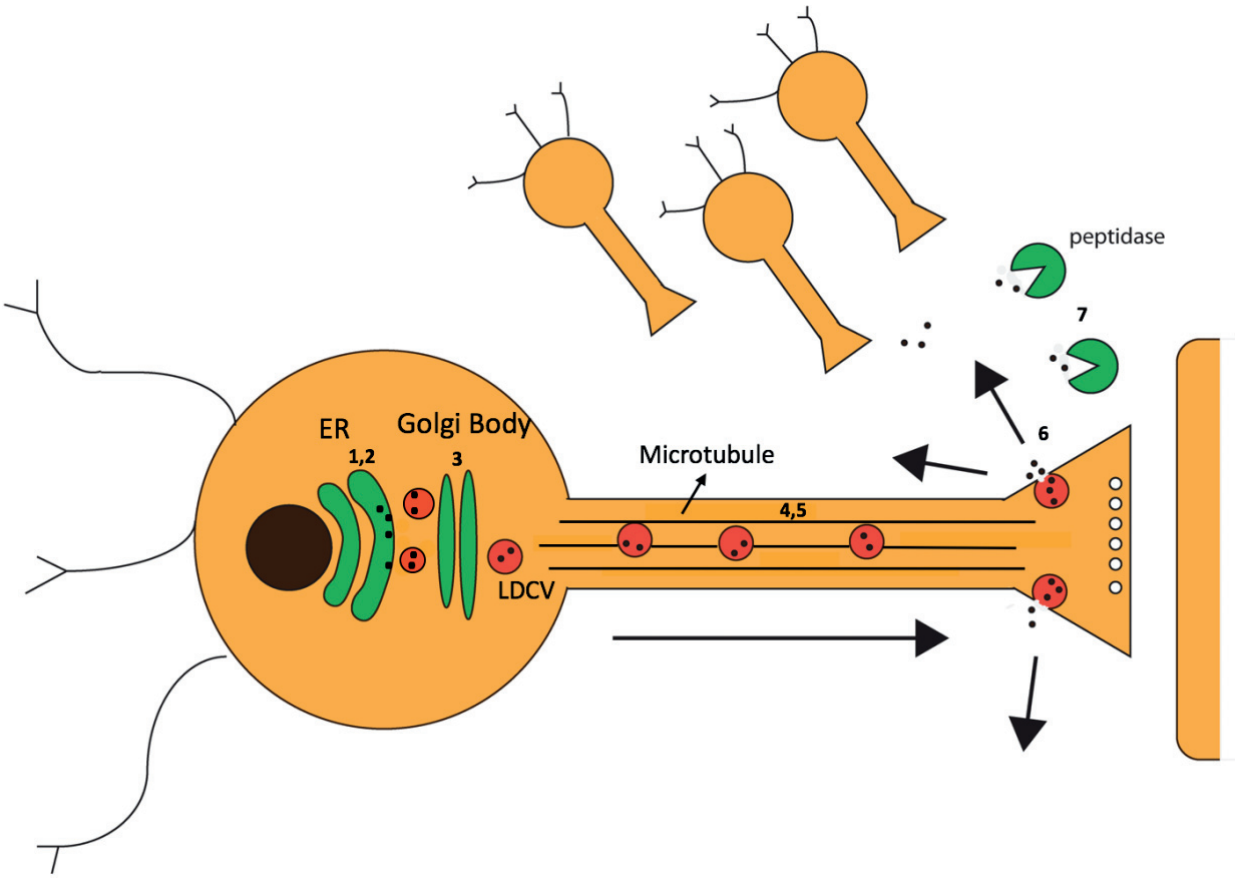

Fig.1.1 Neuropeptide synthesis, trafficking and release are depicted. (1) Neuropeptide is synthesized on the rough endoplasmic reticulum (ER) as an inactive precursor molecule (preprohormone). (2) Precursor molecule is converted into a prohormone by the cleavage of ER-targeting signal sequence. (3) Prohormone is transferred to Golgi Body, where it targeted to regulatory secretory pathway in a large dense core vesicle (LDCV). (4) LDCV travels to its cellular destination along the microtubule track driven by kinesin motor proteins. (5) Prohormone is converted into a physiologically active neuropeptide during this vesicular transport. (6) Neuropeptides are released away from the synaptic terminal and (7) degraded by peptidases[3, 4].

Neuropeptide exocytosis is not restricted to the synaptic terminal but occurs from all parts of a neuron, including cell body, dendrites, axonal shafts and axonal boutons[5]. The extra-synaptic localization of LDCVs raises questions on the nature of neuropeptide signaling, particularly how far neuropeptides travel through the extracellular space[1]. Minute-long half-lives of the neuropeptides and high-affinity of the neuropeptide receptors to the ligands (K_d ~

nM) suggest that neuropeptides signal through volume transmission and can act on extra-synaptic targets located several micrometers away[1]. However, other findings suggest local diffusion is more plausible than volume transmission[1]. The low frequency of neuropeptide-containing LDCVs in axons and hours it would take to replenish the pool of LDCVs makes it unlikely that neuropeptides ever reach concentrations to affect neurons located farther than the neuron immediately releasing the neuropeptide [1]. Moreover, anatomical studies showing confinement of axo-dendritic synaptic complexes by astrocytic processes further support to the local diffusion hypothesis[1].

CNiFERs Allow Real-Time Monitoring of Neuropeptides in the Brain

Monitoring the release of neuropeptides in real-time in awake animals is critical for elucidating when and where neuropeptides are released and how they affect neural circuits in the brain. Currently, there is no method to monitor release of neuropeptides in real-time. Although real-time analysis is not possible, microdialysis allows the measurement of neuropeptide levels in vivo[6]. With this method, a microdialysis probe with a semipermeable membrane at its tip is inserted into the brain and ACSF is perfused through a probe[6]. Molecules in the tissue surrounding the probe diffuse across the membrane into the perfusion medium and collected for later analysis [6]. Although microdialysis allows neuropeptide detection *in vivo*, its temporal resolution is not high[6]. Sampling time is typically on the on the order of minutes [6].

Recently, an optical cell-based method for in vivo detection of transmitters has been developed with high temporal resolution [7-9]. The method relies on a cell-based

neurotransmitter fluorescent engineered reporter (CNiFER), which is developed by genetic modification of human embryonic kidney cells (HEK293) to express a G-protein coupled receptor specific for the molecule of interest and a genetically encoded Ca^{2+}-sensor[7, 8]. The method takes advantage of phospholipase C/inositol trisphosphate (PLC/IP3) pathway and the $Ca2^{+}$-sensor for translating GPCR activation to an optically detectable signal: binding of the agonist to the GPCR induces an increase in intracellular Ca^{2+} through the PLC/IP3 pathway, and the increase in Ca^{2+} leads to a change in fluorescence signal of the Ca^{2+} sensor [7, 8] (Fig1.2). Thus, CNiFER converts agonist binding into a fluorescence signal that can be detected by microscopy.

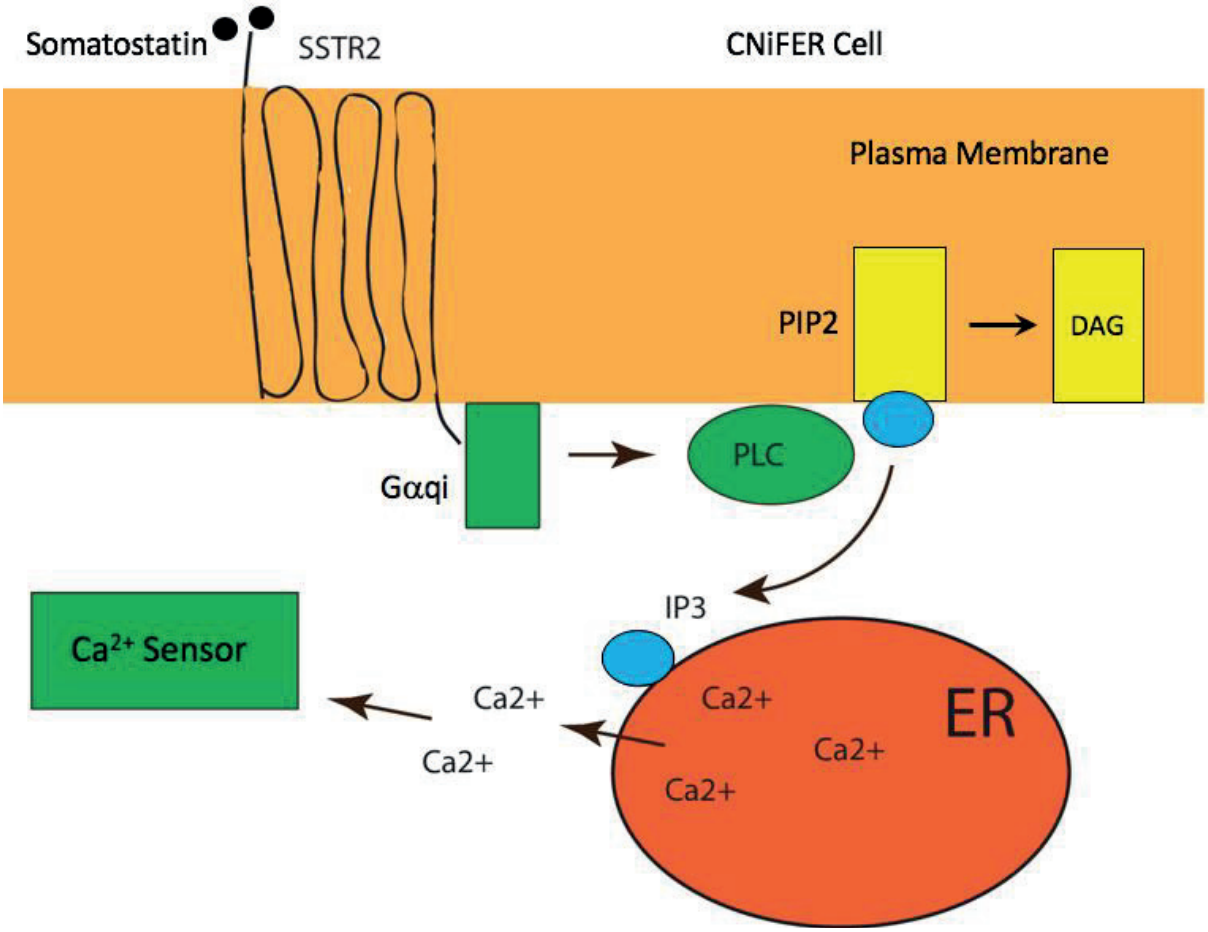

Fig 1.2 Cartoon showing how a CNiFER works. Somatostatin receptor 2-expressing CNiFER that

allows somatostatin (SST) detection is given as an example. SST binding to the SSTR2 activates phospholipase C (PLC) enzyme. PLC hydrolyzes phosphatidylinositol 4,5-bisphosphate (PIP_2) into inositol trisphosphate (IP_3) and diacylglycerol (DAG). IP_3 then diffuses through the cytoplasm and opens Ca^{2+} channels in the ER. This increases intracellular Ca^{2+} level and leads to a fluorescent signal from the Ca^{2+}-sensor[10]. For Gi/o-coupled GPCRs (e.g. SSTR2), an adapter Gq protein is required to redirect GPCR signaling to PLC/IP3 pathway. This is discussed later in the text.

A typical CNiFER surgery involves opening a cranial window through which the CNiFERs are injected[9]. This window is then sealed with a cover glass for chronic imaging[9]. A head-bar is cemented on the skull to fix the animal's head during imaging[9]. Imaging, which starts the day after surgery for chronic experiments, animal is mounted on a frame and imaged under two-photon laser-scanning microscopy (2PLSM)[9].

Somatostatin, Somatostatin Receptors and Somatostatin-Expressing Interneurons

There are over 100 neuropeptides encoded in the genome [11]. When a neuropeptide CNiFER was being developed, somatostatin (SST) stood out as a good candidate for detection because it localizes to the cortex making it accessible with two-photon microscopy and the neurons expressing SST make up 30% of interneurons —one of the largest neuropeptide-expressing cell types in the cortex[12].

SST-14 and SST-28 are two active forms of somatostatin and are produced by enzymatic cleavage of 92 amino acid long pro-peptide[13]. The two forms are generated in variable amounts by different SST-producing cells[13]. In the brain, SST-14 predominates, making up 70-80% of total SST[13]. Five receptor subtypes (SSTR1-5) have been identified which bind to SST-14 and SST-28 with nanomolar affinity (SSTR1-5)[13]. SSTR subtypes show similar affinity to SST-

14 and SST-28, except for SSTR5, which binds to SST-28 more tightly[13].

In the brain, specific SSTR subtypes are enriched in the cortex and show layer-specific expression[13]. Hybridization/nuclease protection analysis with cRNA probes specific to SSTR subtypes (SSTR1-5) revealed that all SSTR mRNAs, except for SSTR5 mRNA, are expressed in the cortex[14]. The same study showed SSTR1 and SSTR2 mRNAs are found at a higher level than SSTR3 and SSTR4 mRNAs [14]. Immunohistochemical (IHC) mapping of three receptors demonstrated layer-specific distribution SSTR subtypes in the rat cortex. SSTR1 and SSTR2-positive neurons were identified in layers 2/3, 5 and 6; while SSTR3 mainly localized to layers 5 and 6[13].

SST modulates excitatory and inhibitory transmission in two ways: (1) by affecting presynaptic neurotransmitter release and (2) by modulating excitability of the postsynaptic neuron [2]. Studies have shown SST can inhibit presynaptic release of both glutamate and GABA[15, 16]. For instance, SST reduces recurrent excitation between CA3 neurons in an *in vitro* model of epilepsy by depressing glutamate release from the presynaptic terminals[15]. However, SST was also shown to block inhibitory transmission by suppressing presynaptic GABA release in rabbit CA1 hippocampal slices[16]. SST can also influence neurotransmission via modulation of postsynaptic neuron excitability[17]. Superfusion of hippocampal slices with SST hyperpolarizes pyramidal cells and reduces pyramidal cell spontaneous firing rate[17]. Studies that follow showed that SST inhibits neurons by increasing voltage-sensitive and insensitive K^+ currents (M-, K^+-leak-, and GIRK- currents), and inhibiting N-type Ca^{2+}-current [18-21].

Neuropeptide release has been demonstrated to occur in all parts of the cell: cell body, dendrites, axonal shaft and boutons [5]. As neuropeptide-containing LDCVs are located away

from the synaptic active zone, a specialized structure enriched in voltage-gated Ca^{2+} channels, neuropeptide release is thought to require repetitive action potentials [2, 22]. However, neuropeptide release can also occur by an increase in intracellular $Ca2^{2+}$ levels not coupled to a change in firing rate [23]. SST release in the brain has been evidenced in previous studies[24-26]. Somatostatin-expressing hypothalamic cells spontaneously release SST through tonic firing [24]. Glutamate can increase this SST release by increasing intracellular Ca^{2+} level[25, 26]. GABA, in contrast, decreases basal release of somatostatin[24, 25].

Neuropeptide release from the LDCV is slower than low-molecular weight neurotransmitter release from small clear vesicles as large neuropeptides cannot diffuse through the fusion pore [27]. Moreover, once released, low-molecular weight neurotransmitters are rapidly cleared out from the extracellular medium on a timescale of milliseconds by transporters [28]. A reuptake mechanism does not exist for neuropeptides[1]. Rather, neuropeptides are inactivated by extracellular peptidases[1]. Peptide half-lives vary depending on the size, presence of disulfide bonds, amidation, and chemical conformation of the neuropeptide[1]. Moreover, medium affects the half-life of a neuropeptide. For instance, oxytocin's half-life in cerebrospinal fluid (CSF) is longer than its half-life in blood plasma (~19min in CSF vs ~3min in blood plasma) [29, 30]. SST's half-life in CSF has not been studied, but it can be longer than its 1.5-3 min half-life in blood plasma[31].

SST is almost exclusively found in interneurons and co-expressed with GABA[32, 33] . Besides GABA, SST interneurons (SST-INs) can express neuropeptide (neuropeptide Y (NPY), cholecystokinin (CCK), calcitonin gene-related peptide (CGRP), cortistatin, vasointestinal polypeptide (VIP), enkephalin) and gaseous (nitric oxide) neurotransmitters[34-38]. A Subset of

SST-INs co-express markers that are Ca^{2+}-binding proteins, such as calretinin and calbindin[37, 39].

Morphological characteristics, electrophysiological properties, input-output relationships and chemical markers are in general used to classify SST-INs. Three transgenic mouse lines generated by injection of GAD67-GFP vector into mouse eggs and subsequent implantation have been particularly helpful in classification of SST-INs[40, 41]. The three lines that resulted, X94, X98, and GIN, mark different subsets of SST-INs that show well separation along the cortical layers and complement each other[40]. While in X94 mice GFP+ neurons are located in layers 4 and 5b, GFP+ neurons are found in layers 5b and 6 in X98[40]. In GIN mice, on the other hand, SST-INs in supragranular layers (layers 2/3) and layer 5a are marked[40]. In terms of morphology, X98 and GIN SST-INs are Martinotti-type, with axons projecting and branching in layer1[40]. In contrast, X94 SST-INs do not have projections to layer1, rather, innervate layer 4[40]. Current clamp recording of these neurons revealed that X94 and X98 SST-INs have distinct electrophysiological characteristics, and GIN neurons is an intermediate between the two[40]. X94 SST-INs had lower input resistance, narrower spikes than X98 and GIN neurons, and tended to show a stuttering firing pattern[40]. X98 neurons were distinct from X94 and GIN neurons by the triphasic waveform that follows an action potential that results from fast and late hyperpolarization-activated currents (Ih)[40]. Although SST-INs in all three lines showed a sag at the beginning and a depolarizing rebound at the end of a hyperpolarizing current step, as a result of Ih current, X94 and GIN neurons rarely displayed rebound spikes while half of X98 did[40]. Subsequent experiments have shown that the

rebound spikes are associated with T-type calcium channels, rather than Ih current mediated by HCN channels, which led to classify these cells as low-threshold spiking (LTS) cells[40].

Martinotti-type SST-INs can be further subdivided into two groups based on axonal morphology: T-shape Martinotti type SST-INs innervate layer1, whereas fanning-out Martinotti cells have a broad axonal domain in layer 2/3 and lower half of layer1[42, 43]. In layer 5, the layer in which SST-INs are most abundant, T-shaped Martinotti, fanning-out Martinotti cells, and non-Martinotti cells make up ~10%, ~50% and ~40% of SST-INs, respectively[44]. T-shaped Martinotti, fanning-out Martinotti, non-Martinotti cells roughly overlap with the SST-INs previously identified in X94, X98, and GIN mouse lines[44]. T-shaped Martinotti show rebound spikes in response to hyperpolarizing current steps characteristic of half of X98 cells[44]. Fanning-out Martinotti cells display adapting type of firing pattern similar to GIN SST-INs[44]. Non-Martinotti cells, on the other hand, have the fast-spiking firing pattern of X94 SST-INs, with narrow spike width, low input resistance, stuttering-AP trains and lack the triphasic waveform that follows depolarizing current injections[44]. The morphological and electrophysiological classification described here seems to correlate with in vivo functional data as layer5 T-shaped and fanning-out shaped cells have been shown to have opposite spiking patterns during whisking[43].

In the cortex, SST-IN axonal branches show layer-specific organization, while SST-IN dendritic processes are mostly short and remain local[45]. For instance, layer 2/3 SST-INs have extensive axonal projections to layer 1, and to a lesser extent horizontally to layer 2/3[45]. Layer 5 SST-INs, on the other hand, have axonal arbors in layers 1 and 4, but also local

processes in layer 5[45]. On the contrary, layer 4 SST-INs tend to have local axonal arbors in layer 4, with only a few branches extending to layer1[45].

SST-INs have high connection probability to nearby neurons. Pyramidal cells are the primary cell type these connections are made: almost all SST-INs synapse on to a neighboring pyramidal cell and 30% of pyramidal cells connect to an SST-IN[46, 47]. The other major partners are parvalbumin-expressing interneurons (PV-INs) and vasoactive intestinal peptide-expressing interneurons (VIP-INs) [48, 49]. While SST IN-VIP IN connections are reciprocal, it is the SST-IN that synapses on to PV-IN[48, 49]. SST INs do not form chemical synapses between each other, but electrical coupling is common with half of neighboring SST-INs paired with gap junctions[50]. The connectivity between SST and other cell types is layer specific: SST-IN – PV-IN connections are predominant in layer IV, whereas in layer II/III pyramidal cell is the main SST-IN target[48, 51]. As a result, while SST-IN silencing inhibits pyramidal cells in layer IV, it has the opposite effect in layer II/III [48, 51].

Local cortical pyramidal cells are the major source of excitatory input to SST-INs[52]. These connections are weaker than those pyramidal cells make on to PV-INs[47]. However, given that a SST-IN receives input from many pyramidal cells in its surrounding and has facilitating synapses, it can be easily brought to firing by repetitive activity of pyramidal cells [53, 54].

VIP-INs provide inhibitory input to SST-INs [49]. Optogenetic stimulation of VIP-INs in cortical slices inhibits SST-INs [49]. A variety of input has been shown to recruit VIP-INs to inhibit SST-INs. For instance, stimulation of vibrissal motor cortex (vM1) glutamatergic projections to S1 leads to SST-IN inhibition[55]. Optogenetic silencing of VIP-INs blocks this

effect suggesting VIP mediates SST-IN inhibition[55]. Reinforcement signals have also been shown to modulate SST-INs activity via VIP-IN activation[56].

Several neuromodulators have been shown to increase SST-IN activity. Cortical SST-IN firing increases when cholinergic agonists are applied[57, 58]. This effect is specific: pyramidal and PV-INs do not respond to carbachol and muscarine [57]. Norepinephrine (NE), similarly, upregulates SST-IN spiking[59]. NE's effect is mediated directly through adrenergic receptors on the SST-cells as co-application of CNQX/APV does not block the response [59].

Somatostatin and Somatostatin Interneurons in Epilepsy

Epilepsy is characterized by the loss of balance between excitation and inhibition in the brain[60]. Several studies implicated SST and SST-INs in the development of epilepsy. For instance, selective loss of SST-INs in *Dlx* knock-out mouse results in reduced frequency and amplitude of inhibitory post-synaptic currents (IPSCs) in the hippocampal and cortical pyramidal cells[61]. $Dlx^{-/-}$ mice, at later stages of SST-IN loss, develop epileptic phenotype[61]. Similarly, in a mouse model of Dravet Syndrome — a genetic form of epilepsy that starts in childhood —loss of voltage-gated sodium channel $Na_V1.1$ reduces the excitability of cortical SST- and PV-INs[62]. The reduced excitability of SST-INs was shown to disrupt disynaptic inhibition between pyramidal cells [62]. While SST-IN loss and reduction in excitability have been associated with epilepsy, delivery of SST and SST analogues have been shown to have an ameliorative effect. A peptidase resistant analogue of SST-14, SMS201-995, reduced epileptic activity induced by kainic acid injection into the hippocampus[63]. Similarly, perfusion of SST suppressed bicuculline-induced epileptiform events in hippocampal slices [15]. Thus, somatostatinergic system can be a viable target for treatment of epilepsy.

Chapter 2: Development and In Vitro Characterization of Somatostatin Receptor 2-Expressing CNiFER Clones

A CNiFER is a genetically modified HEK293 cell that at its most basic state expresses a G_q-coupled GPCR targeted at the molecule of interest and a fluorescent Ca^{2+}-sensor[7]. Binding of the agonist to the GPCR increases intracellular Ca^{2+}-levels through the PLC/IP3 pathway and this increase is converted into a fluorescent signal by the Ca^{2+}-sensor [7]. However, If the GPCR is a Gi/o- or Gs-coupled GPCR, an adapter Gq protein is added to the CNiFER[8]. This Gq protein has the same sequence as a regular Gq protein except for five amino acid substitutions that let it couple to a Gi/o- or Gs-coupled GPCR [64]. This strategy has previously been applied to develop a D2 receptor-expressing CNiFER to detect dopamine [8]. Same as D2, all five somatostatin receptors (SSTR1-5) are coupled to Gi/o G proteins[65]. Therefore, in the present study, Gqi5 protein was introduced into HEKs in addition to Ca^{2+}-sensor and SSTR2.

Genetically-encoded calcium sensors have either single or two fluorophores [66]. A Förster resonance energy transfer (FRET)-based Ca^{2+} sensor is a type of two fluorophore sensor with donor and acceptor fluorophores linked by a Ca^{2+}-binding protein [66]. The sensor relies on FRET, which is a nonradiative form of energy transfer between an excited donor fluorophore and an acceptor fluorophore[66]. When FRET-based sensor binds to Ca^{2+}, sensor undergoes a conformational change and two fluorophore come closer increasing the FRET from donor to acceptor fluorophore[66]. As a result, acceptor fluorescence increases while donor fluorescence drops[66]. For instance, for TN-XXL and Twitch-2B (Tw2B), two FRET-based sensors used in

CNiFERs, Ca^{2+} increase leads to a decrease in CFP (donor) and an increase in YFP (acceptor) signal[7-9].

Materials and Methods

Transduction

hSSTR2 was cloned into pCDH vector (pCDH-CMV-MCS-EF1-Puro). Vector was amplified with bacterial transformation and extracted with Maxiprep kit. Subcloning was confirmed with sequencing. The vector was then sent to a core facility for lentiviral packaging.

Control CNiFER (Gqi5 Tw2B UR1D6 pre-CRiSPR or 128C3 HM4 CRiSPR-edited) expressing Tw2B and Gqi5 was grown in a T25 flask with HEK medium (DMEM, 10% Fetal Bovine Serum, 1x Pen/Strep). Once they reached 50% confluency, medium was replaced with 10^{11} GC/mL lentivirus (containing pCDH vector with SSTR2 gene). After a day, puromycin (2μg/mL in HEK medium) selection started. 2 days later part of selected cells was transferred to a new flask for single cell sorting, while the rest was frozen.

Single Cell Sorting, Expansion

Six 96-well plates were coated with poly-D-lysine (0.1mg/mL) and loaded with HEK medium with puromycin. The transduced cells were resuspended in 5mL of 5%(w/v) BSA in PBS and filtered through 40um strainer. Flow cytometer was programmed to select those cells that have high CFP and low FRET (low YFP on CFP excitation). Sorted cells were deposited in single wells of 96-well plate. Cells were grown for two weeks. When they became confluent in a well, they were transferred to a 24-well plate well. From a confluent 24-well, cells were transferred to a 96-well black bottom plate to be tested. The remaining cells were expanded and frozen.

Plate Reader Assay

Cells in HEK medium were plated in a 96-well black bottom plate the day before the plate reader run. On the day of experiment, drug plate was filled with agonists dissolved in artificial cerebrospinal fluid (ACSF) (125mM NaCl, 5mM KCl, 10mM D-Glucose, 10mM HEPES-Na, 3.1mM $CaCl_2$, 1.3mM $MgCl_2$). The plate reader was programmed to measure emitted fluorescence at 485nm and 527nm while exposed to light at 436nm every 4 sec for a total of 180s. Agonist delivery was made after collecting baseline fluorescence for half a min.

Plate Reader Data Analysis

Plate reader data was exported as the ratio of fluorescence signal at 527nm and 485nm channels (R_t). The data was then normalized to baseline by subtracting and dividing baseline fluorescence ratio (R_0) from each data point $(R_t-R_0)/R_0$. Baseline fluorescence ratio is defined as the ratio before adding SST and was the average of first five points in a run. Peak FRET ratio for each well was calculated by a formula written on excel that finds the point with the maximum value for each time trace and takes the average of this point along with the preceding and following points. Peak FRET ratio for a particular concentration in a plate run was computed by averaging replicate well results. Mean CNiFER FRET response to a particular concentration was calculated by averaging responses across multiple plate runs (N=3-11).

In Vitro Perfusion Assay

Cells were seeded on PDL-coated cover glasses (Dia:12mm, Thickness: #1) on the day before the experiment. On the day of the experiment, the cover glass was glued to a perfusion chamber with silicone. The imaging was made on an inverted microscope (Nikon TE300) fitted with a 430nm LED (Prizmatix) for excitation, a filter wheel (Sutter Lambda) with CFP (Chroma ET485/30m) and YFP (Chroma ET535/50m) emission filters, and a CMOS camera (Andor Zyla)

for acquisition. A dual bandpass dichroic (Chroma 51017bs) was on the light path to reflect the excitation light and let CFP and YFP through. Imaging setup components were controlled by Micromanager. The program was set to acquire 2 images with the camera every 3s while the wheel was alternating between CFP and YFP filters. The total experiment lasted for 20min where cycles of 30s SST (5nM) perfusion were followed with 3min artificial cerebrospinal fluid ACSF (125mM NaCl, 5mM KCl, 10mM D-Glucose, 10mM HEPES-Na, 3.1mM $CaCl_2$, 1.3mM $MgCl_2$) washes. The solutions were delivered into the chamber with a 6-channel gravity-fed perfusion set-up ending with 6-channel manifold. Individual lines were controlled with valves that were turned on and off with pCLAMP.

In Vitro Perfusion Assay Data Analysis

The stack of images obtained in a recording was collapsed in to a single z-stack average picture using ImageJ. This picture was then segmented with Graph Cut (ImageJ plug-in) to generate a region of interest (ROI) around the CNiFER cluster. ROI was overlaid over the CNiFER ratio image stack (YFP/CFP) and Time series analyzer (ImageJ plug-in) was used to calculate the CNiFER fluorescence ratio across time. CNiFER fluorescence ratio was then normalized by the formula(R_t-R_0/R_0), where R_t is fluorescence ratio at each time point and R_0 is the baseline fluorescence ratio. Peaks on the normalized fluorescence trace corresponding to each cycle of SST delivery was calculated using the maximum function on excel. The 6 peaks for each recording were averaged across coverslips. One-way ANOVA with post-hoc Tukey test was run to study the effect of SST delivery order on the CNiFER FRET peak response.

Results

To generate SSTR2-expressing clone, a previously developed control CNiFER (Gqi5 Tw2B UR1D6 pre-CRiSPR) was transduced with lentivirus expressing SSTR2. The transduction resulted in a heterogeneous population of cells varying in the extent they express the receptor. To obtain clones, transduced cells were single-cell sorted on a flow cytometer. Flow cytometer also allowed for selecting cells that have high fluorescence but low baseline FRET(Fig.2.1).

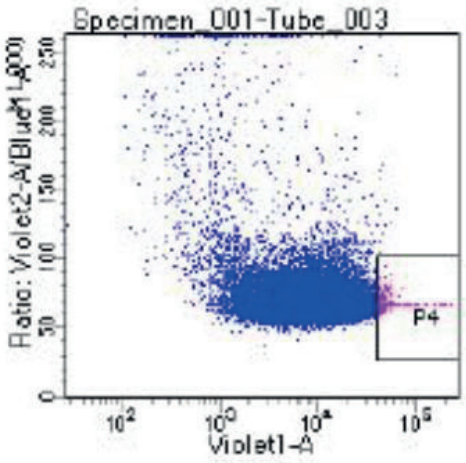

Fig.2.1 CNiFER clones obtained by viral transduction of control CNiFER (Gqi5 Tw2B UR1D6 pre-CRiSPR) with SSTR2 receptor were single cell-sorted on a flow cytometer. Cells that have high CFP (Violet1: CFP emission signal on CFP excitation) and low FRET (Violet2: YFP emission signal on CFP excitation) were selected (P4 gate). Blue1 (YFP emission signal on YFP excitation) was used to normalize the FRET signal. Flow cytometer data was obtained by Erin Aisenberg.

Over 100 clones survived single-cell sorting. These were then tested on a plate reader that allows for fluorescence measurements on two channels (CFP emission at 485nm and YFP emission at 536nm) while exciting with a single wavelength (CFP excitation at 436nm). Plate reader screening of clones for maximal FRET peak change in response to SST, led to selection of Gqi Tw2B UR1D6 SSTR2.6 clone (referred to as SSTR2.6 pre-CRiSPR) for further characterization (data not shown).

SSTR2.6 CNiFER (pre-CRiSPR) was then tested against varying concentrations of SST to compare its sensitivity and FRET response size with a previously developed TN-XXL- expressing clone (SSTR2.46). SSTR2.6 CNiFER (pre-CRiSPR) showed a 6-fold larger FRET peak at saturation compared to SSTR2.46 CNiFER (SSTR2.6 CNiFER FRET peak = ~2.4, SSTR2.46 CNiFER FRET peak =~0.4 at 100nM SST) (Fig2.2 A, B). The improvement on the signal did not cost sensitivity. Half maximal effective concentration (EC50), which was calculated by fitting a variable slope curve on log (SST concentration) vs FRET peak data set and finding the SST concentration at which CNiFER responds 50% of its maximal FRET level, was comparable for two CNiFERs (EC50(SSTR2.6 pre-CRiSPR) = 35nM vs. EC50(SSTR2.46) =15nM) (Fig.2.2 A, B). Control CNiFER (Gqi5 Tw2B UR1D6 pre-CRiSPR), which was not transduced with SSTR2, also had a response to SST at high concentrations possibly associated with the endogenous SSTRs (EC50 (Control CNiFER Gqi5 Tw2B UR1D6 pre-CRiSPR) = 350nm, Fig2.2 A)[70].

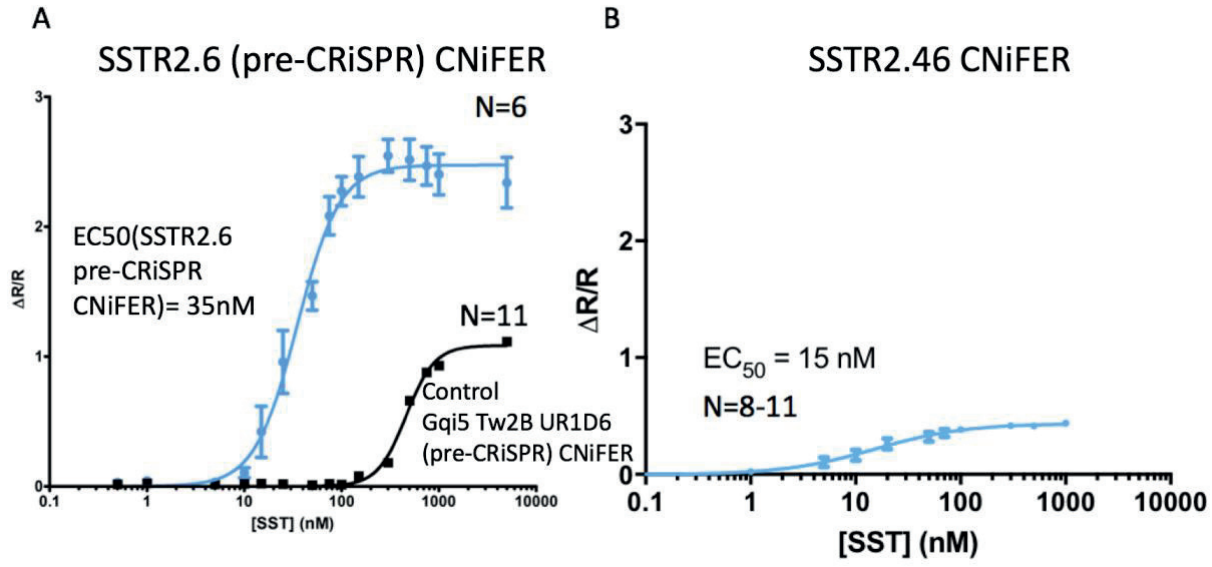

Fig.2.2 Mean FRET peak responses to increasing concentrations of SST are plotted for three CNiFER clones(±SEM). SSTR2.6 and control CNiFERs (A) have Tw2B as a Ca^{2+}-sensor, whereas SSTR2.46 (B) expresses TN-XXL. Half-maximal effective concentration (EC50) is the

concentration at which CNiFER shows 50% of its maximum FRET response. EC50 was calculated by fitting a variable slope curve on log (SST concentration) vs FRET peak data. Total number of plate reader runs are indicated on the side of the graphs. Plate reader data was obtained by Erin Aisenberg.

Although frequently used as a heterologous expression system, HEK293 cells have endogenous GPCRs [70]. To test whether SSTR2.6 (pre-CRiSPR) CNiFER have non-specific responses to GPCR agonists, SSTR2.6 (pre-CRiSPR) CNiFER was probed norepinephrine(NE), glutamate, acetylcholine (ACh), vasoactive intestinal propeptide (VIP), substance P (SP), serotonin (5-HT), corticotropin releasing factor (CRF), cholecystokinin (CCK), dynorphin A, GABA, neuropeptide Y(NPY), orexin A, dopamine, neurokinin B. SSTR2.6 CNiFER (pre-CRiSPR) was found to have a non-specific response to ACh, ATP, CRF, CCK and VIP at the two concentrations tested 100nM, 1uM (Fig.2.3).

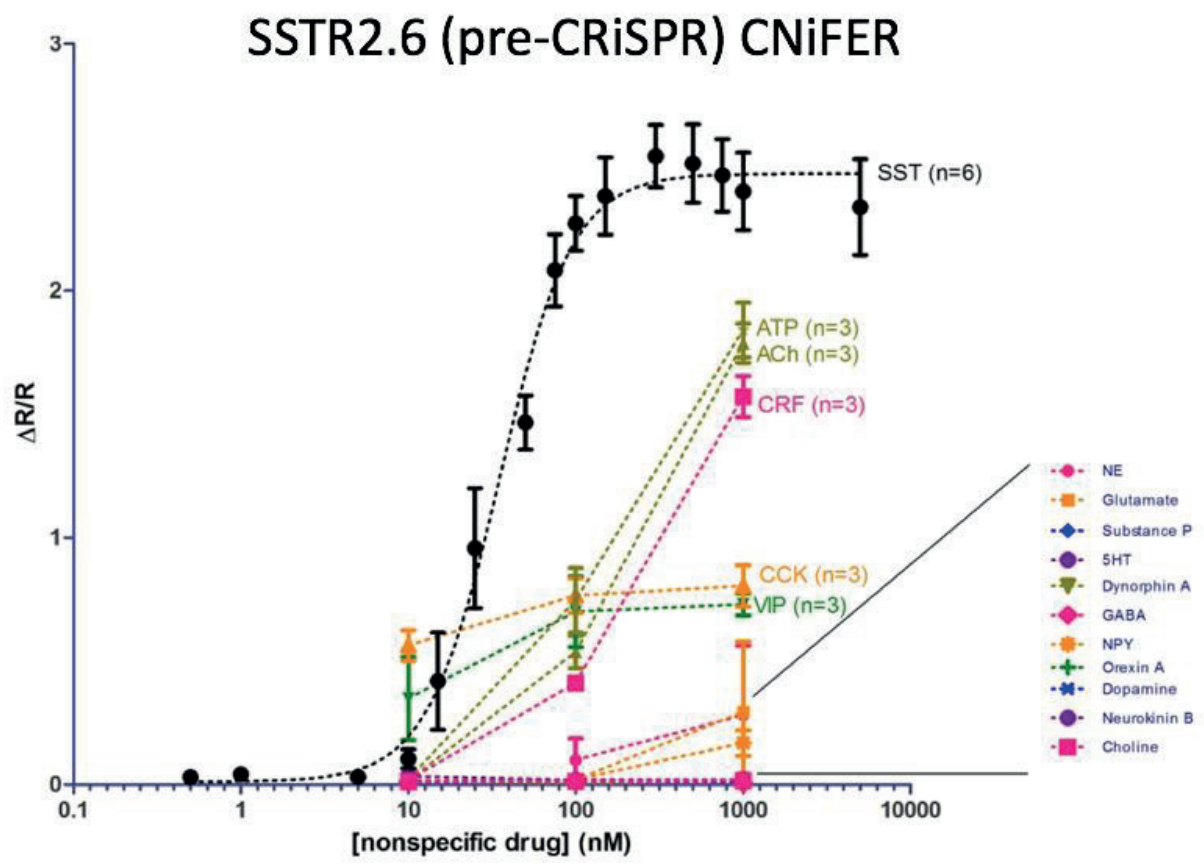

Fig.2.3 Mean SSTR2.6 (pre-CRiSPR) CNiFER FRET peak response to the given agonist concentration is plotted(±SEM). Total number of plate reader runs are indicated on the side of the graphs. Plate reader data was obtained by Erin Aisenberg.

SSTR2.6 (pre-CRiSPR) CNiFER was planned to be used in two experiments in later stages of the project. First of these involved photostimulation of ChR2-expressing SST-INs and detection of SST with the SSTR2 CNiFER. SSTR2.6 (pre-CRiSPR) CNiFER's non-specific responses to ACh, ATP, CRF, CCK, VIP posed a problem for this experiment as SST-INs have previously been shown to express ACh, CRF, CCK, VIP, and thus photostimulation of SST-INs may lead to release of these peptides and ATP along with SST [37, 71-73]. However, several controls existed for this experiment. For instance, if control CNiFER did not respond to optogenetic stimulation of SST-IN while SSTR2.6 did, this would suggest a specific SST response. Moreover, performing optogenetic stimulation in SST-KO (-/-) mouse or in the presence of SSTR antagonists could be used to confirm the specificity. Thus, SSTR2.6 (pre-CRiSPR) CNiFER was used in the optogenetic stimulation experiment (Chapter 4).

However, the same controls were not applicable to the second experiment, which involved cholinergic stimulation of SST-INs. As SSTR2.6 (pre-CRiSPR) CNiFER responds to both ACh and SST, one would not be able to tell which one SSTR2.6 (pre-CRiSPR) CNiFER is detecting on cholinergic stimulation. To address this issue, endogenous muscarinic receptor M4 (HM4) was targeted[70]. To remove the HM4 receptor gene, control CNiFER (Gqi Tw2B UR1D6, same clone SSTR2.6 (pre-CRiSPR) CNiFER originated) was transfected with Cas9 and HM4 gRNA. Transfected clones were selected with puromycin and single-cell sorted. Survived clones were screened on the plate reader for ACh response. Gqi5 Tw2B UR1D6 CM4 128C3 (referred to as Control 128C3 (HM4 CRiSPR-edited)) clone was selected based on its low response to 1nM ACh

without a loss of basal fluorescence (Fig. 2.4 A, red-circled). After CRiSPR-editing, plate reader test showed that control 128C3 (HM4 CRiSPR-edited) CNiFER did not respond appreciably to any of the agonists indicating that CRiSPR-editing did not have any off-target effect to increase non-specific CNiFER responses (Fig.2.4 C).

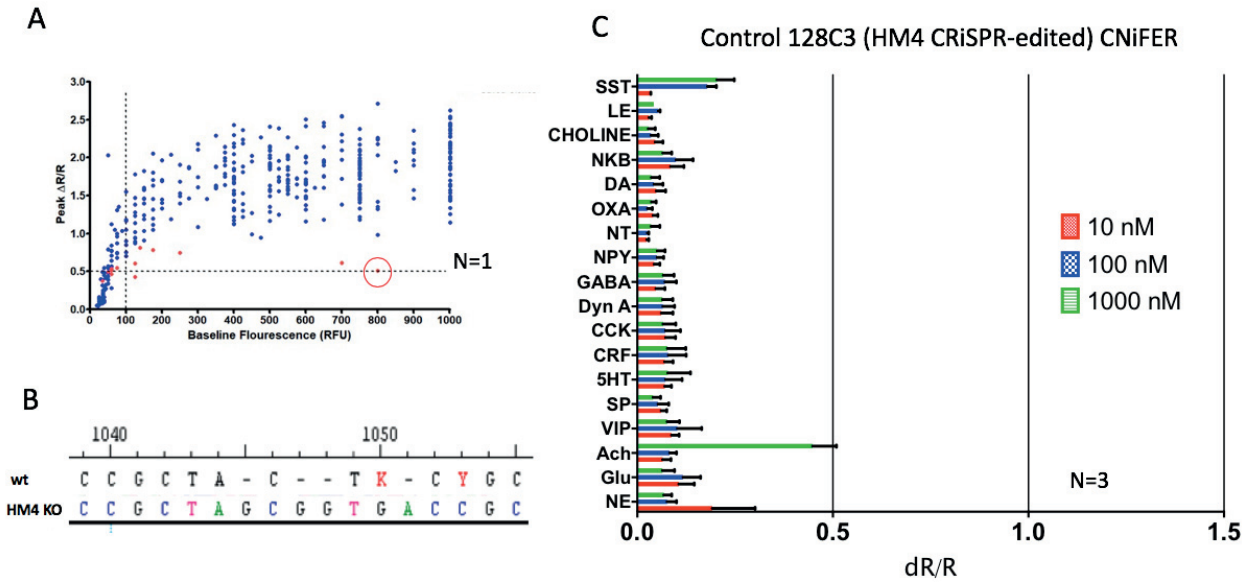

Fig. 2.4 (A) HM4 CRiSPR-edited control CNiFER clones FRET peak responses to 1nM ACh are plotted. CRiSPR editing was made on control (Gqi5 Tw2B UR1D6 pre-CRiSPR) CNiFER and resulted in a heterogenous population of HM4-CRiSPR-edited control CNiFER clones. Each dot represents a clone. Selected clone, control 128C3 CNiFER (HM4 CRiSPR-edited), is red circled (bottom right). (B) CRiSPR-editing of HM4 in control 128C3 CNiFER (HM4 CRiSPR-edited) was confirmed with sequencing. (C) Control 128C3 (HM4 CRiSPR-edited) CNiFER mean FRET peak response to a given concentration of agonist is plotted (±SEM). Total number of plate runs is indicated on the side. CRiSPR editing and plate reader screening was carried out by Tyler Kern.

The control 128C3 CNiFER (HM4 CRiSPR-edited) was then transduced with SSTR2, selected with antibiotic, single-cell sorted. Gqi5 Tw2b UR1D6 CM4 128C3 SSTR2 5F3 clone (referred to as SSTR2 5F3 (HM4 CRiSPR-edited) CNiFER) was selected after clonal screening on a plate a reader. SSTR2 5F3 (HM4 CRiSPR-edited) CNiFER was found to have similar sensitivity to SST as the previous two clones (EC50(SSTR2 5F3) =4nM, EC50(SSTR2.46) =15nM, EC50(SSTR2.6)

=35nM). However, SSTR2 5F3 (HM4 CRiSPR-edited) CNiFER FRET response at saturating level SST was 5-fold higher than TN-XXL-expressing SSTR2.46. (SSTR2 5F3 CNiFER FRET peak=~2.0, SSTR2.46 CNiFER FRET peak=~0.4 at 100nM) (Fig.2.5 A). Control 128C3 (HM4 CRiSPR-edited) CNiFER did not respond to SST (Fig.2.5 A).

To make sure that introduction of the SSTR2 did not change the response pattern of control 128C3(HM4 CRiSPR-edited) CNiFER, the SSTR2 5F3(HM4 CRiSPR-edited) CNiFER was tested with 14 transmitters (and choline). The FRET responses were found to be similar to the original control 128C3 (HM4 CRiSPR-edited) clone (Fig.2.5 B).

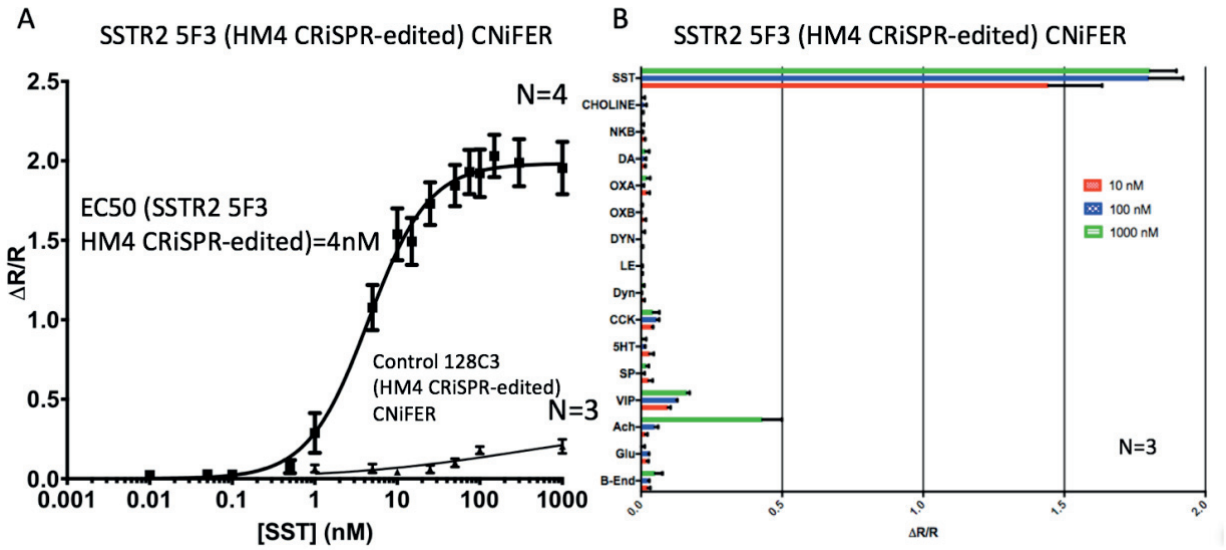

Fig.2.5 (A) Mean SSTR2 5F3 (HM4 CRiSPR-edited) CNiFER and control 128C3 (HM4 CRiSPR-edited) CNiFER FRET peak responses to the given concentration of SST is plotted(±SEM). (B) Mean SSTR2 5F3 (HM4 CRiSPR-edited) CNiFER FRET peak response to the given concentration of agonist is plotted (±SEM). Total number of plate runs is denoted. Plate reader data was obtained by Tyler Kern.

Signaling through SSTR2 can be reduced through homologous desensitization [74]. To test for desensitization of the SSTR2 receptor, the SSTR2 5F3 (HM4 CRiSPR-edited) CNiFER was exposed to SST (5nM) multiple times in an in vitro assay (Fig.2.6 A,B). At the concentration

tested (5nM), there was no effect of the order of stimulus on the SSTR2 5F3 (HM4 CRiSPR-edited) CNiFER FRET peak response (one-way repeated measure ANOVA, p>0.05) (Fig.2.6C). A previous study suggested that the extent of SSTR2 phosphorylation —the process that leads SSTR2 desensitization— depends on the concentration of SST[74]. The same study showed that SSTR2 phosphorylation was noticeably increased at 3nM SST and was maximal at 100nM[74]. Considering CSF levels of SST can go up to 30nM in certain mammals, the desensitization of SSTR2 5F3 (HM4 CRiSPR-edited) CNiFER should be tested with higher levels of SST in subsequent experiments [75].

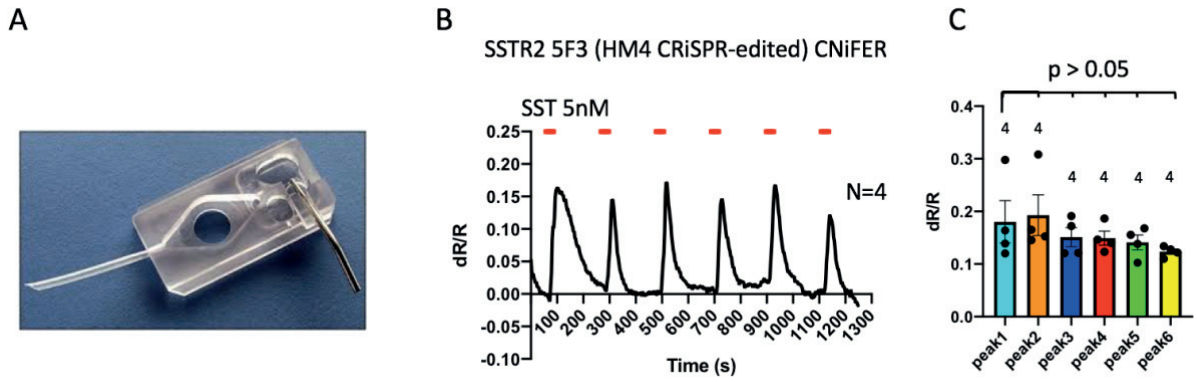

Fig.2.6 (A) SSTR2 5F3 (HM4 CRiSPR-edited) CNiFER desensitization test was performed in a perfusion chamber. CNiFER was exposed to alternating cycles of SST (5nM) (30s) and ACSF (3min) for six times. (B) SSTR2 5F3 CNiFER (HM4 CRiSPR-edited) FRET trace in a recording, where the cells were exposed to six cycles of 5nM SST, is plotted. Red bars indicate SST (5nM) delivery. (C) Peak values in a FRET ratio trace were determined for each recording and averaged across coverslips to generate a bar graph (±SEM, N=4 coverslips). There was no effect of the order of delivery on the CNiFER FRET peak indicating CNiFER does not desensitize at this level of SST(5nM) (ANOVA with post-hoc Tukey test, p>0.05).

Discussion

The SSTR2 CNiFER clones that express Tw2B (SSTR2.6 and SSTR2 5F3) had 5-6-fold higher peak FRET responses at saturating level SST (100nM) compared to the TN-XXL-expressing

SSTR2.46 consistent with Tw2B being a brighter sensor compared to TN-XXL [67, 68]. The improvement on FRET peak responses with Tw2B-expressing CNiFERs make them better suited for in vivo imaging, where there is a significant drop in signal level due to light scattering [76].

HEK cells are frequently used for heterologous expression of membrane proteins because they have a high transfection/transduction efficiency, faithfully translate and process proteins and have a high mitotic rate[77]. However, HEK cells also have endogenous receptors that makes them responsive to GPCR agonists[70]. This was also evident in CNiFER plate reader assays. CNiFER clones showed VIP responses consistent with a previous report of an endogenous VPAC1 receptor in HEK cells[78]. Screening for non-specific agonists also revealed CNiFER responses to ACh, ATP, CRF and CCK. Of these non-specific responses only ACh has been addressed in the present study as it was required to study cholinergic induction of SST release.

In the present study, SSTR2 5F3 CNiFER response did not attenuate on multiple exposures to SST(Fig.2.6C) However, a previous report has shown that SSTR2 desensitization is a concentration-dependent process suggesting SSTR2 CNiFER may desensitize at concentrations higher than tested in the present study (>5nM). [74]. To determine the full extent of CNiFER desensitization perfusion assay can be repeated with concentrations higher than 5nM. In case of a desensitization, perfusion assay may also aid in determining recovery time for SSTR2 receptor.

Chapter 3: In Vivo Characterization of Somatostatin Receptor 2-expressing CNiFER Clones

In vitro experiments in Chapter 2 have shown that SSTR2.6 (pre-CRiSPR) CNiFER has nanomolar sensitivity to SST. However, in vitro experiments did not establish whether CNiFER would function in vivo as they were conducted in ACSF that lacked molecules found in the extracellular medium of the brain. Previous studies have shown that there is a basal level of 30nM SST in the brain[75]. Given agonist-mediated desensitization of SSTR2, SSTR2 CNiFER may be inactivated with this basal level of SST[74]. To test whether SSTR2.6 CNiFER is functional in vivo, SSTR2.6 CNiFER was implanted into the mouse brain and probed with external injection of SST.

Materials and Methods

CNiFER implantation

Adult C57BL/6 mouse (postnatal 3-6months) was anesthetized with 4% isoflurane. Mouse was mounted on a stereotaxic frame, where it rested on a heating pad. Isoflurane was lowered and maintained at 1.5% during the surgery. Eyes were covered with eye ointment and top of the skull was shaved. Exposed skin was sterilized with betadine and isopropanol (70%). A cut following the midline between the ears was made. Skin lining the incision was moved aside with clamps to expose the top of the skull. The surface of the skull was cleaned with ACSF-soaked cotton swab. A cranial window with 3mm diameter centered at C2 barrel column (AP: -1.6, ML: 3.3mm) was drilled (#5 drill bit). Once the cap started loosening, a drop of ACSF was

added and cap was removed with forceps (#5). ACSF-soaked surgical sponge was left on the exposed brain while harvesting CNiFERs for injection.

CNiFERs grown to 90% confluency in a T75 flask were incubated with trypsin (0.05%) and dislodged by pressure ejection of ACSF from a pipettor. Cells were pelleted at 1,200g and then pipetted onto a parafilm strip. Cells were then sucked into a glass pipette (40μm tip) using a nanoliter injector. Pipette tip was brought over the window to an area clear from blood vessels and lowered 200μm below the dura. 10 x 4.6nL injections were made with nanoliter injector. 5min after the injection pipette was raised and injection was repeated in two more sites (Fig.3.1B). The window was then washed with ACSF and covered with silicone.

A cross head-bar was cemented to the skull anterior to bregma. A crown of cement was made surrounding the window to work with water-immersion objectives. Mouse was then removed from the stereotaxic frame, injected with 1mL 0.9% saline solution, and placed on a warm pad.

In Vivo Somatostatin Injection and Imaging

2 hours after the surgery, the mouse was mounted on an imaging frame screwing the head bar. A glass pipette filled with SST and Alexa 594 dye (100nM) was inserted into a pipette holder standing on the side of the imaging frame(Fig3.1 A). The probe holder was tilted at a 30° and connected to a micromanipulator that allowed movement in the xyz and diagonal directions. A software (LinLab) displayed the xyz-coordinates of the pipette. To bring the tip of the glass pipette near the CNiFER, first the depth of the CNiFER was determined by an optical z-scan. Based on the depth, required movement was calculated. Once the coordinates were dialled, two photon imaging was turned on and final adjustments were made (Fig3.1C). CNiFERs

were imaged at 810nm with a 4-10μs/pixel scan rate. Laser power measured at the exit of objective varied between 60-160mW. CNiFER signal was filtered at 460-500nm and 520-560nm, and collected by photomultiplier tubes. Images were acquired at a rate of 1-2fps. SST delivery to the brain was made by pressure pulse injections using a valve controller (Picospritzer). Pressure and duration of pulses varied between injections (10-30psi, 5-50ms). One injection cycle involved 40 pressure pulse injections every 1.5s and was triggered by pClamp program. In a typical recording, multiple injection cycles were delivered. The interval between injection cycles varied between 5-10min. Mouse was anesthetized during imaging (1.5% isoflurane).

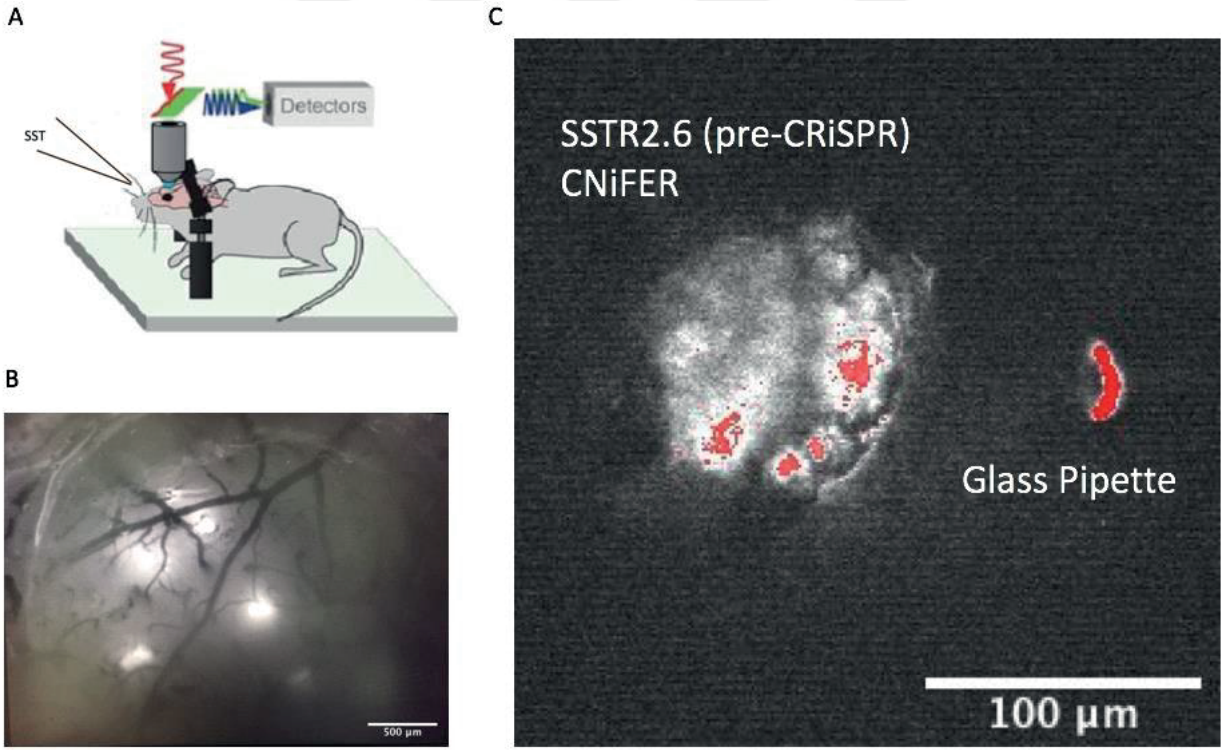

Fig.3.1 (A) Imaging frame that holds the mouse steady while imaging. Mouse was anesthetized (1.5% isoflurane) during recordings. (B) Fluorescence microscopy image of the cranial window is displayed. Cranial window is 3mm wide. 5 CNiFER clumps are visible. (C) Two-photon image at 200μM depth from the brain surface is displayed. For in vivo SST injections pipette was brought 100μm away from the CNiFER clump center.

In Vivo Somatostatin Injection Imaging Data Analysis

Normalized CNiFER FRET trace was extracted and calculated from two stack of images (CFP and YFP) as described previously (see Chapter 2, Materials and methods: In Vitro Perfursion Data Analysis). CNiFER FRET peak in response to an injection was calculated in several steps. First, the maximum FRET ratio value in the five minutes following an injection was determined. This maximum value was then averaged with the preceding and following two points. FRET ratio baseline (average FRET ratio value of 10 points preceding the end of an injection cycle) was then subtracted from the maximum to give the CNiFER FRET peak represented in the graphs. Mean CNiFER FRET peak to each cycle of injection was first calculated for each animal and then averaged across animals. Paired t-test was performed to compare the SSTR2.6 (pre-CRiSPR) CNiFER FRET peak responses to the first and second cycle of injections. Unpaired t-test was conducted to compare SSTR2.6 (pre-CRiSPR) CNiFER and control (Gqi5 Tw2B UR1D6 pre-CRiSPR) CNiFER FRET peak responses to 1μM SST. One-way ANOVA was performed to test the effect of somatostatin concentration on the SSTR2.6 CNiFER (pre-CRiSPR) FRET peak response and was followed by Tukey post-hoc test.

Results

To test whether SSTR2.6 is functional in vivo, SST was injected onto the SSTR2.6 CNiFER (pre-CRiSPR) after surgical implantation. injection (200nM SST) resulted in a FRET change (mean SSTR2.6 CNiFER FRET peak = 0.086±0.026, N=3 animals) suggesting basal SST did not inactivate the CNiFER (Fig.3.2 A, B). However, a second injection delivered 5 min after first resulted in a 34% drop in FRET peak response (mean SSTR2.6 CNiFER FRET peak =0.057±0.025, N=3 animals)

(Fig.3.2 B). These results suggest SSTR2.6 CNiFER is functional in vivo but desensitizes with closely followed SST injections.

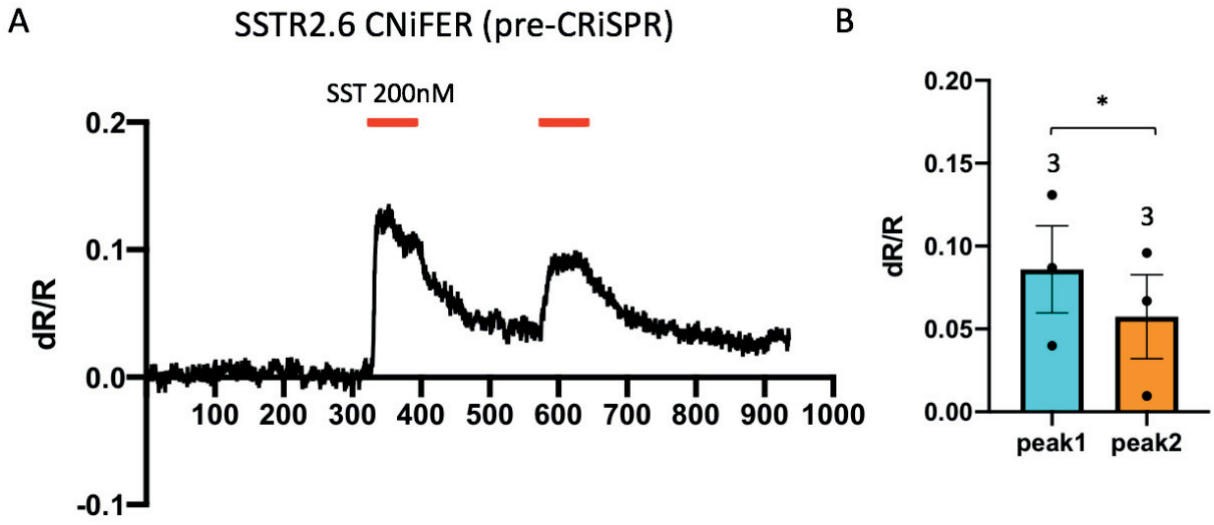

Fig.3.2 (A) SSTR2.6 CNiFER (pre-CRiSPR) FRET trace in a single in vivo recording, where two cycles of SST (200nM) injection were made, is plotted. Each red bar indicates one cycle of SST injection (one injection cycle = one 10-30psi pressure pulse injection every 1.5s over 1min) (B) Mean SSTR2.6 CNiFER FRET peaks in response to the first and second cycle of SST (200nM) injection are plotted (±SEM, N=3mice). Although SSTR2.6 CNiFER responded to the second injection, there was a significant drop in FRET peak response (paired t-test, $p<0.05$).

To test whether SSTR2.6 CNiFER FRET peak varies with increasing SST concentrations in the medium, known concentrations of SST were applied onto the SSTR2.6 CNiFER (pre-CRiSPR). SSTR2.6 CNiFER (pre-CRiSPR) FRET peak response increased with increasing concentration of SST with a maximum FRET ratio change at 5μM SST (mean SSTR2.6 FRET peak (5μM SST) =0.182±0.051) (Fig.3.3). Moreover, a significant effect of SST concentration on the SSTR2.6 (pre-CRiSPR) CNiFER FRET peak was detected (one-way ANOVA, $p<0.025$) (Fig. 3.3). Thus, SSTR2.6 CNiFER is suited for informing about relative concentration differences in the medium.

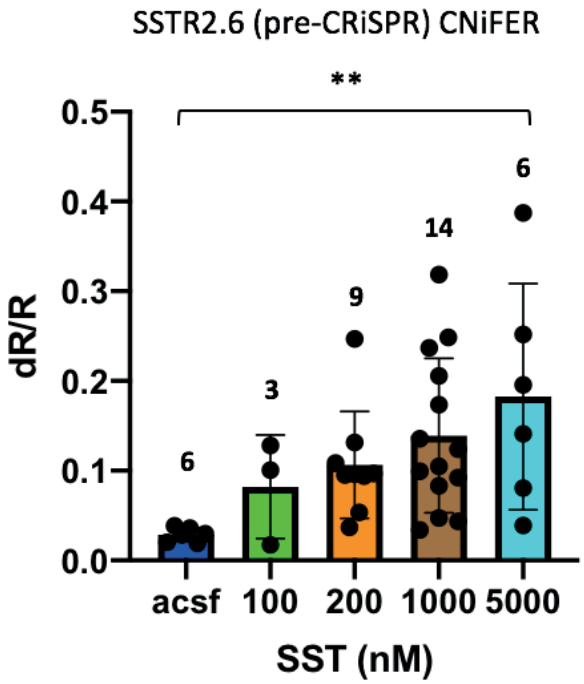

Fig.3.3 Mean SSTR2.6 CNiFER (pre-CRiSPR) FRET peak response to a cycle of in vivo SST injection at the given concentration is plotted (±SEM). Total number of animals injections were performed is indicated on top of the bars. There was a significant effect of SST concentration on the SSTR2.6 CNiFER FRET peak response (ANOVA followed by Tukey post-hoc test, **p<0.025).

Variation of SSTR2.6 CNiFER (pre-CRiSPR) FRET peak response with increasing concentration of SST indicated that the response is not due to the Alexa594 dye (Fig.3.3). To further corroborate the specificity of the response, SST was injected onto the control CNiFER (Gqi5 Tw2B UR1D6, pre CRiSPR) (Fig.3.4B). At a concentration SSTR2.6 CNiFER was previously demonstrated to respond (Fig.3.4A), control CNiFER (Gqi5 Tw2B UR1D6) did not show a FRET change (Mean SSTR2.6 FRET peak=0.153±0.032SEM, N=5 mice; mean control (Gqi5 Tw2B UR1D6) CNiFER FRET peak =0.035±0.007, N=3 mice; unpaired t-test, p<0.05) (Fig.3.4C). Thus, control CNiFER (Gqi5 Tw2B UR1D6) can be employed to show specificity of SSTR2.6 CNiFER

response to SST.

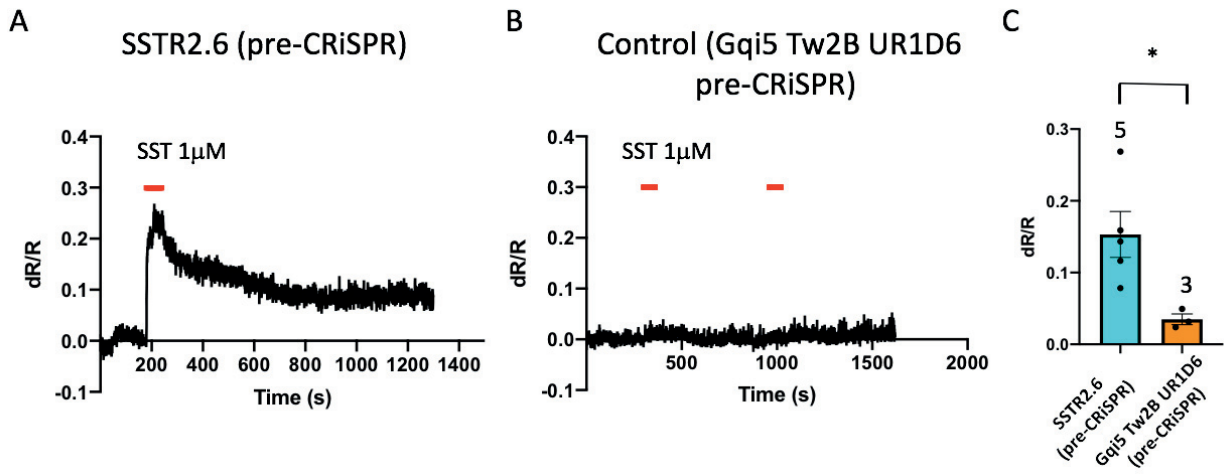

Fig.3.4 (A) SSTR2.6 (pre-CRiSPR) CNiFER FRET trace in an in vivo recording, where one cycle of SST(1μM) injection was made, is shown. (B) Control (Gqi5 Tw2B UR1D6 pre-CRiSPR) CNiFER FRET trace in an in vivo recording where two cycles of SST(1μM) injection were made, is shown. Red bar indicates one cycle of SST injection (one injection cycle = 10-30psi pressure pulse injections every 1.5s over 1min). (C) Mean SSTR2.6 (pre-CRiSPR) CNiFER and control (Gqi5 Tw2B UR1D6 pre-CRiSPR) CNiFER FRET peak responses to a cycle of SST(1μM) injection are shown (±SEM). Total number of animals injections were performed is indicated on top of the bars. (unpaired t-test, *p<0.05)

Discussion

In vivo SST concentration in the extracellular medium is about 30nM [75, 79]. SSTR2.6 (pre-CRiSPR) CNiFER's FRET response to SST injection suggests that CNiFER's exposure to the basal level of SST does not inactivate the CNiFER (Fig.3.2 A). However, SSTR2.6 CNiFER FRET peak responses to in vivo SST injections are significantly smaller than its responses to the same concentrations in vitro (Fig.2.2A, Fig.3.3). Significant differences exist between plate reader and in vivo conditions which may explain the difference between two results. In plate reader, a large volume of SST (50μL) is delivered into a well in one burst of injection (~sec) through a large tip pipette. However, the delivery of SST in in vivo condition is in small volume (<200nL), occurs

through a small-diameter tip (20μm) and takes a longer time (1min). Moreover, the injection in in vivo condition is not made into a confined space, which leads to fast dissipation of SST. Solution delivery to the CNiFER in vivo can be improved by enlarging the pipette tip diameter, increasing the pressure or frequency of injections, or getting closer to the CNiFER.

The drop in SSTR2.6 CNiFER FRET peak response on the second cycle of SST (200nM) injection and the difference between SSTR2.6 CNiFER FRET peak responses to SST delivery in vitro and in vivo conditions suggest that SSTR2.6 CNiFER is not suited for measuring absolute SST concentration in vivo (Fig.2.2A, Fig.3.2, Fig.3.3). However, the steady increase in SSTR2.6 (CNiFER FRET peak in response to increasing concentrations of SST suggests that SSTR2.6 is suited for relative comparisons (Fig.3.3).

Multiple SST injection experiment has shown that SSTR2.6 (pre-CRiSPR) CNiFER FRET peak response drops significantly on the second injection of SST (Fig.3.2 A). Previous studies have demonstrated somatostatin receptor phosphorylation and internalization are reversible processes [80, 81]. To test whether SSTR2 CNiFER response recovers over time, multiple injections experiment was repeated with a longer interval. SSTR2.6 CNiFER FRET response to the second injection did not significantly decrease when the two injections were separated by 10min (Fig.3.5). This result suggests SSTR2.6 (pre-CRiSPR) CNiFER is suited for making SST level comparisons in vivo as long as sufficient time (>10min) is given between experimental manipulations that will drive SST release.

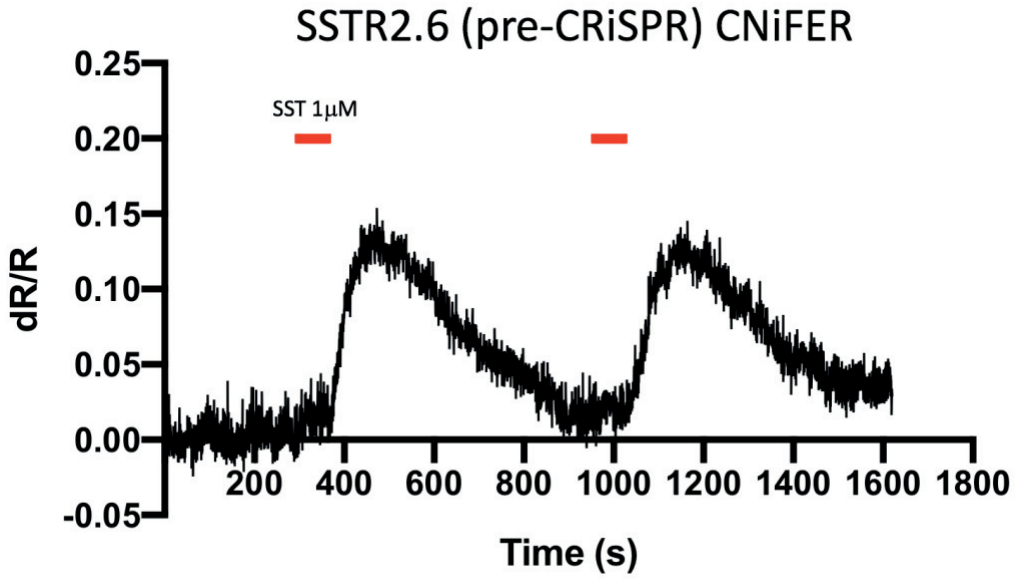

Fig.3.5 SSTR2.6 (pre-CRiSPR) CNiFER FRET trace in an in vivo recording, where two cycles of SST (1μM) injection (one injection cycle = one 10-30psi pressure pulse injection every 1.5s over 1min) were made, is shown. Although the concentration of SST(1μM) is higher than Fig.3.2.2(A), with a 10-min interval, there is not a significant drop in SSTR2.6 (pre-CRiSPR) CNiFER FRET response to the second injection.

In vivo SST injection tests performed in this study were acute experiments that followed SSTR2 CNiFER surgery. Thus, how SSTR2 CNiFER sensitivity changes across days remains to be tested. Chronic imaging with SSTR2 CNIFER can inform about SST level changes that may not be evident in short duration recordings. Several studies suggest brain SST level may vary during sleep-wake cycles. For instance, SST-IN firing increases before slow wave activity during non-rapid eye movement (NREM) sleep[82]. SST CSF level shows a daily variation, with a higher level during dark period for diurnal animals[83, 84]. An SSTR2 CNiFER that does not desensitize over time would answer how SST level changes between sleep-wake cycles.

Chapter 4: In Vivo Detection of SST Released by Optogenetic Stimulation of Somatostatin-Expressing Interneurons

SST is used as a molecular marker to classify a group of neurons[34]. However, SST can be released into the medium [24, 26]. Experiments with cultured rat hypothalamic cells have shown that depolarization with high concentration of K^+ leads to SST release [24]. Lowering extracellular Ca^{2+} blocks K^+-induced release suggesting the effect is Ca^{2+}-dependent[24]. Hypothalamic cells have also been shown to release SST tonically [24]. Tetrodotoxin blocked this release suggesting spontaneous cell firing underlies this tonic release [24]. Amino acid agonists can modulate SST release. Studies with cultured rat cortical neurons showed that excitatory amino acid agonists (glutamate, NMDA, quisqualate, and kainate) stimulate SST release in a dose dependent manner[26]. In contrast, GABA was shown to decrease tonic release of SST from cultured hypothalamic cells[24].

To selectively stimulate the SST-INs, in the present study, Cre-Lox strategy was combined with optogenetics [85, 86]. Sst-Cre mouse line, which had an IRES-Cre insert next to somatostatin gene, was crossed with Ai32 mouse line that expressed light-activated cation channel channelrhodopsin (ChR2) in a Cre-dependent manner[86, 87].

Materials and Methods

Animals

$Sst^{tm2.1(cre)Zjh}$/J (Jax Stock No:013044) and B6.Cg-*Gt(ROSA)26Sor*$^{tm32(CAG-COP4*(H134R)/EYFP)}$ (Jax Stock No: 024109) were crossed to obtain the mice used in the study. Genotype was either Sst-Cre (0/Tg) floxed-ChR2-eYFP(+/+) or Sst-Cre (Tg/Tg) floxed ChR2-eYFP(+/+).

Immunostaining

An adult mouse (Sst-Cre 0/Tg. floxed-ChR2-eYFP Tg/Tg) was anesthetized with 100mg/kg ketamine, 10mg/kg xylazine. Mouse was transcardially perfused with 10mL ice-cold PBS (137mM NaCl, 2.7mM KCl, 10mM Na_2HPO_4, KH_2OPO_4 1.8mM) and 25mL 4%PFA using a peristaltic pump set to 5mL/min. Extracted brain was post-fixed with 4% PFA overnight at 4°C. 50μm thick coronal sections of S1 barrel cortex were taken on a vibratome.

Slices were blocked with 2% bovine serum albumin (BSA) in PBS-T (0.3% Triton-X in PBS) for 30min. Slices were incubated in primary antibody (rabbit anti-eYFP, 1:2,000, Invitrogen A6455) overnight at 4°C. The slices were then washed with PBS-T and incubated in secondary antibody (Alexa 488-conjugated donkey anti-rabbit, 1:500, Jackson 711-545-452) for 1hr. Slices were then washed with PBS and mounted on slides. Images of barrel cortex were taken on a fluorescence microscope while 5x objective and FITC-filter cube were set.

Surgery

Surgery was the same as previously described (see Chapter 3, Materials and methods). The only difference was the addition of a cover glass (circular, 3mm diameter, #0) over the craniotomy to allow for chronic imaging. Buprenorphine (0.1mg/kg) injections (2 times per day) were made until the animals were sacked three days after the surgery.

Photostimulation of SST-INs and SSTR2.6 (pre-CRiSPR) CNiFER Imaging

With FITC filter set and mercury lamp on, the tip fiber optic cannula (either 200μm or 400μm diameter) was brought over the CNiFER using a micromanipulator. The light stimulation was made with an LED driver controlled by pCLAMP software. In one cycle of photostimulation twenty 4ms pulses were delivered every 2s for 30s. On a single recording three to four cycles of

photostimulation were made, where each photostimulation cycle was separated by 10min from the previous. The interval between photostimulation cycles was shorter for control (Gqi5 TW2B UR1D6, pre-CRiSPR) CNiFER. To show the variation of the FRET peak with increasing frequency/LED power, in several figures (Fig.4.6A, Fig.4.7A, Fig.4.9A, Fig.4.10A), FRET traces originating from separate recordings were joined into a single FRET trace. The light intensity (measured at the tip of the fiber optic cannula) was set at 9.5mW, when the effect of blue light stimulation frequency on the SSTR2.6 (pre-CRiSPR) CNiFER FRET peak response was studied. The frequency of blue light pulses was set at 30Hz, when the effect of LED power on the SSTR2.6 (pre-CRiSPR) CNiFER FRET peak response was studied.

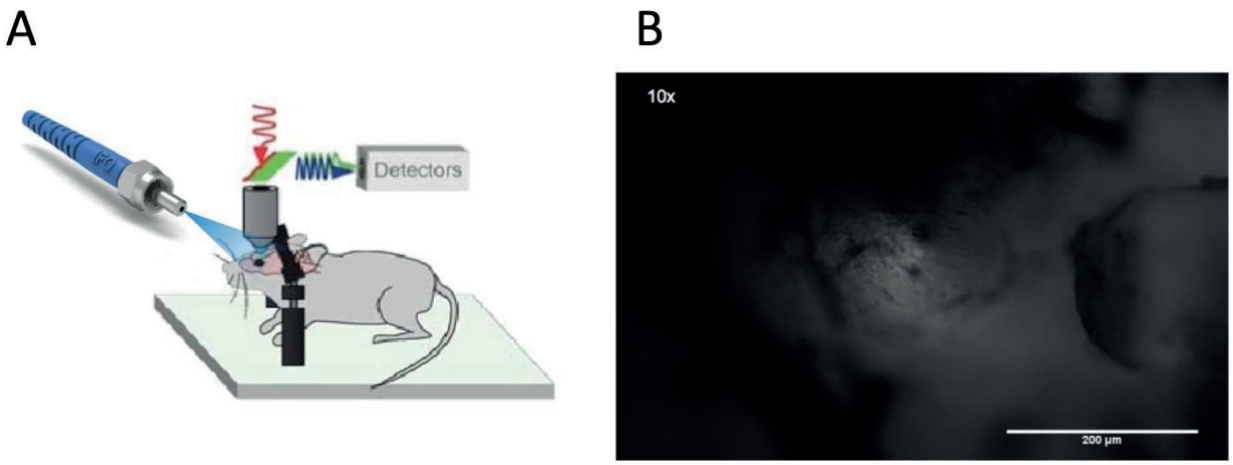

Fig.4.1 (A) Photostimulation experiment set-up (B) SSTR2.6 CNiFER (pre-CRiSPR) (middle) and fiber optic cannula (right) are shown. Cannula has a 200µm diameter.

Analysis of SSTR2.6 (pre-CRiSPR) CNiFER FRET Responses to Photostimulation Cycles

Normalized CNiFER FRET trace was extracted and calculated from two stack of images (CFP and YFP) as described previously (see Chapter 2, Materials and methods: In Vitro Perfusion Data Analysis). CNiFER FRET peak in response to a photostimulation cycle was calculated in several steps. First, the maximum FRET ratio value in the five minutes following the start of a

photostimulation cycle was determined. This maximum value was then averaged with the preceding and following two points. FRET ratio baseline (average FRET ratio value of 10 points preceding the start of a photostimulation cycle) was then subtracted from the averaged maximum value to give the CNiFER FRET peak. Mean CNiFER FRET peak to a photostimulation cycle was calculated by averaging responses in a single animal. Unpaired t-test was conducted to compare SSTR2.6 (pre-CRiSPR) CNiFER and control (Gqi5 Tw2B UR1D6 pre-CRiSPR) CNiFER mean FRET peak responses to a photostimulation cycle . One-way ANOVA was performed to test the effect of LED power/frequency of blue light pulses on the SSTR2.6 CNiFER (pre-CRiSPR) FRET peak response and was followed by Tukey post-hoc test.

Results

To stimulate SST-INs selectively, Sst-Cre driver line was used[87]. This line was crossed with Ai32 mice, a line that has floxed-ChR2-eYFP in the ROSA26 locus[86]. Mice obtained through this cross had dense eYFP+ neurites across all layers including layer 1 (Fig.4.2). The image suggested, even if blue light may not penetrate infragranular layers—where SST-INs cluster— there will be ChR2-expressing SST-IN cell bodies/processes in the upper layers that are

likely to be stimulated.

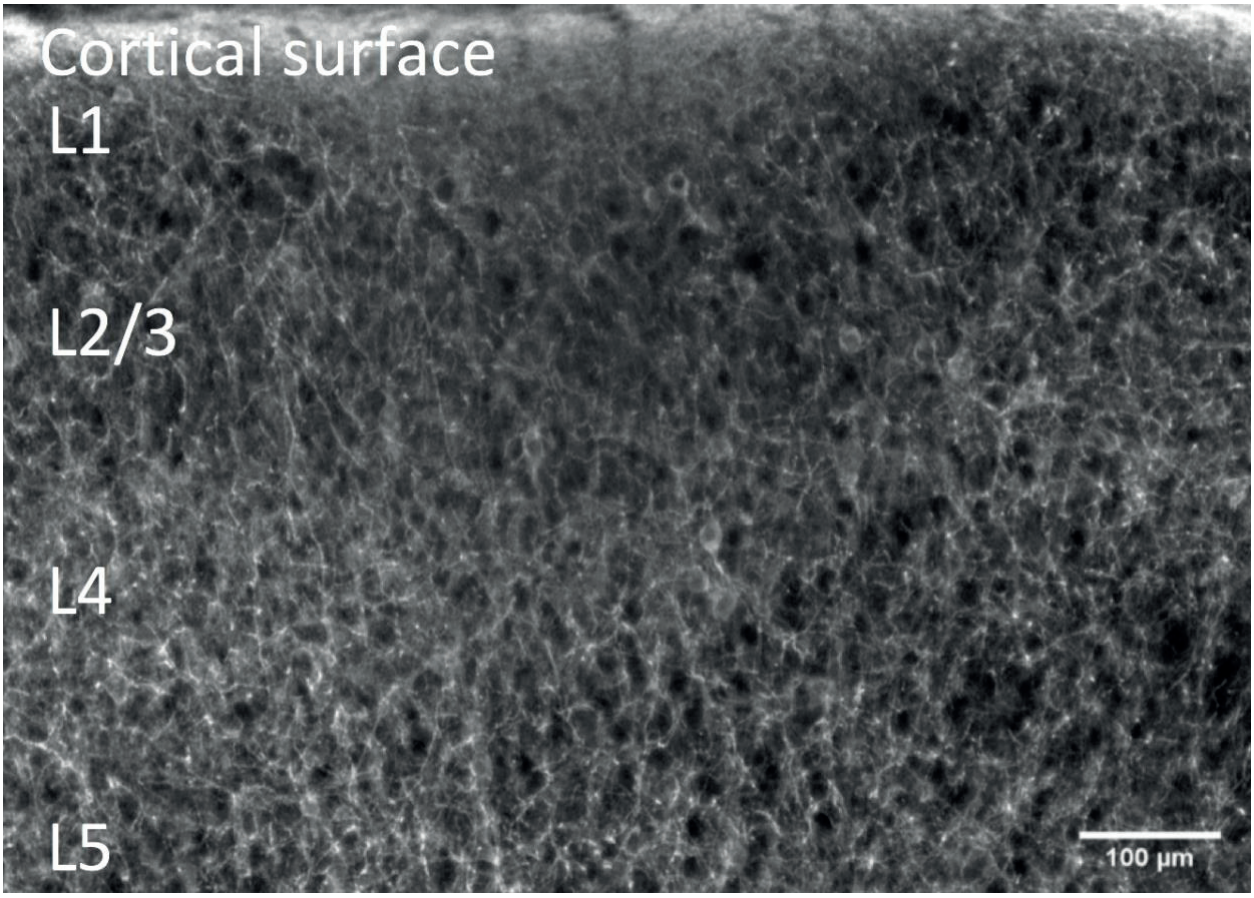

Fig.4.2 A coronal section from a mouse obtained by crossing Sst-Cre driver line with Ai32 mouse (floxed-ChR2-eYFP) is shown. eYFP+ neurites are found across all cortical layers. Photostimulation of ChR2-expresssing SST-INs, and SSTR2.6 (pre-CRiSPR) CNiFER FRET response measurements were made in these mice.

A recent study has reported reduced levels of SST in the cortex of SST-Cre mouse line used in the present study[88]. In homozygous Sst-Cre mice (Sst-Cre Tg/Tg) the drop was reported to be up to 90% from the wild type SST level[88]. Photostimulation experiments performed in Sst-Cre Tg/Tg mice, in the present study, supported this previous finding. SSTR2.6 CNiFER (pre-CRiSPR) did not show FRET changes in response to photostimulation cycles (mean SSTR2.6 CNiFER FRET peak=-0.043 $\pm$ 0.040SEM, N=2 mice) (Fig.4.3)

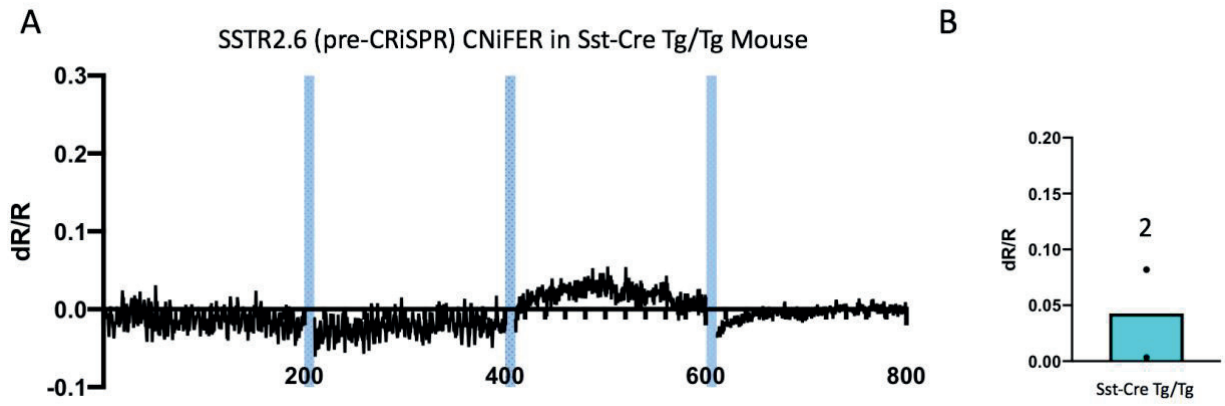

Fig.4.3 (A) SSTR2.6 (pre-CRiSPR) CNiFER FRET trace in a recording, where three cycles of photostimulation (one photostimulation cycle = 4ms light pulses at 30Hz for 30s) were made, is plotted. Each blue bar represents one cycle of photostimulation. SSTR2.6 (pre-CRiSPR) CNiFER was implanted in a Sst-Cre Tg/Tg mouse (also floxed-ChR2 Tg/Tg) (B) Mean SSTR2.6 (pre-CRiSPR) CNiFER FRET peak response to one cycle of photostimulation is plotted. Total number of animals is indicated on top of the bar.

The drop in SST level in heterozygous condition (Sst-Cre 0/Tg) was reported to be less compared to homozygous condition (Sst-Cre Tg/Tg)[88]. Sst level in Sst-Cre 0/Tg was found to be 30-50% less than wild type level of SST[88]. Long-duration CNiFER recordings (>20min) in heterozygous mice (Sst-Cre 0/Tg), in the present study, evidenced the presence of SST in heterozygous condition. SSTR2.6 (pre-CRiSPR) CNiFER implanted in Sst-Cre (0/Tg) mice showed spontaneous FRET responses at a rate of 3 FRET peaks over 10min (mean # of spontaneous SSTR2.6 CNiFER FRET peaks over 10min=3.091 $\pm$ 0.831 SEM, N=4 mice) (Fig.4.4B, C). In contrast, control (Gqi5 Tw2B UR1D6, pre-CRiSPR) CNiFER was mostly silent during the same imaging period (mean # of spontaneous FRET peaks over 10min= 0.624$\pm$0.291, N=2mice) (Fig.4.4 B,C). These results suggested, that SST is present in Sst-Cre (0/Tg) mice while Sst-Cre (Tg/Tg) is deficient; therefore, the following photostimulation experiments were performed in Sst-Cre(0/Tg) mice.

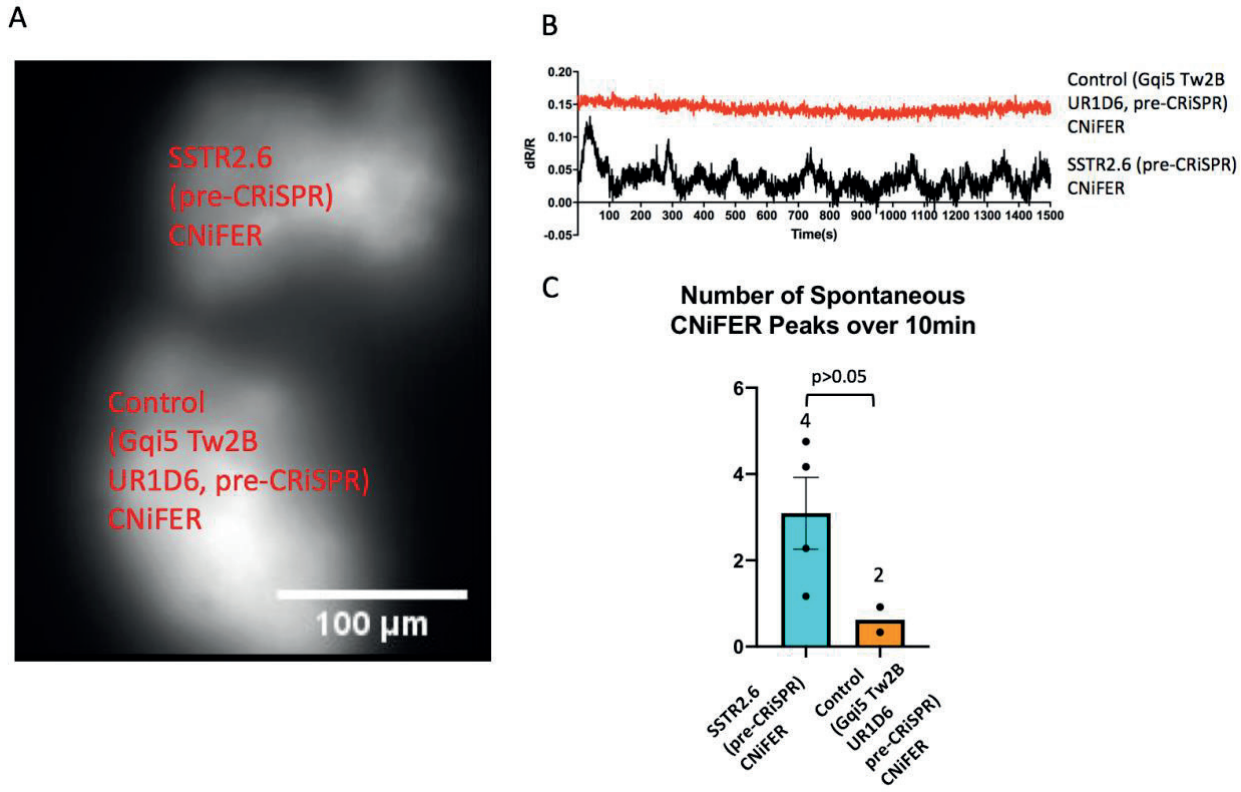

Fig.4.4 (A) Two-photon image of SSTR2.6 (pre-CRiSPR) CNiFER and control (Gqi5 TW2B UR1D6, pre-CRiSPR) CNiFER implanted in a Sst-Cre 0/Tg mouse. Two CNiFERs were imaged simultaneously. (B) SSTR2.6 (pre-CRiSPR) CNiFER and control (Gqi5 TW2B UR1D6, pre-CRiSPR) CNiFER FRET ratio traces in a single recording in a lightly anesthetized (0.5% isoflurane) Sst-Cre 0/Tg mouse are presented.(C) Mean number of FRET peaks over 10min is plotted for SSTR2.6 (pre-CRiSPR) CNiFER and control (Gqi5 TW2B UR1D6, pre-CRiSPR) CNiFER (± SEM). The total number of animals is denoted on top of the bars (unpaired t-test, p>0.05).

SSTR2.6 (pre-CRiSPR) CNiFER implanted in Sst-Cre (0/Tg) mouse showed FRET changes in response photostimulation (mean SSTR2.6 CNiFER FRET peak= 0.076±0.070 SEM, N=3 cycles) (Fig.4.5 B,D). To test the specificity of the SSTR2.6 CNiFER response, photostimulation experiment was repeated with control (Gqi5 TW2B UR1D6, pre-CRiSPR) CNiFER. Control (Gqi5 TW2B UR1D6, pre-CRiSPR) CNiFER did not show FRET changes in response to photostimulation indicating SSTR2.6 CNiFER response is specific and based on somatostatin release. (mean

control (Gqi5 TW2B UR1D6, pre-CRiSPR) CNiFER FRET peak= 0.015±0.003, N=7 cycles; unpaired t-test SSTR2.6 CNiFER vs. control CNiFER (Gqi5 TW2B UR1D6, pre-CRiSPR), p<0.01)

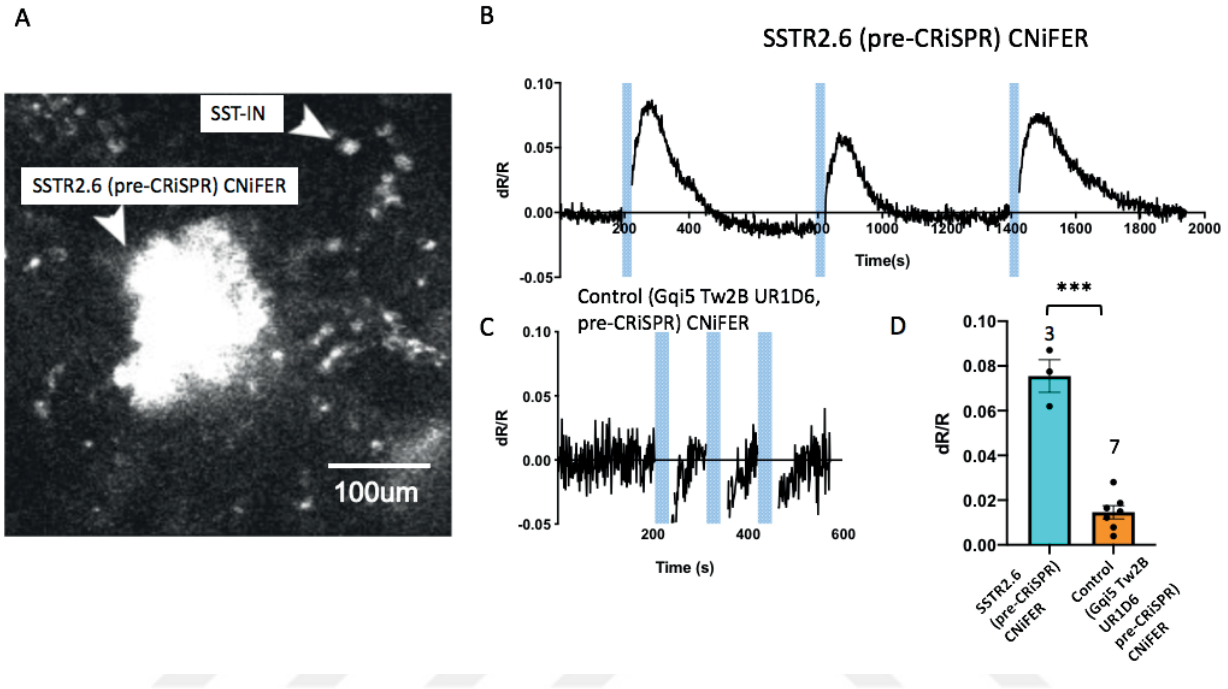

Fig.4.5 (A) Two-photon image of SSTR2.6 CNiFER and ChR2-eYFP+ SST-INs in Sst-Cre (0/Tg) floxed ChR2-eYFP (+/+) mouse. Image is an optical z-section 200um deep from the cortical surface. (B) SSTR2.6 (pre-CRiSPR) FRET trace in a recording, where three cycles of photostimulation were made (one photostimulation cycle = 4ms light pulses at 30Hz for 30s), is presented. Each blue bar represents one cycle of photostimulation. (C) Control CNiFER (Gqi5 TW2B UR1D6, pre-CRiSPR) FRET trace in a single recording, where three cycles of photostimulation were made, is presented. Each blue bar represents one cycle of photostimulation. Note the drop in FRET ratio trace following a photostimulation cycle. The drop is a result of YFP bleaching by 470nm light. (D) Mean SSTR2.6 (pre-CRiSPR) CNiFER and control CNiFER (Gqi5 TW2B UR1D6, pre-CRiSPR) FRET peak response to one cycle of photostimulation is plotted. Numbers on top represent the total number of photostimulation cycles. Data was collected in one mouse. (unpaired t-test, ***p<0.01)

To study the effect of LED power on SSTR2.6 (pre-CRiSPR) CNiFER FRET peak response, SSTR2.6 (pre-CRiSPR) was exposed to photostimulation cycles where LED power was increased progressively (1.3, 2.9, 9.5, 16mW). SSTR2.6 (pre-CRiSPR) CNiFER showed a FRET change in response to photostimulation cycles starting from 9.5mW (mean SSTR2.6 CNiFER (pre-CRiSPR)

FRET peak (at 9.5mW)=0.039±0.004, N=3 cycles) (Fig.4.6A, B). There was a significant effect of LED power on the SSTR2.6 CNiFER (pre-CRiSPR) FRET peak response (ANOVA with post-hoc Tukey test, $p<0.01$). These results suggest the amount of SST release can be modulated with light intensity.

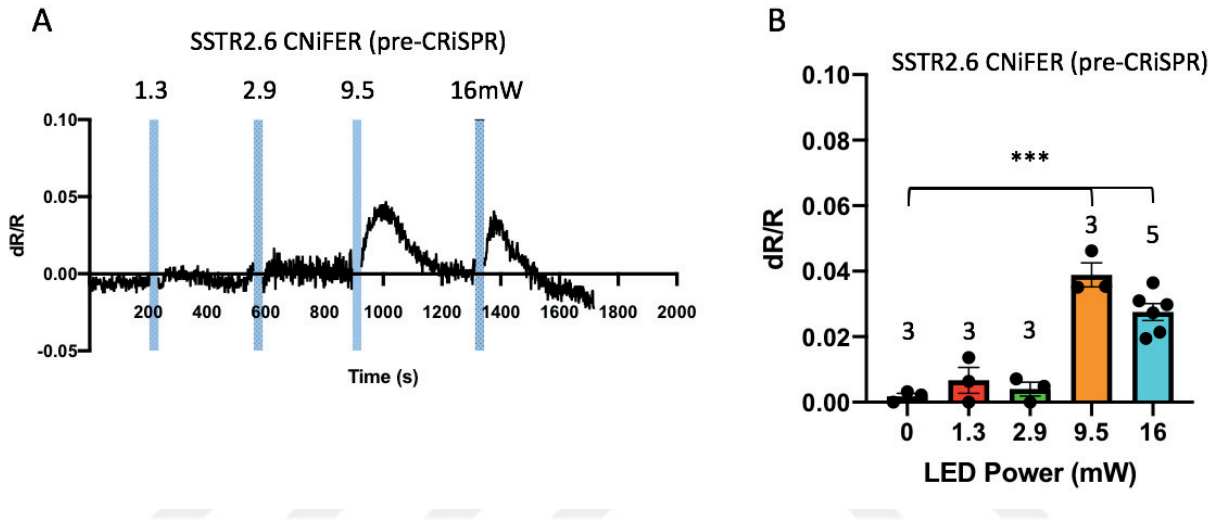

Fig.4.6 (A) SSTR2.6 (pre-CRiSPR) CNiFER FRET ratio trace in a recording, where four cycles of photostimulation were made, each with a higher LED power setting than the previous, is plotted. Each blue bar represents one photostimulation cycle (frequency of blue light pulses in a photostimulation cycle was fixed at 30Hz). (B) Mean SSTR2.6 (pre-CRiSPR) CNiFER FRET peak response to a photostimulation cycle at the indicated LED power setting is plotted (±SEM). Data was collected in one animal. Total number of photostimulation cycles is denoted on top of the bars. There was a significant effect of LED power on the SSTR2.6 (pre-CRiSPR) CNiFER FRET peak response (ANOVA with Tukey post-hoc tests vs. LED-off condition, ***$p<0.01$).

To study the effect of frequency of blue light pulses on the SSTR2.6 (pre-CRiSPR) CNiFER FRET peak response, SSTR2.6 (pre-CRiSPR) CNiFER was exposed to photostimulation cycles, where the frequency of blue light pulses was progressively increased (10, 20, 30, 40Hz) (Fig.4.7A). A significant effect of frequency of blue light pulses on the SSTR2.6 (pre-CRiSPR) CNiFER FRET peak response was found (ANOVA with post-hoc Tukey test, $p<0.01$, N=3 cycles). Thus, the amount of SST release can be modulated by frequency of light pulses.

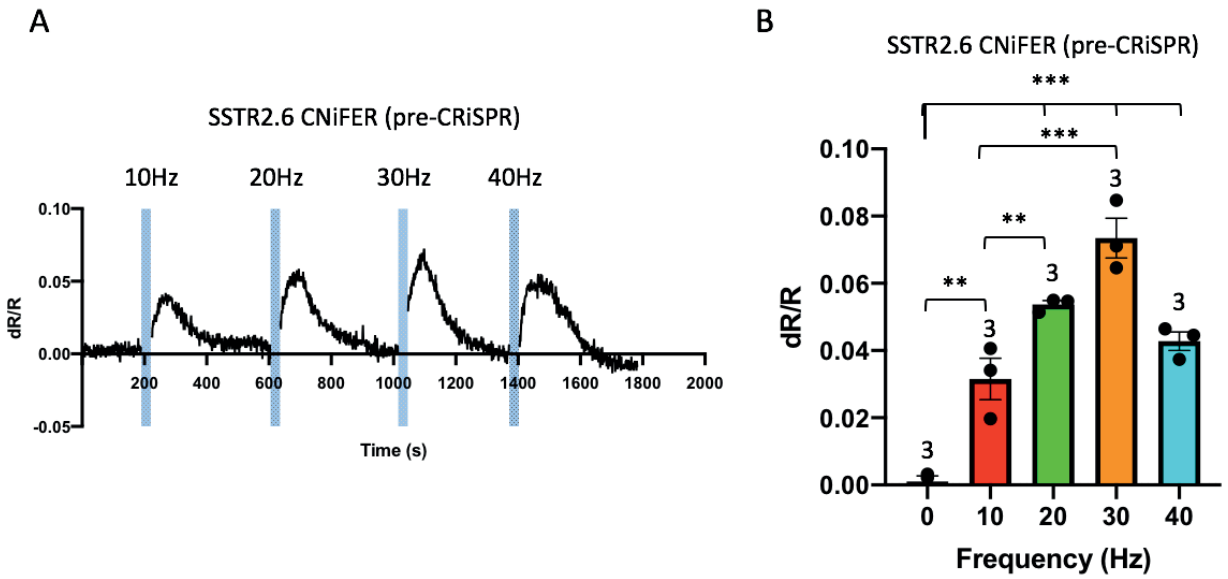

Fig.4.7 (A) SSTR2.6 (pre-CRiSPR) CNiFER FRET trace in a recording, where four cycles of photostimulation were made, each with a higher frequency of blue light pulses than the previous, is plotted. Each blue bar represents one photostimulation cycle (LED power was fixed at 9.5mW). (B) Mean SSTR2.6 (pre-CRiSPR) CNiFER FRET peak response to a photostimulation cycle at the indicated frequency is plotted (±SEM). Total number of photostimulation cycles are denoted on top of the bars. Data was collected in one animal. There was a significant effect of frequency on the SSTR2.6 (pre-CRiSPR) CNiFER FRET peak response (ANOVA followed by Tukey post-hoc tests, **p<0.025, ***p<0.01) Note the drop in CNiFER FRET peak response at 40Hz. A decrease in firing success has been reported for high frequency stimulation of ChR2 variant (ChR2/H134R) used in the present study[89, 90].

The significant effect of LED power on the SSTR2.6 CNiFER (pre-CRiSPR) FRET peak response indicated that SSTR2.6 CNiFER (pre-CRiSPR) FRET peak is influenced by parameters that affect light delivery to the tissue and suggested that larger SSTR2.6 CNiFER (pre-CRiSPR) FRET peak responses can be obtained if blue light pulses are delivered more effectively (Fig.4.6 A). Indeed, replacing 200μm-diameter cannula with a 400μm-diameter cannula in subsequent experiments significantly increased SSTR2.6 CNiFER FRET peak response to photostimulation (mean FRET peak (400μm) = 0.258±0.024SEM, mean FRET peak (200μm)=0.076±0.007, N=3 cycles; unpaired t-test, p<0.025) while control CNiFER (Gqi5 Tw2B UR1D6) FRET response did not change (mean FRET peak(400μm)= 0.005±0.004, mean FRET peak(200μm)= 0.015±0.003,

N=3-7; unpaired t-test, p>0.05)(Fig.4.5B, Fig.4.8A). These results suggest larger cannula size increase the amount of SST release.

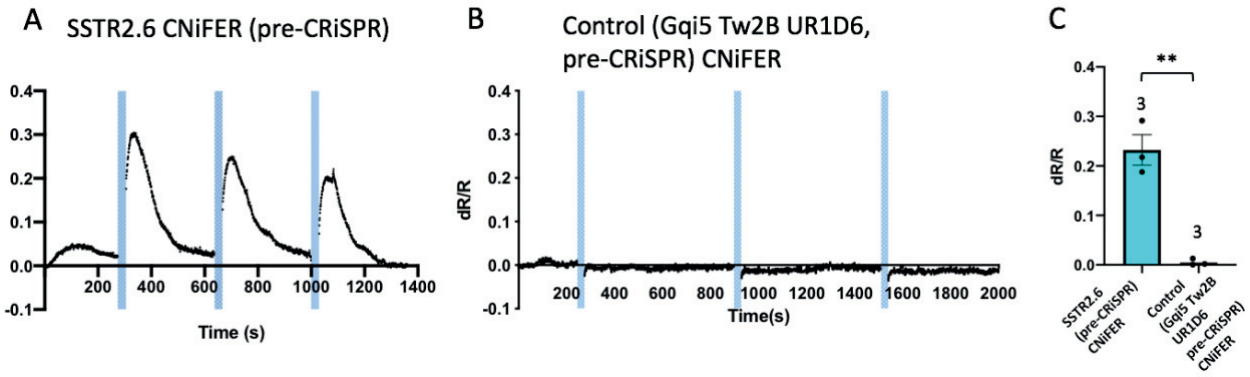

Fig.4.8 (A) SSTR2.6 CNiFER (pre-CRiSPR) FRET ratio trace in a single recording, where three cycles of photostimulation were made (one photostimulation cycle = 4ms light pulses at 30Hz for 30s), is plotted. Each blue bar represents one photostimulation cycle. Light was delivered with a 400μm-diameter fiber optic cannula (B) Control CNiFER (Gqi5 Tw2B UR1D6, pre-CRiSPR) FRET ratio trace in a recording, where three cycles of photostimulation were made (one photostimulation cycle = 4ms light pulses at 30Hz for 30s), is plotted. Each blue bar represents one photostimulation cycle. (C) Mean SSTR2.6 CNiFER (pre-CRiSPR) and control CNiFER (Gqi5 Tw2B UR1D6, pre-CRiSPR) FRET peak responses to a photostimulation cycle are plotted (±SEM). Total number of photostimulation cycles is denoted on top of the bars. Data was collected in one mouse. (unpaired t-test, **p<0.025)

The effect of LED power on SSTR2.6 (pre-CRiSPR) CNiFER FRET peak response was re-examined with 400μm-diameter cannula. Consistent with the previous experiment (4.6 B), there was a significant effect LED power on the SSTR2.6 (pre-CRiSPR) CNiFER FRET peak response (ANOVA with post-hoc Tukey test, p<0.01) (Fig.4.9 B).

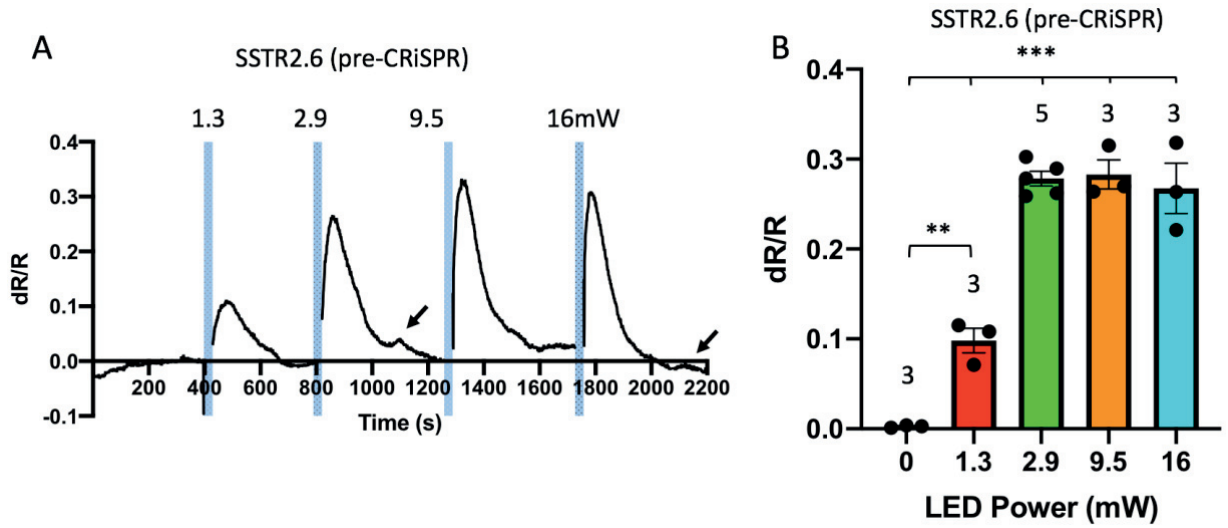

Fig.4.9 (A) SSTR2.6 CNiFER (pre-CRiSPR) CNiFER FRET trace in a recording, where four cycles of photostimulation were made, each photostimulation cycle with a higher LED power setting than the previous, is plotted. Light was delivered with a 400μm-diameter fiber optic cannula. Each blue bar represents one photostimulation cycle (blue light stimulation frequency fixed at 30Hz). Note the smaller FRET peaks present in the FRET trace (arrowheads). Spontaneous SSTR2 FRET peaks were previously detected in heterozygous Sst-Cre mice (0/Tg) (Fig.4.4), but not in homozygous Sst-Cre mice (Tg/Tg) (Fig.4.3) which are deficient of SST[88]. Thus, small peaks are likely to correspond to spontaneous SST release events. (B) Mean SSTR2.6 (pre-CRiSPR) CNiFER FRET peak response to a photostimulation cycle at the indicated blue LED power is plotted (±SEM). Data was collected in one mouse. Total number of photostimulation cycles is denoted on top of the bars. There was a significant effect of LED power on the SSTR2.6 CNiFER (pre-CRiSPR) FRET peak response (ANOVA with post-hoc Tukey's tests, **p<0.025, ***p<0.01).

The effect of frequency blue light pulses on the SSTR2.6 (pre-CRiSPR) CNiFER FRET peak was also re-examined. Similarly, consistent with the previous experiment (Fig.4.7 B), a significant effect LED power on the SSTR2.6 (pre-CRiSPR) CNiFER FRET peak response was found (ANOVA with post-hoc Tukey test, p<0.01) (Fig.4.10 B). Overall, these results suggest the amount of SST released can be modulated with light intensity and frequency of blue light pulses.

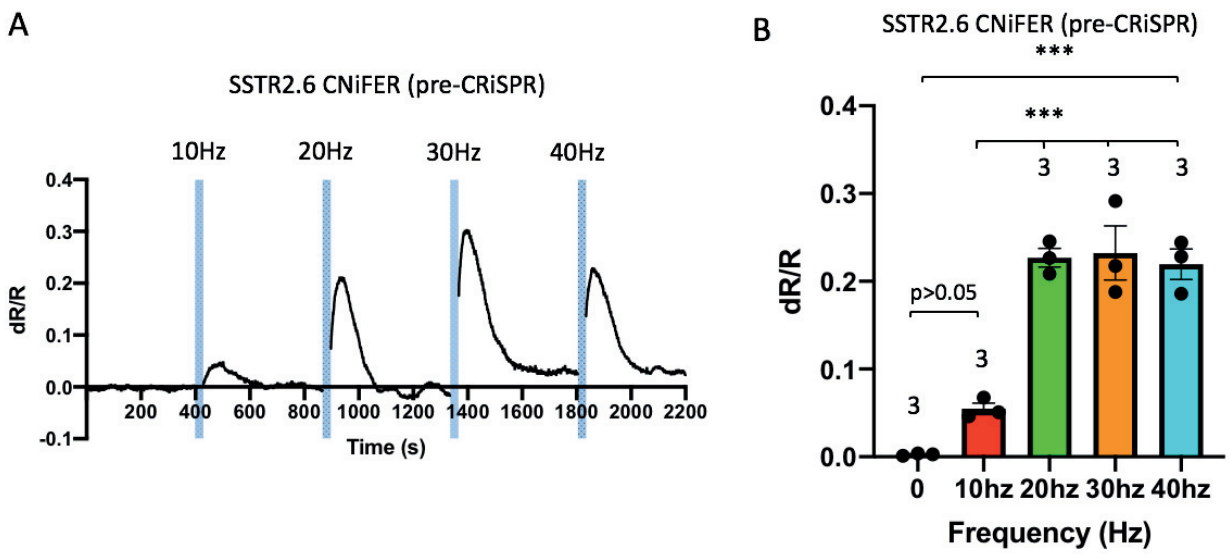

Fig.4.10 (A) SSTR2.6 (pre-CRiSPR) CNiFER FRET trace in a recording, where four cycles of photostimulation were made, each with a higher frequency of blue light pulses than the previous, is plotted. Light was delivered with a 400μm-diameter fiber optic cannula. Each blue bar represents one photostimulation cycle (LED power was fixed at 9.5mW). (B) Mean SSTR2.6 (pre-CRiSPR) CNiFER FRET peak response to a photostimulation cycle at the indicated frequency is plotted (±SEM). Data was collected in one mouse. Total number of photostimulation cycles is denoted on top of the bars. There was a significant effect of frequency of blue light pulses in a photostimulation cycle on the SSTR2.6 (pre-CRiSPR) CNiFER FRET peak response (ANOVA followed by Tukey post-hoc test, ***$p<0.01$)

Discussion

The Sst-Cre mice used in this study was reported to have lower levels of SST compared to wild type [88]. Same study also reported that SST level is partially recovered in the heterozygous condition[88]. In the present study, optical stimulation in homozygous Sst-Cre mice (Sst-Cre Tg/Tg, floxed-Chr2 Tg/Tg) did not lead to a SSTR2.6 (pre-CRiSPR) CNiFER response (Fig.4.3). However, stimulation in heterozygous condition (Sst-Cre 0/Tg,floxed-Chr2 Tg/Tg) resulted in SSTR2.6 (pre-CRiSPR) CNiFER responses (Fig.4.5). Thus, present results are consistent with the previous report of effect of Cre-recombinase knock-in on the Sst-gene expression [88].

In view of this effect, SSTR2.6 (pre-CRiSPR) CNiFER responses seen here are expected to be higher in wild-type mouse.

Whole-cell recording in head-restrained mice has shown that SST-IN has a basal firing rate of 6-7Hz in awake mice[51, 91]. Anesthesia was shown to suppress SST-IN activity[91]. The present study was conducted under light-anesthesia (0.5% isoflurane). Thus, SST-IN activity was likely to be lower than 6-7Hz during these recordings. At this suppressed state of SST-INs, SSTR2 CNiFER has shown FRET peaks at a rate of 3 peaks/10min indicating SST release does not require high frequency stimulation (Fig.4.4). However, a significant effect of light frequency on the SSTR2 CNiFER FRET peak was also detected in subsequent experiments (Fig.4.7, Fig.4.9). These results suggest that SST release occurs at low levels of SST-IN activity and can increase as SST-IN activity goes up.

ChR2(H134R) used in this study is a channelrhodopsin variant with a high photocurrent level compared to wild type ChR2[90]. However, the higher photocurrent level comes at the expense of slower channel kinetics[89]. ChR2(H134R) turns off slower than wild type ChR2 [90]. As a result, ChR2(H134R) fails to open at high frequency stimulation[89]. For instance, at 25Hz stimulation, ChR2(H314R)-expressing neurons respond only half of the light pulses delivered[89]. This slower kinetics of the ChR2(H134R) could explain why there was a drop in SSTR2.6 (pre-CRiSPR) CNiFER FRET peak response at 40Hz photostimulation (Fig.4.7B). The ChR2(H134R) could have started to fail in responding to light pulses after 30Hz decreasing neuropeptide release. Whether SST-INs can be driven to higher rates of firing and higher amounts of SST release can be tested by replacing ChR2(H134R) with an opsin variant that has

faster kinetics. One such variant is ChETA with two times faster channel closing rate than ChR2(H134R) (τ_{off}(ChETA)=7.9ms vs τ_{off}(ChR2(H134R))=17.9ms)[92].

Chapter 5: In Vivo Detection of Somatostatin Released by Cholinergic Stimulation of Somatostatin-Expressing Interneurons

Experiments in chapter 3 demonstrated that photostimulation of ChR2-expressing SST-INs lead to SSTR2.6 (pre-CRiSPR) CNiFER FRET changes. Control CNiFER (Gqi5 Tw2B UR1D6, pre-CRiSPR) did not show FRET changes in response to photostimulation cycles suggesting SSTR2.6 (pre-CRiSPR) CNiFER FRET responses are specific and based on SST release by the SST-INs. However, an SST-release driven by stimulation of SST-INs that express a transgene (ChR2) does not address the question whether SST-INs naturally release SST.

Cholinergic agonists have been shown to increase cortical SST-IN activity [57, 58, 93]. Optogenetic stimulation of cholinergic terminals from the nucleus basalis of Meynert (NBM) increases SST-IN firing[93]. Genetic ablation of SST-IN muscarinic receptors or application of an antimuscarinic drug reverses whisking-evoked activation of SST-INs[43]. To test whether SST-INs can be driven to release SST by cholinergic input, in the present study, SSTR2 CNiFER was imaged during electrical stimulation of ACh release. M1 CNiFER, which allows detection of acetylcholine, was co-implanted with SSTR2 CNiFER to confirm the acetylcholine release.

The study of ACh-evoked SST release required the use of a SSTR2 CNiFER that did not have a non-specific response to ACh. SSTR2.6 (pre-CRiSPR) CNiFER, which was previously shown to have a significant response to ACh, was not suited for the present study (Fig.2.3). Thus, this CNiFER was replaced with SSTR2 5F3 CNiFER, which lacked the HM4 receptor and was previously shown to have lower responses to ACh (Fig.2.5).

Materials and Methods

SSTR2 5F3 (HM4 CRiSPR-edited) CNiFER and NBM Electrode Implantation

CNiFER implantation was the same as previously described (see Chapter 3, Materials and methods). SSTR2 5F3(HM4 CRiSPR-edited) and M1 CNiFERs were implanted in a window centered around C2 barrel column (AP: -1.6mm, ML: 3.3)(Fig.5.1). For ease of identification during imaging, M1 and SSTR2 5F3 (HM4 CRiSPR-edited) pairs were injected on opposite sides of a clear vessel. A monopolar electrode was implanted in nucleus basalis of Meynert (NBM) at (AP: -0.7mm, ML: 1.3, DV: -4.3)(Fig.5.1). Cranial window was sealed with a cover glass for chronic imaging.

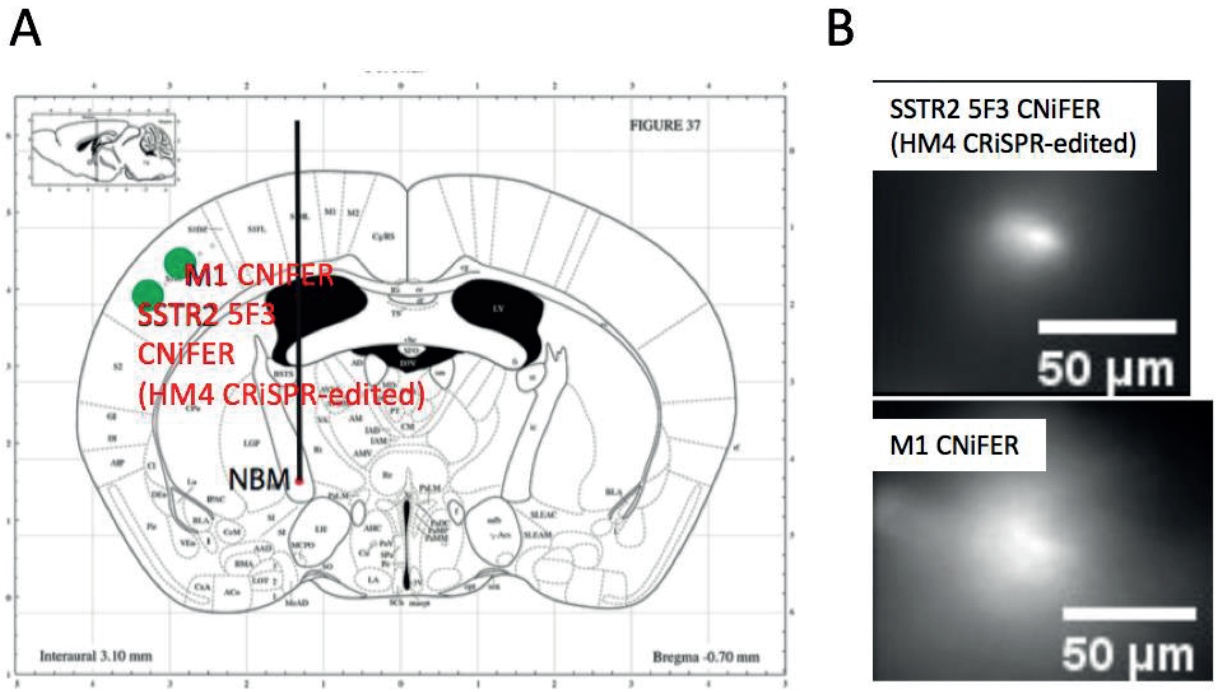

Fig.5.1 (A) SSTR2 5F3 CNiFER (HM4 CRiSPR-edited) and M1 were implanted in primary somatosensory barrel cortex. A monopolar electrode was inserted in nucleus basalis of Meynert (NBM). (B) Two-photon images of SSTR2 5F3 CNiFER (HM4 CRiSPR-edited) and M1 CNiFERs.

NBM Stimulation

NBM was stimulated with a pulse generator controlled by pCLAMP program. Twenty-five 200μs pulses at 50Hz were applied every 2s for 1 min. Current level was 1mA.

Results

M1 CNiFER showed a FRET change in response to NBM stimulation (mean M1 CNiFER FRET peak = 0.075±0.011SEM, N=5 cycles in one animal) (Fig.5.2B, D). NBM stimulation also led to a response in SSTR2 5F3 (HM4 CRiSPR-edited) CNiFER, although the FRET change was lower (mean FRET peak =0.027±0.000SEM, N=3 cycles) (Fig.5.2 C, D). Aligning M1 CNiFER FRET trace with SSTR2 CNiFER FRET trace revealed a time difference between two CNiFER responses (Fig.5 E). SSTR2 CNiFER FRET peak onset was 50s delayed compared to the M1 CNiFER FRET peak. It is notable that the delay is what would be predicted from an acetylcholine-induced SST release.

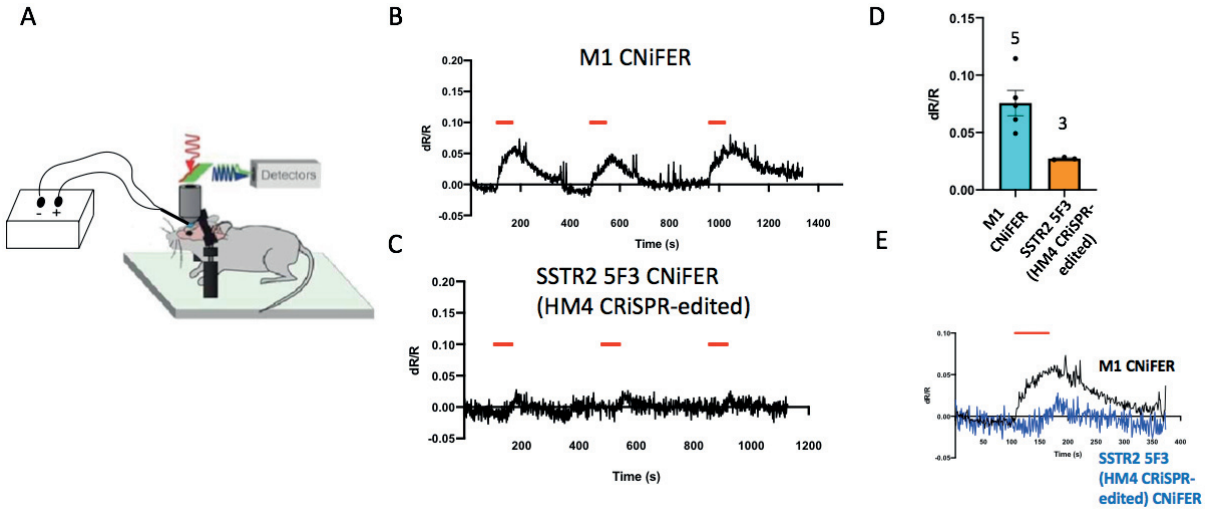

Fig.5.2 (A) NBM stimulation experimental setup (B) M1 CNiFER FRET trace in a recording, where three cycles of NBM electrical stimulation were made (one electrical stimulation cycle = twenty-five 200μs pulses at 50hz were delivered every 2s for a minute), is plotted. (C) SSTR2 5F3 CNiFER (HM4 CRiSPR-edited) FRET trace in a recording, where three cycles of NBM electrical stimulation were made, is plotted. (D) Mean M1 and SSTR2 5F3 CNiFER (HM4 CRiSPR-edited) FRET peak responses to NBM electrical stimulation are plotted (±SEM). Data was collected in one mouse. Total number of NBM electrical stimulation cycles is denoted on top of the bars (E)

M1 and SSTR2 5F3 (HM4 CRiSPR-edited) CNiFER FRET traces are aligned to show the time difference between peaks in response to NBM stimulation.

Discussion

Optogenetic stimulation of VIP-INs in cortical slices inhibits SST-INs[49]. Several studies have shown VIP-INs can be recruited by a variety of input to inhibit SST-INs. For instance, in S1 barrel cortex, stimulation of vibrissal motor cortex (vM1) glutamatergic projections results in SST-IN inhibition[55]. Optogenetic silencing of VIP-INs abolishes this effect[55]. VIP INs can also be stimulated by cholinergic input[58, 94]. VIP-IN activity increases during running[95, 96]. This effect was shown to depend on cholinergic stimulation[95, 96]. In view of these findings, cholinergic recruitment of VIP-INs may explain the small SSTR2 CNiFER responses to NBM stimulation in the present study. NBM stimulation may have suppressed SST-IN activation and SST release via stimulation of VIP-INs.

VIP-IN inhibitory input to SST-INs vary across cortical layers. SST-INs in layer 2/3 and 5 receive stronger VIP-IN input compared to SST-INs located in layers 4 and 6[43]. This bias has been demonstrated to underlie layer-specific distribution of SST-IN activity pattern during whisking, with whisking-activated SST-INs mostly found in layers where VIP-IN input is the weakest[43]. In the current study, SSTR2 CNiFER was implanted in layer2/3 of S1 barrel cortex where whisking-off type of SST-INs predominate[43, 51]. Implanting SSTR2 CNiFER in layer 4, where whisking-on type SST-INs forms the majority may increase the size of small SST responses seen in the present study[43].

Cholinergic agonists depolarize and increase firing of cortical SST-INs[57, 58]. Optogenetic stimulation of basal forebrain projections stimulate SST-IN activity in V1[93].

Knocking out SST-IN muscarinic receptors or application of atropine blocks whisking-evoked activation of SST-INs in S1 barrel cortex[43]. These findings suggest NBM electrical stimulation is expected to lead to an increase SST-IN firing. The effect of NBM stimulation on SST-IN activity was not studied in the present study. SSTR2 CNiFER imaging can be coupled with patch clamp recording in future studies. This would inform about whether SST level changes follow SST-IN firing activity.

The CNiFER used for the NBM stimulation experiment, SSTR2 5F3, was shown to have an ACh response at high concentrations (Fig2.5 B). This non-specific response is presumably associated with M3 receptor that HEK293 cells endogenously express[70]. To show that SSTR2 5F3 response to NBM stimulation is a specific response to SST, several controls can be added to the present study. First, control 128C3 CNiFER response to NBM stimulation can be tested. Control 128C3 CNiFER has a small response to ACh but does not respond to SST at a physiological level (Fig2.4 C. Fig2.5 A). If control CNiFER does not respond to NBM stimulation, this would suggest that SSTR2 5F3 response is specific to SST. Second, NBM stimulation can be performed in SST KO mice (-/-). As these mice are deficient of SST, NBM should not result in an SSTR2 5F3 FRET change. Third, pharmacology can help confirming the specificity of the response. A selective SSTR2 antagonist exists[97]. NBM stimulation in the presence of this SSTR2 antagonist should block SSTR2 CNiFER response.

Chapter 6: Conclusion and Future Directions

In conclusion, in the present study, two CNiFER clones were developed with physiological level sensitivity to SST. One of these clones (SSTR2.6 CNiFER) was used to show that SST can be released by optogenetic stimulation of SST-INs and the amount of release is dependent on the firing rate of SST-INs. A second clone (SSTR2 5F3), which was modified for its non-specific ACh response, was used to demonstrate SST can also be released by cholinergic stimulation of SST-INs.

CNiFERs allow simultaneous imaging of two transmitters. Currently, this is accomplished by implanting two kinds of CNiFERs side-by-side 100μm apart. An alternative strategy is to develop CNiFERs expressing different colored Ca^{2+}-sensors. Two kinds of CNiFERs then can be mixed and implanted in the same location allowing simultaneous measurements on a finer scale. RCaMP sensors are spectrally distinct from the current CNiFER Ca^{2+}-sensors with an emission peak around 600nm, and thus well-suited for a new line of CNiFERs[98]. Red-shifted Ca^{2+}-sensors like RCaMP also facilitate deep two-photon imaging as light scattering is reduced at longer wavelengths[98, 99]. Moreover, RCaMP can be integrated with optogenetics experiments as excitation spectra of RCaMP and ChR2 are well-separated[98].

SSTR2 CNiFER may help finding out whether SST is involved in cortical processing. Various behavioral states are associated with increases in SST-IN activity[43, 82]. For instance, SST-INs firing increases during whisking and before slow-wave activity in NREM sleep[43, 82]. Moreover, SST-INs have been shown to be involved in several microcircuits that modulate pyramidal cell activity [49, 55, 91, 100, 101]. However, it is not known whether SST plays a role in SST-IN modulation of pyramidal cells. Patch-clamp recording of pyramidal cells coupled with

SSTR2 CNiFER imaging may help elucidating whether SST is involved in pyramidal cell modulation.

In human temporal lobe epilepsy patients and kainate-induced rat model of epilepsy, a reduction in hippocampal SST-IN number has been observed[102, 103]. However, it is not clear how this reduction contributes to excitation-inhibition balance in the hippocampal circuitry[104]. Several studies suggest SST-IN loss is compensated [105, 106]. Surviving SST-INs enlarge, sprout axons and form new synapses with granule cells[105]. Moreover, surviving SST-IN have a higher rate of basal firing consistent with the increased frequency of spontaneous EPSCs that is seen in these cells[106]. However, other studies suggest a decrease in inhibition on granule cells —the synaptic target of SST-INs—following seizure-induced loss of SST-INs[107, 108]. For instance, granule cells in epileptic rats were found to be hyperexcitable following pilocarpine-induced seizure [107]. Whole-cell recording of granule cells showed a reduction in miniature and spontaneous IPSC frequencies [107]. Besides changes in synaptic strength of SST-IN input and output, SST level is also affected by seizures[109, 110]. An in vivo microdialysis study shows baseline level of SST is higher in kindled rats compared to controls[109]. Moreover, depolarization by K+ results in a higher level of SST release in kindled animals[109]. However, it is not clear whether this elevated level of SST is associated with an increased level of SST-IN activity in kindled rats. Whole-cell patch clamp recording of SST-INs coupled with SSTR2 CNiFER imaging may elucidate how SST-IN activity relates to increased SST level in kindling-model of epilepsy.

Appendix

The following is published: J. Gen. Physiol. Vol. 149, No. 8, pp. 799–811. Emre Lacin,* Prafulla Aryal,* Ian W. Glaaser, Karthik Bodhinathan, Eric Tsai, Nidaa Marsh, Stephen J. Tucker, Mark S.P. Sansom, and Paul A. Slesinger.

* contributed equally.

It was written by Mark S.P. Sansom and Paul A. Slesinger and is reproduced verbatim.

Dynamic role of the tether helix in PIP_2-dependent gating of a G-protein gated potassium channel

Introduction

G protein–gated inwardly rectifying potassium (GIRK or Kir3) channels are expressed in various regions of the brain, where they control the resting membrane potential and excitability of neurons [111]. Mouse and human molecular genetic studies have indicated a role for GIRK channels in a variety of human disorders, including addiction, alcoholism, Down's syndrome, and depression (for a review, see [112]. Similar to other inwardly rectifying potassium channels, activation of GIRK channels hyperpolarizes the membrane potential, reducing neuronal excitability. A large number of neurotransmitters (e.g., GABA, dopamine, glutamate, serotonin, acetylcholine, and opioid peptides) stimulate G protein–coupled receptors that directly activate GIRK channels [113-117] via G protein Gβγ subunits [118-120]. In addition to G proteins, alcohol has been shown to directly activate GIRK channels. However, GIRK channels remain mostly closed in the absence of activators. The structural mechanism underlying their low probability of opening in the absence of such activators remains poorly understood.

Four different GIRK subunits (GIRK1, GIRK2, GIRK3, and GIRK4) have been identified in mammals [111, 121-123] and each is regulated by the membrane phospholipid phosphatidylinositol 4,5 bisphosphate (PIP_2). [124] showed that depletion of PIP_2 prevents GIRK activation by Gβγ subunits, indicating that PIP_2 is a cofactor for G protein regulation of GIRK channels. In fact, PIP_2 is an essential cofactor for many different types of ion channels. Interestingly, the strength of the PIP_2interaction with the channel can determine the level of

basal channel activity, which varies considerably among different inward rectifiers. For example, constitutively open inward rectifiers, such as Kir2 and Kir4 channels, bind PIP_2 with relatively high affinity and have an open probability of close to 1 [125]W. In contrast, Kir channels that are gated by G proteins, ATP, or ethanol (e.g., Kir3/GIRK, Kir1, and Kir6) exhibit lower relative affinities for PIP_2 and a corresponding lower open probability, suggesting a correlation between the strength of the PIP_2 interaction and open channel probability. GIRK channel activators, such as ethanol and Gβγ subunits, appear to increase the relative affinity for PIP_2, leading to an increase in the frequency and/or channel open time [124, 126, 127]. Conversely, ATP binding to Kir6/SUR channels leads to a reduction in PIP_2 relative affinity [128].

Several laboratories have investigated what determines the relative strength of PIP_2association with Kir channels. Mutagenesis studies originally identified several conserved basic amino acids as well as some hydrophobic residues that influence the strength of PIP_2interaction with the channel [129-131]. Accordingly, the interaction of PIP_2 with GIRK channels could be converted from a weak to a strong interaction by introducing point mutations in the putative PIP_2-binding site, resulting in large agonist-independent currents similar to Kir2 channels [129, 132]. These studies led to the proposal that positively charged basic amino acids form an essential part of the PIP_2-binding site and that changes in the association of PIP_2 with this region of the channel underlie gating of different inward rectifiers. However, how the nature of the interactions with these positively charged amino acids changes during gating is unknown.

Atomic resolution structures of GIRK2 and Kir2.2 channels in the presence or absence of PIP_2 have provided structural details on the molecular interactions underlying PIP_2-mediated

gating of Kir channels [133, 134]. Inward rectifiers possess two gating structures, a G loop gate located at the apex of the cytoplasmic domain and a hydrophobic gate formed by amino acids in the pore-facing M2 transmembrane helices (i.e., helix bundle-crossing [HBC] gate)[111]. Both gates must move sufficiently to support K^+ conduction through the channel pore. A cluster of four basic amino acids in a helical structure, referred to as the "tether helix" (also called the C-linker), appears to coordinate PIP_2 [133, 134]. Curiously, these structural studies reveal only subtle differences in how PIP_2 interacts with Kir2.2 and GIRK2 channels [133-135], with the positive charge appearing to have a dominant role in PIP_2 binding for both channels. Furthermore, the GIRK2 structure solved in the presence of PIP_2 and Gβγ subunits is partially closed, as is the Kir2.2/PIP_2 structure [133-135], suggesting that the binding of PIP_2 to an open channel may look entirely different from the current set of atomic resolution structures. Another limitation with ion channel structures is they represent a static channel and lack the dynamic interactions that occur during gating. Thus, it remains to be determined how the molecular interactions of PIP_2 with the channel protein explain the large differences in resting basal channel activity and subsequent activation among different Kir channels. Here, using a combination of functional electrophysiological studies and molecular dynamics (MD) simulations, we sought to investigate how the highly conserved basic amino acids in the tether helix contribute to channel activation.

Materials And Methods

Molecular biology

The following cDNAs, mouse GIRK2c (Kir3.2c), mouse Kir2.1, human m2R, enhanced yellow fluorescent protein (eYFP), and *Danio rerio* voltage-sensitive phosphatase (*Dr-Vsp*; gift

from Y. Okamura, Osaka University, Osaka, Japan) were cloned in the mammalian expression vector pcDNA3.1 (ThermoFisher). Point mutations were introduced by site-directed mutagenesis (QuikChange II XL, Agilent Technology) and confirmed by automated DNA sequencing. GIRK2* was generated by replacing four native cysteines in GIRK2 (or Kir3.2) channels with thiol-unreactive amino acids (C65V, C190T, C221S, and C321V).

Electrophysiology

Whole-cell patch-clamp recordings were performed 24 to 48 h after transfection [127]. Borosilicate glass electrodes (Warner Instruments) with access resistances ranging from 3 to 6 MΩ were filled with an intracellular solution containing 130 mM KCl, 20 mM NaCl, 5 mM EGTA, 5.46 mM $MgCl_2$ (1.5 mM free Mg^{2+}), 2.56 mM K_2ATP, 0.3 mM Li_2GTP, and 10 mM HEPES (pH 7.4, ~313 mOsm). The extracellular "20K" solution contained 20 mM KCl with 140 mM NaCl, 0.5 mM $CaCl_2$, 2 mM $MgCl_2$, and 10 mM HEPES (pH 7.4, ~318 mOsm). 100 mM ethanol, 1-propanol, or 2-methyl-2,4-pentanediol (MPD) were added directly to the 20K solution. MTS-HE, MTS-Y, and MTS-F (Tocris) were dissolved in DMSO and diluted in 20K solution directly before application to cells. Whole-cell patch-clamp recordings were made as described previously [127].

MD simulations

The crystal structure of the GIRK2 channel bound to a PIP_2 head group was used for MD simulations (see supplemental Materials and methods). We used the Protein Data Bank (PDB): 4KFM structure for simulations, because this channel is in a preopen conformation [133]. We compared the 3SYA and 4KFM structures and determined there is a small RMSD, with the largest movements in the LM loop and a 0.41 Å RMSD for the c-α in the PIP_2 pocket, formed by

residues 88–92 (from the slide helix), 192–203 (HBC gate and tether helix), and 62–64 (N-terminal b-loop). Four 1-stearoyl-2-arachidonoyl-*sn*-glycero-3-phosphoinositol 4,5 bisphosphate (18:0, 22:4 PIP_2) molecules were aligned to the crystal structure of PIP_2, one at each binding site. Gβγ subunits were not included in the calculations. The GIRK2-PIP_2 system was embedded in a bilayer consisting of 202 1-palmitoyl-2-oleoyl-*sn*-glycero-3-phosphocholine (POPC; 16:0, 18:1 PC) lipids using the CHARMM-GUI membrane builder [136, 137]. The protein–lipid system was then solvated with TIP3P water molecules and 150 mM KCl. The CHARMM36 force field was employed [138]. Additionally, five potassium ions were placed in the ion conduction pathway, and four sodium ions were placed in the sodium-binding site as seen in the crystal structures. A second system was set up with the same conditions but with a 6'Y mutation generated by in silico mutagenesis using CHARMM-GUI. The two systems (WT and 6'Y) were subjected to stepwise decreased restraint equilibration used in CHARMM-GUI membrane builder [139]. The two systems (WT and 6'Y) were then equilibrated for 20 ns using positional restrain of 1,000 KJ/mol/nm^2 on all Cα atoms of the protein before the 400-ns unrestrained production simulations. We then repeated the 400-ns production simulations using different initial velocities for both systems. Simulations were conducted using GROMACS 4.6 [140] with a 2 fs integration time step and visualized using VMD, Pymol [141], or Discovery Visualizer 4.0 (Accelrys).

GIRK2 K^+ flux Assay

Mouse GIRK2 (containing amino acids 52–380) was expressed and purified in *Pichia pastoris* (a gift from R. Mackinnon, The Rockefeller University, New York, NY) as described previously [134, 142]. Purified GIRK2 channels were reconstituted into a lipid vesicle mixture

containing POPE/POPG as described previously [134]. For the K^+ flux assay, vesicles were diluted 1:200 into flux buffer containing the H^+-sensitive dye 9-amino-6-chloro-2-methoxyacridine (ACMA), as described previously [134, 142]. Fluorescence quenching was measured using a *Flexstation 3* microplate reader (Molecular Devices). Changes in fluorescence were monitored after the addition of the H^+ ionophore *m*-chlorophenyl hydrazone (CCCP), followed by the addition of 30 µM diC_8-lipids (PI, PI(4)P, PI(5)P, PI(3,4)P_2, PI(4,5)P_2, and PI(3,4,5)P_3; Echelon). The K^+ gradient was collapsed with 50 nM of the K^+ionophore valinomycin, allowing for determination of vesicle capacity at the end of the experiment. The "relative K^+ flux" was calculated by measuring the decrease in fluorescence (i.e., quenching) 900 s after the addition of a vehicle or phospholipid. This decrease in fluorescence was normalized to the basal fluorescence before adding CCCP and to the maximal decrease in fluorescence following the addition of valinomycin (F_v). The leakage flux for the proteoliposomes (no diC_8) was subtracted to give the "fractional activation."

Statistical analyses

Pooled data are presented as mean ± SEM and evaluated for statistical significance (defined as $P < 0.05$ for all tests). An unpaired Student's *t* test was used to compare data from two separate groups. One-way ANOVA was used for comparing three or more groups, followed by Bonferroni post hoc test for comparison between groups when applicable. Where indicated, n represents the number of cells from which the currents were recorded under each condition. All data were analyzed using Excel (Microsoft) and Prism (GraphPad).

Results

Critical role for the 6' lysine in the tether helix for PIP_2-dependent gating

To better understand the structural mechanism underlying PIP_2-dependent gating of GIRK channels, we evaluated the role of the positively charged, basic amino acids in the tether helix [133, 134]. To facilitate a comparison with the previous studies that have examined these highly conserved charged residues, we propose a numbering system whereby the first of these highly conserved residues (K194 in GIRK2) is defined as the 0' position (0'K), K199 as 5'K, and K200 as 6'K (Figs. 1 a and S1 a).

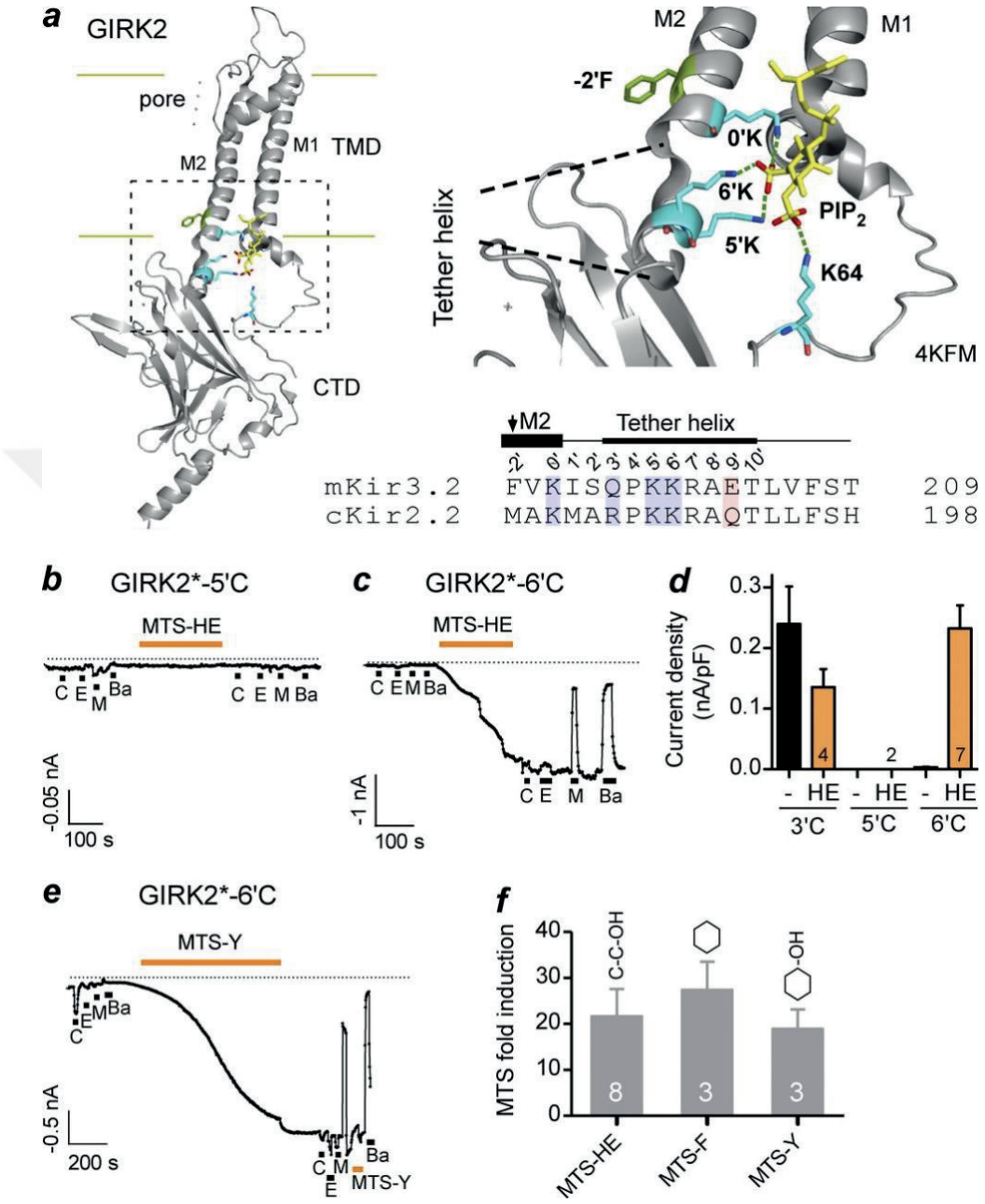

Fig 1 The positive charge at 6'K is not essential for activation of GIRK2 channels. (a) Model shows a single subunit of GIRK2 (PDB: 4KFM), highlighting the region involved in binding PIP_2. Four lysines form hydrogen bonds with the 4' and 5' phosphates of PIP_2. Amino acid sequences of the tether helix for mouse GIRK2 (Kir3.2) and chicken Kir2.2 are shown below with the proposed number system. Arrow indicates HBC. (b) Current trace for GIRK2*-5'C shows little effect of 5 µM carbachol (C), 100 mM ethanol (E), 100 mM MPD (M) or Ba^{2+}before or after exposure to 1 mM MTS-HE. Vh= −100 mV. (c) Current trace for GIRK2*-6'C shows large activation of basal current with 1 mM MTS-HE. Note the inhibition of MTS-HE–activated current with both Ba^{2+} and MPD. (d) Bar graph shows mean increase in basal current density (pA/pF) measured at −100 mV. (e) Current trace for GIRK2*-6'C shows large activation of basal current

with 0.1 mM MTS-F. (f) Mean fold-induction of basal current with 0.1 mM MTS-HE, 0.1 mM MTS-F, and 0.1 mM MTS-Y for GIRK2*-6'C. Bars show mean ± SEM. Figure is reproduced from Lacin et al. 2017.

In the GIRK2/PIP_2/Gβγ atomic structure (PDB: 4KFM), which is considered to be in a preopen conformation [133], 0'K, 5'K, and 6'K in the tether helix form hydrogen bonds with the 5' phosphate (5'-PO_4) of PIP_2 (Fig. 1 a). In the Kir2.2/PIP_2 structure (PDB: 3SPI), the 0'K and 5'K form hydrogen bonds with the 5'-PO_4, but the 6'K forms a hydrogen bond with the 4'-PO_4 (Fig. S1 b; [135]. Thus, the 6'K in the tether helix of GIRK2 and Kir2.2 interact with different phosphates on the inositol ring of PIP_2. Given these variations in how PIP_2 is coordinated in the GIRK2 and Kir2.2 structures, we hypothesized that this region of the tether helix may be important for regulating the PIP_2-dependent gating of GIRK2 channels.

To test this idea, we used a strategy of chemical modification in which a single cysteine is introduced at 5'K or 6'K and is then probed with a membrane permeant MTS compound. This technique has the advantage of enabling the study of a channel before and after modification and has been used previously to probe gating structures of inwardly rectifying potassium channels [127, 131, 143, 144]. Here, we focused on the effect of MTS hydroxyethyl (HE), which would covalently attach a CH_2-CH_2-OH side chain to the sulfhydryl of the engineered cysteine, mimicking a serine/threonine type of amino acid substitution, i.e., a polar, uncharged residue. We introduced the cysteine into a GIRK2 channel that was modified to contain no other internal cysteines (referred to as GIRK2*). GIRK2* was shown previously to retain both Gβγ- and alcohol-dependent activation [127]. Using whole-cell patch-clamp recordings from HEK293 cells transiently transfected with GIRK2*-5'C or GIRK2*-6'C cDNA, along with the m2 muscarinic receptor cDNA, we measured the basal, m2 muscarinic receptor–activated and alcohol-

activated GIRK2 currents before and after MTS modification [127]. In HEK293 cells expressing GIRK2*-5'C, there was little activation by carbachol or alcohol, and transfected cells did not show any appreciable Ba^{2+}-sensitive basal currents. Bath application of MTS-HE (0.1–1 mM) for ~5 min did not appear to alter the basal currents (Fig. 1 b; *n* = 2). Expression of GIRK2*-6'C in HEK293 cells also produced currents that were small and relatively insensitive to 5 μM carbachol or 100 mM alcohols (Fig. 1 c). In contrast to 5'C, however, bath application of 1 mM MTS-HE dramatically increased the amplitude of the Ba^{2+}-sensitive basal current for GIRK2*-6'C channels (Fig. 1, c and d). The neighboring 3'C in the tether helix also showed no increase in basal current with MTS-HE (Fig. 1 d). For 6'C, the basal current density increased from −3.4 ± 0.8 pA/pF to −232.2 ± 38.0 pA/pF (*n* = 7) and was now inhibited by ~90% with MPD (−89.5% ± 6.9%, *n* = 7) after modification with MTS-HE.

We next examined the effect of two other membrane-permeant MTS reagents, 0.01 mM MTS-phenylalanine (F) and 0.1 mM MTS-tyrosine (Y). Like MTS-HE, MTS-Y and MTS-F dramatically increased the Ba^{2+}-sensitive basal currents by ~20-fold (Fig. 1, e and f). These results demonstrate that the positive charge of 6'K is not essential for MTS activation of GIRK2*-6'C channels. In addition, MPD inhibited the MTS-activated basal currents from 60% to 100% after modification with MTS-F and MTS-Y (Figs. 1 e and S2). A large agonist-independent basal current and inhibition with MPD are features of a constitutively active GIRK2 and Kir2.1 channels [145]. These results demonstrate the Cys at the 6' position is unable to support channel activation (i.e., little Ba^{2+}-sensitive current), but modification with a larger uncharged side chain (e.g., Y or F) greatly activates the channel.

With the MTS modification experiments, there are four cysteines per tetrameric channel that can be modified but the exact stoichiometry of modification is unknown. To study the effect of four substitutions per tetramer, we engineered a single point mutation at 6'K in GIRK2*. We predicted that a conserved charged substitution at this position (i.e., K200R [6'R]) would produce a channel with a small basal current and normal alcohol modulation, whereas a phenylalanine or tyrosine substitution would most closely mimic modification with MTS-F or MTS-Y (i.e., increase the basal current and change alcohol activation). Expression of GIRK2*-6'R produced channels with a small Ba^{2+}-sensitive basal current, which was activated by ethanol, propanol, and MPD, similar to GIRK2* channels (Fig. 2, a–d). In contrast, mutation of this positively charged residue to a tyrosine (GIRK2*-6'Y) produced large Ba^{2+}-sensitive basal currents that were relatively insensitive to alcohols, similar to MTS-Y modification of 6'C. Expression of GIRK2*-6'F produced Ba^{2+}-sensitive basal currents that were inhibited by MPD, similar to MTS-F modification of 6'C, but the basal current was not significantly larger (Fig. 2, c and d). Collectively, these results suggest that a Tyr side chain at the 6' position of the tether helix may strengthen the interaction with PIP_2, leading to a large basal current and small alcohol response [145].

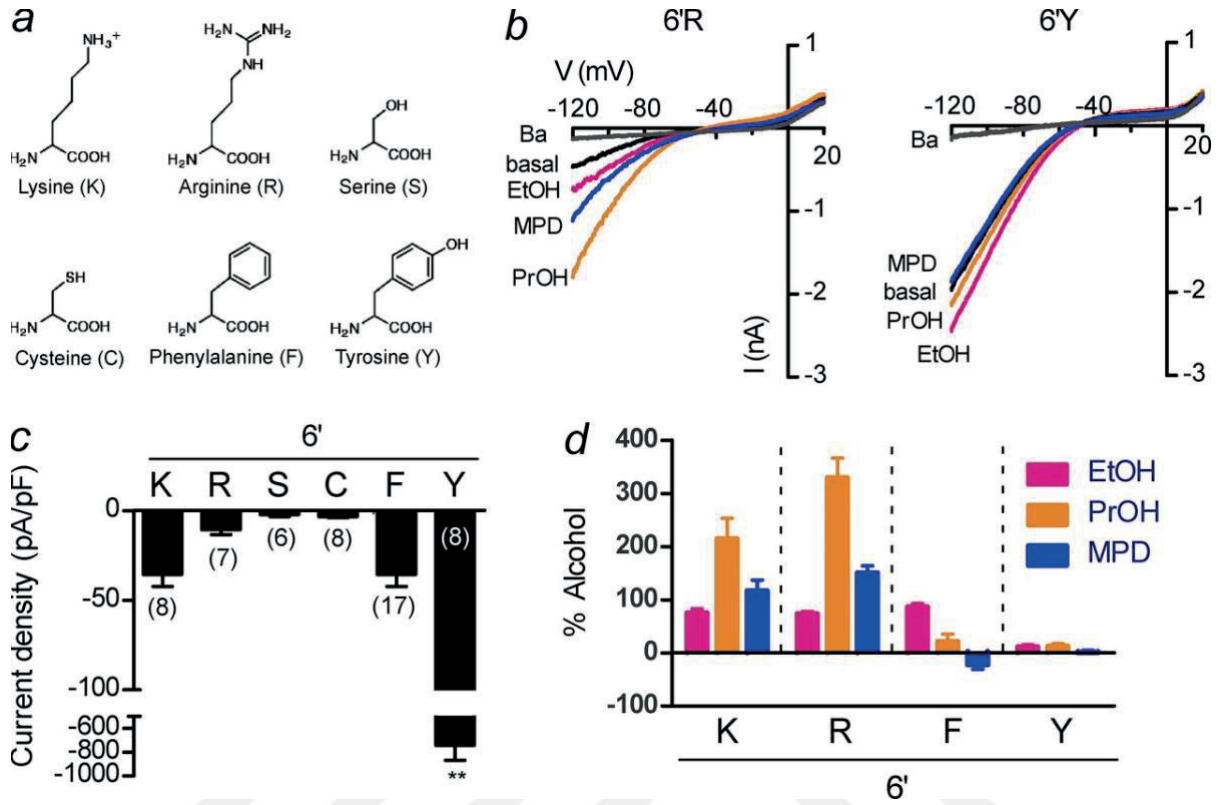

Fig 2 A tyrosine substitution at 6'K increases agonist-independent basal current. (a) Structures of amino acids introduced at 6'K in GIRK2. (b) Current–voltage plots show the change in inwardly rectifying current with different alcohols and Ba^{2+} for 6'R and 6'Y. (c) Bar graph shows change in current density with different substitutions at 6'K. Note the significantly larger current for 6'Y (**, $P < 0.05$). (d) Mean percentage change in current, relative to the Ba^{2+} basal, for 100 mM ethanol (EtOH), 100 mM 1-propanol (PrOH), or MPD (100 mM) with different amino acid substitutions at the 6' position. Note the reduced alcohol responses for 6'Y (n = 8–18). Bars represent mean ± SEM. Figure is reproduced from Lacin et al. 2017.

To probe for possible changes in the relative association of PIP_2 with the channel, we studied the effect of reversibly depleting plasma membrane PIP_2 on whole-cell Kir currents using the voltage-activated phosphatase *Dr-VSP* [127, 146, 147]. Previous studies showed that activation of *Dr-Vsp* by depolarizing the membrane to +100 mV for varying lengths of time produces a time-dependent, graded depletion of PIP_2 and a corresponding reduction in Kir current [127]. To examine the relative association of $PIP_2$with GIRK2*-6'Y channels, we coexpressed *Dr-Vsp* with 6'Y channels and studied the effect of varying length prepulses to +100 mV on the GIRK current measured at −120 mV (Fig. S3). Longer depolarization times led to

more rapid and complete depletion of membrane-bound PIP_2. Both 300 and 500 ms prepulses reduced the steady-state basal current, reaching a maximal inhibition of ~70% of the Ba^{2+}-sensitive basal current (0.7 fractional inhibition; Fig. 3, a and d). The 30% residual current could reflect tightly bound PIP_2 or a change in PIP selectivity and was not examined further. In contrast, activation of *Dr-Vsp*with shorter prepulses (e.g., 50 or 100 ms) reduced ~100% of the basal current for WT GIRK2*-6'K channels (Fig. 3, b and d). For comparison, we also measured the *Dr-Vsp* sensitivity of Kir2.1 channels, which are known to bind PIP_2 with higher relative affinity [124, 148]. Expression of Kir2.1 produced large Ba^{2+}-sensitive basal currents that were partially inhibited by 100 mM propanol (Fig. 3, c and d), similar to previous results [149, 150]. Activation of *Dr-Vsp* for 50 or 100 ms produced little change in the basal current, whereas a 500 ms prepulse significantly reduced the Ba^{2+}-sensitive basal currents by ~90% (Fig. 3, c and d).

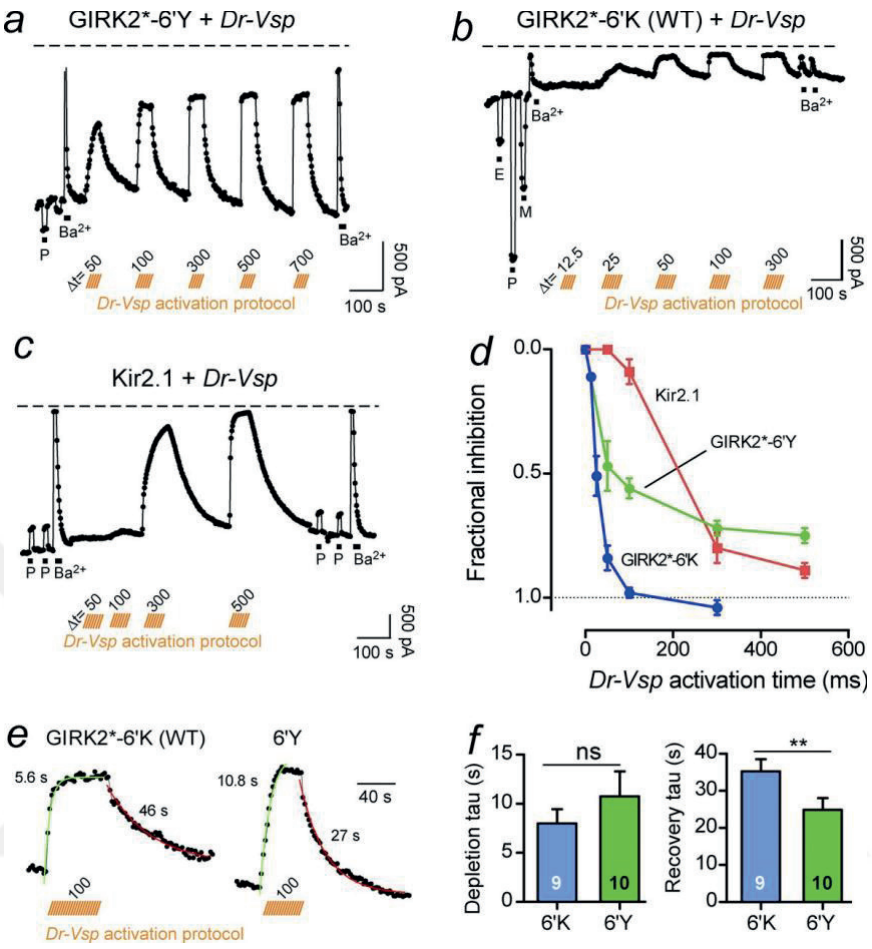

Fig 3 GIRK2 6'Y channels display altered association for PIP_2. (a–c) The current is plotted as a function of time for a cell expressing *Dr-Vsp* with GIRK2*-6'Y (a), GIRK2*-6'K (WT; b), or Kir2.1 (c) channels. V_h = −120 mV. Voltage-dependent (+100 mV) activation times for *Dr-Vsp* are indicated by orange bars. 100 mM 1-propanol, 100 mM ethanol, or 100 mM MPD (P, E, and M, respectively) and 3 mM Ba^{2+} were applied before and after *Dr-Vsp* activation. (d) Fractional inhibition of steady-state basal current is plotted as a function of different *Dr-Vsp* activation times. Note the rank order of Kir2.1 > GIRK2*-6'Y > GIRK2* depletion time. *n* = 7–10. (e) Representative examples of GIRK current depletion and recovery after 100 ms activation of *Dr-Vsp* at +100 mV. V_h = −120 mV. Best-fit single exponentials with time constants are shown. (f) Mean tau (s) for depletion and recovery of current following Dr-Vsp–dependent depletion. **, P < 0.05; ns, not significant; Student's *t* test. Bars represent mean ± SEM. Figure is reproduced from Lacin et al. 2017.

We next analyzed the rates of current depletion and recovery after *Dr-Vsp* activation by fitting the decay of current with a single exponential and determining the time constant (tau).

These rates correlate with the differences in PIP_2 affinity, where higher-affinity channels

typically have a slow depletion and fast recovery [127, 146, 147]. The rate of recovery depends on both the relative affinity of the channel for PIP_2 and the rate of resynthesizing membrane-bound PIP_2. We assume the latter is similar when comparing different channels. We found that the tau for depletion was not significantly different for 6'K and 6'Y channels, but the tau for recovery was significantly faster for GIRK2*-6'Y (Fig. 3, e and f), 24.9 ± 3.2 s (*n* = 10) for 6'Y, and 35.8 ± 3.4 s (*n* = 9) for 6'K. This faster recovery for 6'Y supports the interpretation of a stronger PIP_2 interaction [127, 146, 147, 151].

MD simulations of PIP_2-dependent gating

To gain structural insights into how 6'Y might play a critical role in determining PIP_2 interactions, we conducted atomistic MD simulations to investigate possible differences in the PIP_2 pocket. GIRK2 (6'K; WT) or GIRK2 6'Y channels were embedded in a POPC bilayer containing four PIP_2 lipids with their head groups aligned onto their crystallographic positions. Using a starting condition defined as a preopen conformation, as depicted in the 4KFM structure [133], we examined the dynamics of PIP_2 interaction with the WT (6'K) or 6'Y channel in the absence of Gβγ subunits during 400-ns simulations (Fig. 4; see Materials and methods for details). During simulation of the WT channel, the side chain of 6'K appears flexible and adopts a downward orientation, away from the transmembrane domains (TMDs). Furthermore, the 5' phosphate group of PIP_2 also moves downward away from 0'K in the pocket, forming a new set of interactions (Fig. 4 a, top; and Videos 1 and 2). In the 6'Y channel simulations, on the other hand, the 6'Y side chain maintains an upward orientation (i.e., points toward the lipid bilayer), and the 5'-PO_4 of PIP_2 appears to be more stably bound in its canonical site (Fig. 4 a, bottom; and Videos 3 and 4). To characterize the dynamics of these interactions,

we examined the frequency of hydrogen bond formation with the 5′-PO_4 of PIP_2 of one chain in the 6′K or 6′Y channel over the 400-ns simulation (Fig. 4 b). The time-dependent plots show that the 0′K and 5′K form hydrogen bonds with the 5′-PO_4, and at ∼100 ns, the hydrogen bonds break as the PIP_2 molecule appears to move away from its canonical binding site (Fig. 4 b, blue trace). Coincident with this change, the negatively charged glutamate at 203 (E203; 9′E) forms a hydrogen bond with 6′K, whereas K64 forms a hydrogen bond with 5′-PO_4. In the 6′Y channel simulations, however, both 0′K and 5′K maintain stable hydrogen bonds with the 5′-PO_4 throughout the simulation, in parallel with the 6′Y forming a stable hydrogen bond to the same phosphate (Fig. 4 b, green trace). Furthermore, the 9′E does not form any hydrogen bonds with 6′Y.

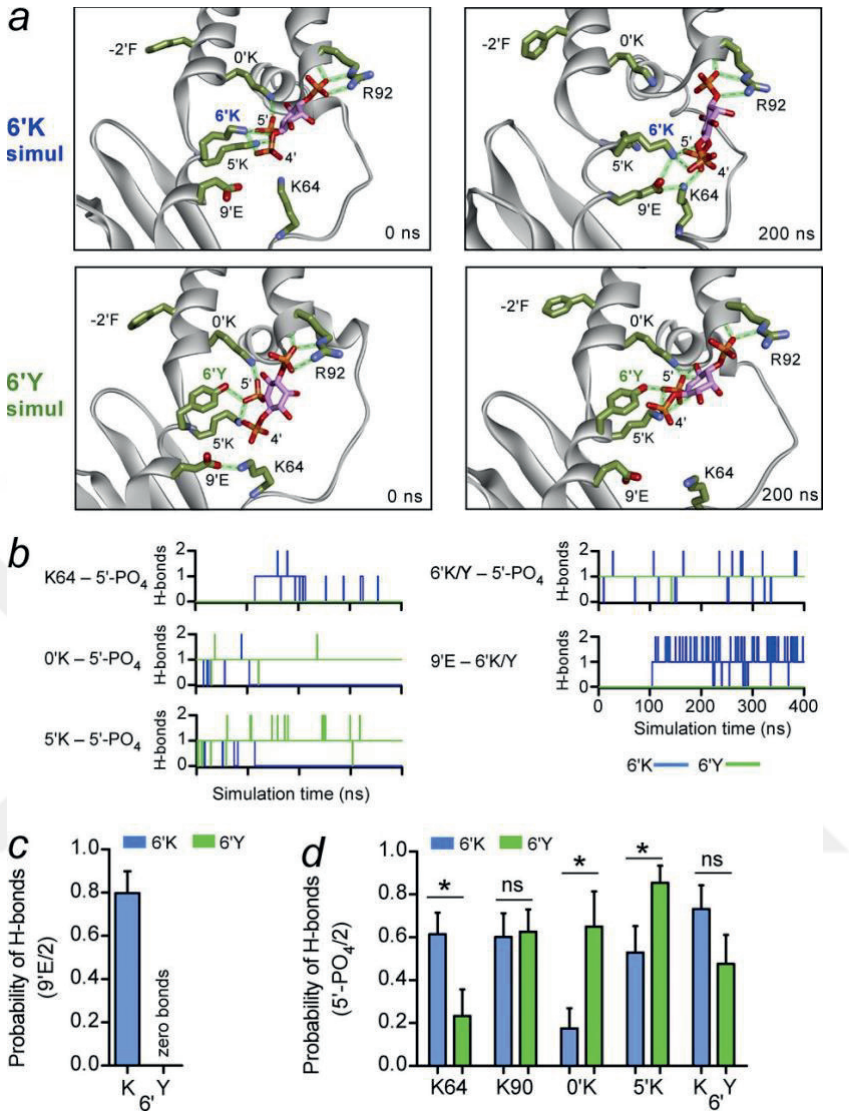

Fig 4 Dynamic change in hydrogen bonding with PIP_2 in GIRK2-6'K and GIRK2-6'Y MD simulations. (a) Examples of GIRK2/PIP_2 structures at the start and after 200 ns of MD simulations for GIRK2-6'K (WT) and GIRK2-6'Y channels. Note the 5'-PO_4 of PIP_2 moves away from starting position in the WT simulation. In contrast, the 5'-PO_4 of PIP_2 appears to engage PIP_2 more deeply in the pocket in the 6'Y channel. One of four subunits is shown. (b) Each graph plots the number of hydrogen bonds during the 400-ns simulation time for the indicated pairs for WT GIRK2-6'K (blue) and GIRK2-'Y (green) for the PIP_2 binding pockets shown in a. (c and d) Bar graphs show the mean relative probability of hydrogen bonds for all four subunits during the two 400-ns simulations for GIRK2-6'K (blue) and GIRK2-6'Y (green) channels. (c) Probability of hydrogen bonding between 9'E and 6'K/Y. (d) Probability of hydrogen bonding for K64, K90, 0'K, 5'K, and 6'K/Y with 5'-PO_4 of PIP_2 (of two maximal bonds). Note the number of hydrogen bonds increases with 0'K and 5'K but decreases for K64 with the 6'Y channel simulations. Bars represent mean ± SEM. *, $P < 0.05$; ns, not significant; Student's *t* test. Figure is reproduced from Lacin et al. 2017.

We repeated the 400-ns simulations (simulation 2) to determine the reproducibility, and similar results were observed in the second simulation (Fig. S5, simulation 2). To quantify these observations, we calculated the probability of hydrogen bond formation between the 1', 4', or 5' phosphate of PIP_2 and GIRK2 for all four pockets in both 400-ns simulations (Fig. 4, c and d; and Figs. S4 and S5). Interestingly, we found that the highest probability of hydrogen bonds with PIP_2 occurs between the side chain and backbone amide of R92 with the 1'-PO_4 in both WT 6'K and 6'Y simulations (Figs. S4 a and S5). This finding raises the possibility that R92, which is at the bottom of the M1 helix, serves as an anchor point for interactions of 1'-PO_4 of PIP_2 with the channel, whereas the 4'-PO_4 and 5'-PO_4 interact more dynamically with the tether helix and N-terminal hairpin.

The probability of hydrogen bonds with the 5'-PO_4 of PIP_2 significantly increased for the 0'K and 5'K in the 6'Y channel simulation (Fig. 4 d). Concurrent with these changes, the probability of hydrogen bonds between K64 and 5'-PO_4decreased, whereas K64 hydrogen bonds with the 5'K increased in the 6'Y channel simulation (Figs. 4 d and S4 b). The probability of hydrogen bonds between the 4'-PO_4 of PIP_2 and K64 was unchanged but increased with the 5'K in the 6'Y channel simulation (Fig. S4 b). Furthermore, the 6'Y does not hydrogen bond with 9'E in the 6'Y simulation, allowing only hydrogen bond interactions with 5'-PO_4 (Fig. 4, c and d). Collectively, the 6'Y simulations appear to show a strengthening of the interaction of the 5'-PO_4 of PIP_2 with the 0'K and 5'K, limiting the downward movement of PIP_2 away from the channel's PIP_2-binding pocket (Fig. 4, a–d).

The MD simulations also revealed an important interaction of the 6'K with the 9'E, as the 6'K adopts a downward orientation (Fig. 4 a). The positively charged 6'K forms a significant

number of hydrogen bonds with 9'E that are absent in the 6'Y channel (Fig. 4 c). The 9'E also forms hydrogen bonds with K64 in the MD simulations (Fig. S4 c). In the 6'Y mutant channels, however, the number of hydrogen bonds significantly decreases between K64 and the 5'-PO_4 of PIP_2(Fig. 4 d). Thus, a trifecta of hydrogen bond interactions among 6'K, 9'E, and K64 may determine the extent of hydrogen bonding between PIP_2 and the 0'K and 5'K sites in the channel. Collectively, the MD simulations provide a tenable model for how 6'Y might promote the channel to interact more strongly with PIP_2; anchored by the 1'-PO_4 at R92, the tyrosine substitution (6'Y) supports movement of PIP_2 deeper into the pocket toward the 0'K and 5'K.

In vitro assessment of 5'-PO_4 in activating GIRK2 channels

The MD simulations indicate a prominent role for 5'-PO_4 of PIP_2 in GIRK2 channel gating. To test the role of the 5'-PO_4 in channel activation, we examined effect of different soluble forms of phosphoinositides (e.g., diC_8-PI(4,5)P_2) on GIRK2 activation using purified GIRK2 channels reconstituted into proteoliposomes [134, 142]. Potassium flux through GIRK channels was monitored via a fluorescence-based K^+ flux assay (Fig. 5 a; [134]. With GIRK2-containing liposomes loaded with the pH-sensitive ACMA dye, the addition of the proton ionophore CCCP results in quenching of the ACMA dye if GIRK2 channels are open (i.e., H^+ enters via CCCP if K^+ can exit the proteoliposome; Fig. 5 a; [133]. As expected, diC_8-PI(4,5)P_2, the soluble form of the predominant phosphoinositide found in the plasma membrane [152], produced maximal activation of purified GIRK2 channels (Fig. 5, b and c). PI(3,4,5)P_3 elicited a K^+ flux comparable to that of PI(4,5)P_2, whereas PI(3,5)$P_2$and PI(3,4)P_2 produced an intermediate K^+ flux (Fig. 5 b). As shown previously [153, 154], PI(4)P, and PI did not increase GIRK2 activity (Fig. 5, b and c). However, we found that application of PI(5)P alone activates GIRK2 channels (Fig. 5 c). To

quantify these changes, we measured the steady-state flux and normalized to the maximal response with PI(4,5)P_2. Indeed, PI(5)P significantly enhanced GIRK2 activity (Fig. 5 c). These data demonstrate that the two phosphates in the 4′ and 5′ position of PIP_2 are necessary for complete channel activation but that the 5′-PO_4 of PIP_2 is sufficient to partially activate GIRK2 channels.

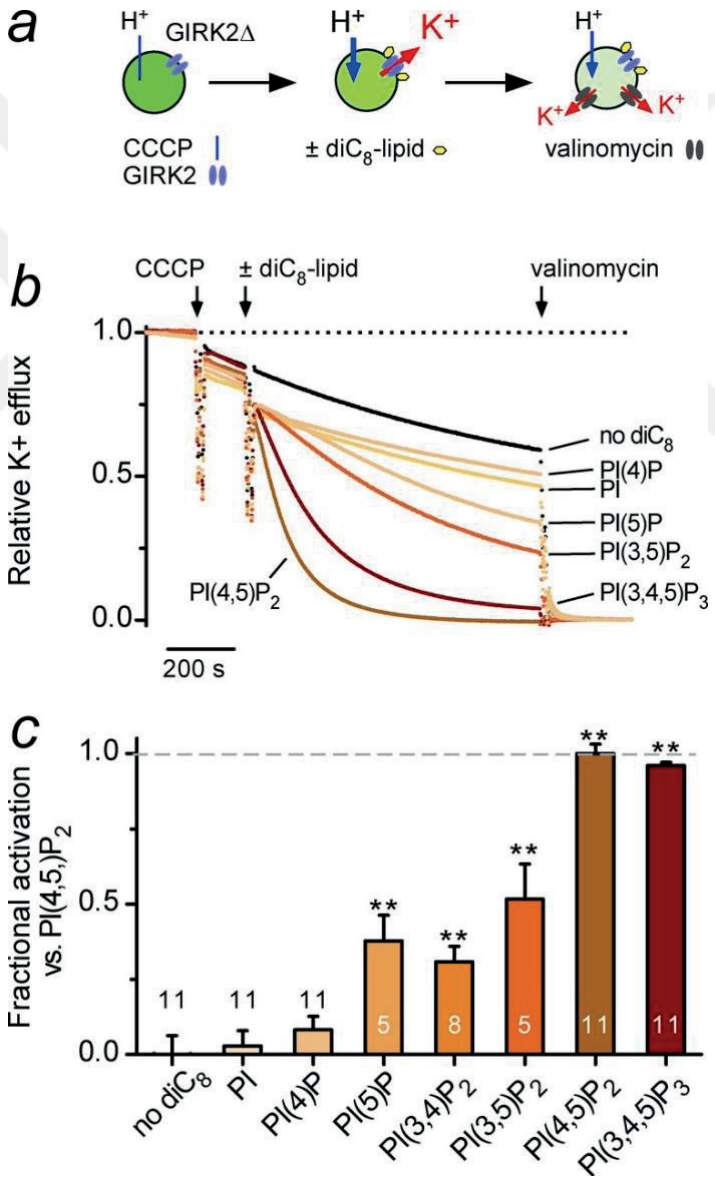

Fig 5 PI(5)P is sufficient to activate GIRK2 channels in proteoliposomes. (a) Cartoon shows design of fluorescence-based K^+ flux assay with GIRK2-containing liposomes. (b) Normalized mean traces of K^+ flux for GIRK2 with acute application of CCCP, 30 µM of the indicated diC_8phosphoinositides (blue), and valinomycin. SEM bars are omitted for clarity. (c) Bar graph

shows steady-state response of each phosphoinositide normalized to the response with $PI(4,5)P_2$ and after subtracting basal flux (e.g., "Fractional activation vs. $PI(4,5)P_2$"). Bars represent mean ± SEM. **, $P < 0.05$ ANOVA with Bonferroni post hoc test versus control (no diC_8). Figure is reproduced from Lacin et al. 2017.

MD simulations reveal conformational changes in the HBC gate

To determine whether PIP_2 channel interactions observed in WT (6'K) and 6'Y channel simulations correlate with gating, we examined the time-dependent changes of PIP_2 in all four PIP_2 pockets at the level of F192 (-2'F), which forms the HBC gate. To quantify the relative association of PIP_2 with all four pockets of the tetrameric channel during the simulation, we calculated the total number of the hydrogen bonds for 0'K–5'-PO_4, 5'K–5'-PO_4, and 6'K–5'-PO_4 and subtracted the number of hydrogen bonds for non-PIP_2 interactions (i.e., 6'K–9'E). This relative PIP_2 association number provides an estimate of the extent of PIP_2interaction, where a high number indicates a stronger 5'-PO_4 interaction within its binding site. Over the 400 ns, the relative PIP_2 association number is ~10 for 6'Y (Fig. 6 a). In contrast, this number decreases toward zero for the WT channel.

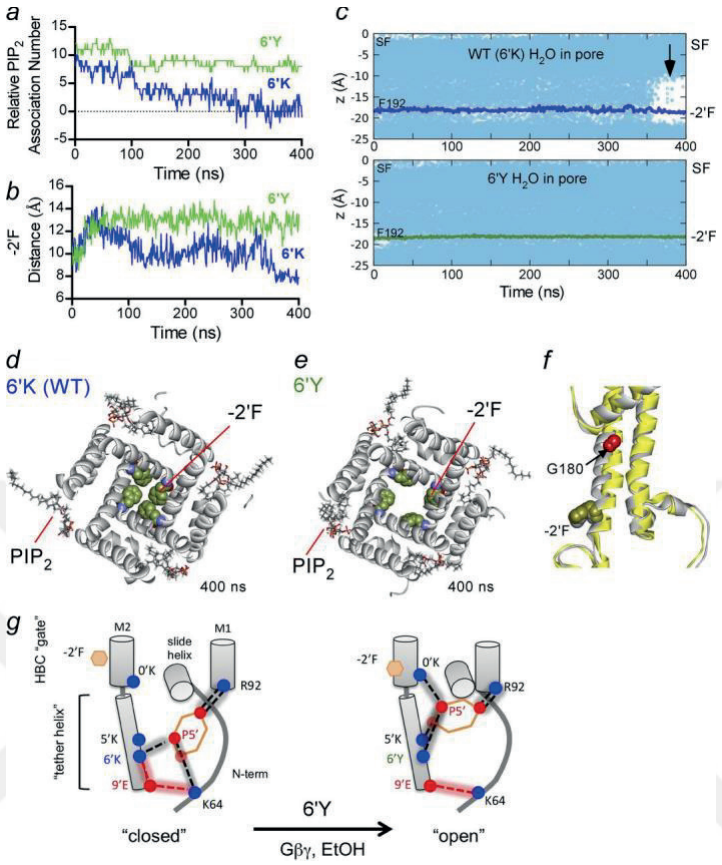

Fig 6 MD simulations of GIRK2 6'Y reveal dynamic opening of the channel at the HBC gate. (a) The relative PIP_2 association number (see Materials and methods) is plotted as a function of simulation time for WT (6'K, blue) and 6'Y (green) channels. (b) The cross-distance diameter of the pore at the HBC, measured between the center of mass of F192 (−2'F) side chain, is plotted as a function of simulation time. (c) The water molecule density in the conduction pathway, moving in the z plane from the selectivity filter (0 Å) to the bottom of the M2 transmembrane domain (approximately −25 Å), is plotted as a function of the simulation time for WT (top) and 6'Y (bottom) channels. Note the loss of water around the region of the −2'F in WT channels (arrow). (d and e) Structural view of the HBC at 400 ns for GIRK2-WT (6'K; d) and GIRK2-6'Y (e). Note how PIP_2 is bound loosely for WT and more tightly for 6'Y. (f) Superimposition of one subunit in 6'K (gray) and 6'Y (yellow) showing movement of M2 relative to G180 in 6'Y (red). (g) Cartoon summarizes hydrogen bond interactions for PIP_2 and GIRK2 for new PIP_2-closed and PIP_2-open conformations based on MD simulations. EtOH, ethanol. Figure is reproduced from Lacin et al. 2017.

To correlate these effects with channel opening, we calculated the mean diameter across the pore at the HBC, F192 (−2'F). For the beginning of the WT 6'K simulation, the diameter at the HBC is ~10 Å and decreases to <8 Å by the end of the simulation (Fig. 6 b).

Coincident with the reduction in the PIP_2association number with WT channels, water density decreases in the pore around the HBC gate (i.e., “dewetting” occurs; [155], consistent with a closed channel (Fig. 6 c, arrow). In contrast, the diameter of 6’Y channel increases from 10 Å to ~13 Å (Fig. 6 b), indicative of an open channel or a channel moving toward an open state. Furthermore, the M2 helix appears to move around G180, a site previously implicated in channel gating [156], in the 6’Y simulations (Fig. 6 f). These differences in the diameter of the pore are readily observed in the cross-sectional view of the channel at the HBC at the end of the 400-ns stimulation (Fig. 6, d and e). Therefore, as the channel transitions from a low to high PIP_2 association number, the gate expands to ~13 Å, and hydration of the pore occurs [155], suggesting an open channel. The increase in water density in the pore around the HBC gate in the 6’Y channel, compared with WT, was also observed in the second 6’Y simulation (Fig. S6). Collectively, the MD simulations of WT-6’K and 6’Y channels reveal dynamic interactions of PIP_2 within its binding pocket that are important for unique PIP_2-dependent gating characteristics of GIRK2 channels.

Discussion

Although it has been known for nearly 20 yr that PIP_2 is required for activation of GIRK channels [124, 148], the structural details of how the association of PIP_2 with GIRK channels leads to channel activation remain poorly described. The initial crystal structures of Kir2.2 and GIRK2 channels provided snapshots of how PIP_2 binds to Kir channels, implicating positively charged, basic amino acids in the tether helix, the M2 TMD, and the N-terminal domain in the binding of one PIP_2 molecule [133-135]. Indeed, a comparison of the amino acids in the tether helix among different Kir channels reveals a high degree of conservation among these basic

residues (Fig. S1 a). However, atomic resolution structures are static and lack the dynamic interactions of ligands associating with the channel and inducing gating conformations. In the current study, we combined functional studies with MD simulations to provide evidence for a dynamic balance of hydrogen bonds between the channel and PIP_2, with the 6'K in the tether helix serving a unique role in regulating gating by PIP_2.

Previous functional studies and mutagenesis experiments revealed some of the first clues on the mechanism of PIP_2-dependent gating of Kir channels. Comparing the rates of current rundown while depleting PIP_2 revealed two important features of PIP_2-Kir gating. First, Kir channels differ in their apparent affinity for PIP_2, whereby GIRK channels exhibit an apparent PIP_2 affinity that is significantly lower than that for Kir2 channels [124, 148]. Second, the apparent affinity of GIRK channels for PIP_2 increases in the presence of Gβγ subunits [124] or alcohol [127]. Hypothesizing that negatively charged phosphates on PIP_2associate with positively charged basic residues in the channel, Lopes et al. systematically mutated basic residues in Kir2.1 and studied the effect of PIP_2antagonists (e.g., anti-PIP_2 antibody or polylysine) on current levels. In the tether helix of Kir2.1, mutation of K188 to Cys (6'C) significantly reduced the association with PIP_2 [131]. Modification of the 6'C with MTSEA, however, restored the inward current and PIP_2 sensitivity, suggesting modification with the partial charge was sufficient to support gating. The 6'Q substitution, on the other hand, did not produce a functionally conducting channel [131]. Similarly, Soom et al. demonstrated that a 6'Q in Kir2.1 reduced the currents and PIP_2 binding [130]. Together, these results suggest that the positive charge at the 6'K position is important for coordinating PIP_2 in Kir2.1.

In contrast, we find that positive charge at the 6' amino acid in the tether helix is not essential for PIP_2-dependent gating. Chemical modification with MTS-HE, MTS-F, and MTS-Y all increased the basal current. Furthermore, the conservative Arg substitution at the 6'K produced little change in the basal current in contrast to the Tyr substitution, which significantly enhanced the basal current. In addition, the 6'Y in GIRK2 appeared to increase the relative affinity for PIP_2, primarily affecting the recovery rate after PIP_2 depletion. Consistent with this finding, a glutamine substitution in Kir1.1 at K187 (6'Q) also appeared to strengthen the PIP_2 interaction, whereas the neighboring 7'Q substitution (R188Q) dramatically reduced PIP_2 association [157]. Collectively, these findings raise the possibility that 6'K serves a unique role in GIRK2 as compared with that in Kir2.1 channels. Other differences exist between Kir2 and GIRK channels. Kir2 channels possess a secondary anionic phospholipid-binding site, which is absent in GIRK channels [157]. Lastly, the cytoplasmic domain in the apo structure of Kir2.2 (i.e., no PIP_2) is not engaged with the TMDs, whereas it remains fully engaged in the apo GIRK2 structure [134, 135, 158].

In the atomic resolution structures of GIRK2-PIP_2 and GIRK2-PIP_2/Gβγ, which are proposed to be in a closed and preopen conformation, respectively, the 6'K forms a hydrogen bond with the 5'-PO_4 of PIP_2 in both structures[133, 134]. Similarly, MD simulations with KirBac3.1/GIRK1 channels showed that 5'K and the 6'K strongly interact with PIP_2 in both the constricted and dilated forms [156]. Together, these studies suggest the electrostatic association of 6'K with the negatively charged phosphate may have a more complex role than simply stabilizing PIP_2 in the pocket. Our MD simulations confirmed that the 6'K (WT) forms hydrogen bonds with the 5'-PO_4, but they also revealed that this interaction is dynamic. When

the 6'K side chain points toward the TMDs (Fig. 6 g), the 5'-PO_4 of PIP_2 hydrogen bonds more tightly with 0'K and 5'K. Based on the functional studies of 6'Y mutation in GIRK2, which showed increased basal current and stronger interaction with PIP_2, we also performed MD simulations with the 6'Y channel. Here, 6'Y stabilizes this upward orientation, increasing the probability of hydrogen bond formation for the 0'K and 5'K with the 5'-PO_4 while decreasing the probability of hydrogen bond formation between K64 and the 5'-PO_4 of PIP_2. The movement of 6'K toward the cytoplasm and its subsequent interaction with E203 (9'E) may destabilize the interaction of 0'K and 5'K with the 5'-PO_4 of PIP_2, leading to closure of the HBC gate (Fig. 6 g) and perhaps explaining the low open channel probability for GIRK channels. K64 in the N-terminal domain may also contribute to PIP_2-dependent gating of GIRK channels by hydrogen bonding with 9'E. It is possible GIRK channel activators, like Gβγ and ethanol, promote the interaction of K64 with 9'E and allow the 5'-PO_4 to engage more strongly with the 0'K (Fig. 6 g). Interestingly, the homologous amino acid in Kir2.2 is a glutamine, supporting a possible unique role for K64 in GIRK channels.

The MD simulations and functional studies also highlight an important role for the 5'-PO_4 of PIP_2 to open GIRK2 channels. Consistent with this, we found that PI(5)P alone is sufficient to partially activate GIRK2 channels in reconstituted bilayers, which contrasts with its lack of effect on Kir2.1 channels [159]. Furthermore, activation of *Dr-Vsp*, which dephosphorylates the 5'-PO_4 of PIP_2 to produce PI(4)P [147], completely inhibits GIRK channel activity. Although PI(5)P is capable of activating, it is not present at high levels in the plasma membrane. Importantly, the MD simulations suggest new PIP_2-bound states that appear to capture a transition state on the path toward opening, an event that appears difficult to observe in any of

the Kir channel crystal structures [133-135]. Recently, Meng et al. successfully modeled an open state of a chimeric GIRK1 channel using an M2-helix mutation, M170P. In these MD simulations, the M1 and M2 helices rotate counterclockwise, with a significant bending at G169, leading to a widening of the pore at the HBC gate (−2'F) that is sufficient to support K^+ permeation [160]. Interestingly, the binding mode of PIP_2 did not change between the M170P-dilated and WT simulations. With the 6'Y MD simulations, however, we observe a similar movement of the M2 helix near G180, a widening of the HBC, and a tighter interaction of the 5'-PO_4 of PIP_2 with 0'K and 5'K of the channel. Additional mutagenesis experiments will be needed to fully validate this MD model of an open channel.

In conclusion, our experiments demonstrate that the highly conserved positive charge of the 6'K in GIRK2 supports a dynamic interaction with PIP_2 that reduces the likelihood of channel opening in the absence of other activators (e.g., Gβγ or ethanol). This model may explain the intrinsically low open probability of GIRK channels and perhaps how the direct binding of physiologically relevant activators, such as Gβγ or ethanol, can modify these interactions to produce robust channel activation. It will be interesting to determine whether any particular features of this mechanism are involved in the regulation of channel activity in other types of Kir channel or whether this remains unique to the GIRK family.

References

1. van den Pol, A.N., *Neuropeptide transmission in brain circuits.* Neuron, 2012. **76**(1): p. 98-115.
2. Baraban, S.C. and M.K. Tallent, *Interneuron Diversity series: Interneuronal neuropeptides--endogenous regulators of neuronal excitability.* Trends Neurosci, 2004. **27**(3): p. 135-42.
3. Sossin, W.S., J.M. Fisher, and R.H. Scheller, *Cellular and molecular biology of neuropeptide processing and packaging.* Neuron, 1989. **2**(5): p. 1407-17.
4. Barkus, R.V., et al., *Identification of an axonal kinesin-3 motor for fast anterograde vesicle transport that facilitates retrograde transport of neuropeptides.* Mol Biol Cell, 2008. **19**(1): p. 274-83.
5. Morris, J.F. and D.V. Pow, *Widespread release of peptides in the central nervous system: quantitation of tannic acid-captured exocytoses.* Anat Rec, 1991. **231**(4): p. 437-45.
6. Chefer, V.I., et al., *Overview of brain microdialysis.* Curr Protoc Neurosci, 2009. **Chapter 7**: p. Unit7 1.
7. Nguyen, Q.T., et al., *An in vivo biosensor for neurotransmitter release and in situ receptor activity.* Nat Neurosci, 2010. **13**(1): p. 127-32.
8. Muller, A., et al., *Cell-based reporters reveal in vivo dynamics of dopamine and norepinephrine release in murine cortex.* Nat Methods, 2014. **11**(12): p. 1245-52.
9. Lacin, E., et al., *Construction of Cell-based Neurotransmitter Fluorescent Engineered Reporters (CNiFERs) for Optical Detection of Neurotransmitters In Vivo.* J Vis Exp, 2016. (111): p. .
10. Berridge, M.J., *The Inositol Trisphosphate/Calcium Signaling Pathway in Health and Disease.* Physiol Rev, 2016. **96**(4): p. 1261-96.
11. Russo, A.F., *Overview of Neuropeptides: Awakening the Senses?* Headache, 2017. **57 Suppl 2**: p. 37-46.
12. Rudy, B., et al., *Three groups of interneurons account for nearly 100% of neocortical GABAergic neurons.* Dev Neurobiol, 2011. **71**(1): p. 45-61.
13. Patel, Y.C., *Somatostatin and its receptor family.* Front Neuroendocrinol, 1999. **20**(3): p. 157-98.
14. Bruno, J.F., et al., *Tissue distribution of somatostatin receptor subtype messenger ribonucleic acid in the rat.* Endocrinology, 1993. **133**(6): p. 2561-7.
15. Tallent, M.K. and G.R. Siggins, *Somatostatin acts in CA1 and CA3 to reduce hippocampal epileptiform activity.* J Neurophysiol, 1999. **81**(4): p. 1626-35.
16. Scharfman, H.E. and P.A. Schwartzkroin, *Selective depression of GABA-mediated IPSPs by somatostatin in area CA1 of rabbit hippocampal slices.* Brain Res, 1989. **493**(2): p. 205-11.
17. Pittman, Q.J. and G.R. Siggins, *Somatostatin hyperpolarizes hippocampal pyramidal cells in vitro.* Brain Res, 1981. **221**(2): p. 402-8.
18. Moore, S.D., et al., *Somatostatin augments the M-current in hippocampal neurons.* Science, 1988. **239**(4837): p. 278-80.

19. Schweitzer, P., S.G. Madamba, and G.R. Siggins, *Somatostatin increases a voltage-insensitive K+ conductance in rat CA1 hippocampal neurons.* J Neurophysiol, 1998. **79**(3): p. 1230-8.
20. Baratta, M.V., T. Lamp, and M.K. Tallent, *Somatostatin depresses long-term potentiation and Ca2+ signaling in mouse dentate gyrus.* J Neurophysiol, 2002. **88**(6): p. 3078-86.
21. Sun, Q.Q., J.R. Huguenard, and D.A. Prince, *Somatostatin inhibits thalamic network oscillations in vitro: actions on the GABAergic neurons of the reticular nucleus.* J Neurosci, 2002. **22**(13): p. 5374-86.
22. Kits, K.S. and H.D. Mansvelder, *Regulation of exocytosis in neuroendocrine cells: spatial organization of channels and vesicles, stimulus-secretion coupling, calcium buffers and modulation.* Brain Res Brain Res Rev, 2000. **33**(1): p. 78-94.
23. Ludwig, M., et al., *Intracellular calcium stores regulate activity-dependent neuropeptide release from dendrites.* Nature, 2002. **418**(6893): p. 85-9.
24. Gamse, R., et al., *Release of immunoreactive somatostatin from hypothalamic cells in culture: inhibition by gamma-aminobutyric acid.* Proc Natl Acad Sci U S A, 1980. **77**(9): p. 5552-6.
25. Fontana, G., et al., *Characterization of the glutamate receptors mediating release of somatostatin from cultured hippocampal neurons.* J Neurochem, 1996. **66**(1): p. 161-8.
26. Tapia-Arancibia, L. and H. Astier, *Actions of excitatory amino acids on somatostatin release from cortical neurons in primary cultures.* J Neurochem, 1989. **53**(4): p. 1134-41.
27. Barg, S., et al., *Delay between fusion pore opening and peptide release from large dense-core vesicles in neuroendocrine cells.* Neuron, 2002. **33**(2): p. 287-99.
28. Diamond, J.S., *Deriving the glutamate clearance time course from transporter currents in CA1 hippocampal astrocytes: transmitter uptake gets faster during development.* J Neurosci, 2005. **25**(11): p. 2906-16.
29. Ginsburg, M. and M.W. Smith, *The fate of oxytocin in male and female rats.* Br J Pharmacol Chemother, 1959. **14**: p. 327-33.
30. Mens, W.B., A. Witter, and T.B. van Wimersma Greidanus, *Penetration of neurohypophyseal hormones from plasma into cerebrospinal fluid (CSF): half-times of disappearance of these neuropeptides from CSF.* Brain Res, 1983. **262**(1): p. 143-9.
31. Reichlin, S., *Somatostatin.* N Engl J Med, 1983. **309**(24): p. 1495-501.
32. Gonchar, Y. and A. Burkhalter, *Three distinct families of GABAergic neurons in rat visual cortex.* Cereb Cortex, 1997. **7**(4): p. 347-58.
33. Somogyi, P., et al., *Different populations of GABAergic neurons in the visual cortex and hippocampus of cat contain somatostatin- or cholecystokinin-immunoreactive material.* J Neurosci, 1984. **4**(10): p. 2590-603.
34. Markram, H., et al., *Interneurons of the neocortical inhibitory system.* Nat Rev Neurosci, 2004. **5**(10): p. 793-807.
35. Dun, N.J., et al., *Colocalization of nitric oxide synthase and somatostatin immunoreactivity in rat dentate hilar neurons.* Proc Natl Acad Sci U S A, 1994. **91**(8): p. 2955-9.
36. de Lecea, L., et al., *Cortistatin is expressed in a distinct subset of cortical interneurons.* J Neurosci, 1997. **17**(15): p. 5868-80.

37. Gonchar, Y., Q. Wang, and A. Burkhalter, *Multiple distinct subtypes of GABAergic neurons in mouse visual cortex identified by triple immunostaining.* Front Neuroanat, 2007. **1**: p. 3.
38. Millhorn, D.E., et al., *Somatostatin- and enkephalin-like immunoreactivities are frequently colocalized in neurons in the caudal brain stem of rat.* Exp Brain Res, 1987. **67**(2): p. 420-8.
39. McDonald, A.J. and F. Mascagni, *Immunohistochemical characterization of somatostatin containing interneurons in the rat basolateral amygdala.* Brain Res, 2002. **943**(2): p. 237-44.
40. Ma, Y., et al., *Distinct subtypes of somatostatin-containing neocortical interneurons revealed in transgenic mice.* J Neurosci, 2006. **26**(19): p. 5069-82.
41. Oliva, A.A., Jr., et al., *Novel hippocampal interneuronal subtypes identified using transgenic mice that express green fluorescent protein in GABAergic interneurons.* J Neurosci, 2000. **20**(9): p. 3354-68.
42. Munoz, W., R. Tremblay, and B. Rudy, *Channelrhodopsin-assisted patching: in vivo recording of genetically and morphologically identified neurons throughout the brain.* Cell Rep, 2014. **9**(6): p. 2304-16.
43. Munoz, W., et al., *Layer-specific modulation of neocortical dendritic inhibition during active wakefulness.* Science, 2017. **355**(6328): p. 954-959.
44. Nigro, M.J., Y. Hashikawa-Yamasaki, and B. Rudy, *Diversity and Connectivity of Layer 5 Somatostatin-Expressing Interneurons in the Mouse Barrel Cortex.* J Neurosci, 2018. **38**(7): p. 1622-1633.
45. Wang, Y., et al., *Anatomical, physiological and molecular properties of Martinotti cells in the somatosensory cortex of the juvenile rat.* J Physiol, 2004. **561**(Pt 1): p. 65-90.
46. Levy, R.B. and A.D. Reyes, *Spatial profile of excitatory and inhibitory synaptic connectivity in mouse primary auditory cortex.* J Neurosci, 2012. **32**(16): p. 5609-19.
47. Pala, A. and C.C.H. Petersen, *In vivo measurement of cell-type-specific synaptic connectivity and synaptic transmission in layer 2/3 mouse barrel cortex.* Neuron, 2015. **85**(1): p. 68-75.
48. Xu, H., et al., *Neocortical somatostatin-expressing GABAergic interneurons disinhibit the thalamorecipient layer 4.* Neuron, 2013. **77**(1): p. 155-67.
49. Pfeffer, C.K., et al., *Inhibition of inhibition in visual cortex: the logic of connections between molecularly distinct interneurons.* Nat Neurosci, 2013. **16**(8): p. 1068-76.
50. Gibson, J.R., M. Beierlein, and B.W. Connors, *Two networks of electrically coupled inhibitory neurons in neocortex.* Nature, 1999. **402**(6757): p. 75-9.
51. Gentet, L.J., et al., *Unique functional properties of somatostatin-expressing GABAergic neurons in mouse barrel cortex.* Nat Neurosci, 2012. **15**(4): p. 607-12.
52. Yu, J., et al., *Principles Governing the Dynamics of GABAergic Interneurons in the Barrel Cortex.* bioRxiv, 2019: p. 554949.
53. Kapfer, C., et al., *Supralinear increase of recurrent inhibition during sparse activity in the somatosensory cortex.* Nat Neurosci, 2007. **10**(6): p. 743-53.
54. Kwan, A.C. and Y. Dan, *Dissection of cortical microcircuits by single-neuron stimulation in vivo.* Curr Biol, 2012. **22**(16): p. 1459-67.

55. Lee, S., et al., *A disinhibitory circuit mediates motor integration in the somatosensory cortex.* Nat Neurosci, 2013. **16**(11): p. 1662-70.
56. Pi, H.J., et al., *Cortical interneurons that specialize in disinhibitory control.* Nature, 2013. **503**(7477): p. 521-4.
57. Fanselow, E.E., K.A. Richardson, and B.W. Connors, *Selective, state-dependent activation of somatostatin-expressing inhibitory interneurons in mouse neocortex.* J Neurophysiol, 2008. **100**(5): p. 2640-52.
58. Kawaguchi, Y., *Selective cholinergic modulation of cortical GABAergic cell subtypes.* J Neurophysiol, 1997. **78**(3): p. 1743-7.
59. Kawaguchi, Y. and T. Shindou, *Noradrenergic excitation and inhibition of GABAergic cell types in rat frontal cortex.* J Neurosci, 1998. **18**(17): p. 6963-76.
60. Scharfman, H.E., *The neurobiology of epilepsy.* Curr Neurol Neurosci Rep, 2007. **7**(4): p. 348-54.
61. Cobos, I., et al., *Mice lacking Dlx1 show subtype-specific loss of interneurons, reduced inhibition and epilepsy.* Nat Neurosci, 2005. **8**(8): p. 1059-68.
62. Tai, C., et al., *Impaired excitability of somatostatin- and parvalbumin-expressing cortical interneurons in a mouse model of Dravet syndrome.* Proc Natl Acad Sci U S A, 2014. **111**(30): p. E3139-48.
63. Vezzani, A., et al., *A peptidase-resistant cyclic octapeptide analogue of somatostatin (SMS 201-995) modulates seizures induced by quinolinic and kainic acids differently in the rat hippocampus.* Neuropharmacology, 1991. **30**(4): p. 345-52.
64. Conklin, B.R., et al., *Substitution of three amino acids switches receptor specificity of Gq alpha to that of Gi alpha.* Nature, 1993. **363**(6426): p. 274-6.
65. Patel, Y.C., et al., *All five cloned human somatostatin receptors (hSSTR1-5) are functionally coupled to adenylyl cyclase.* Biochem Biophys Res Commun, 1994. **198**(2): p. 605-12.
66. Grienberger, C. and A. Konnerth, *Imaging calcium in neurons.* Neuron, 2012. **73**(5): p. 862-85.
67. Mank, M., et al., *A genetically encoded calcium indicator for chronic in vivo two-photon imaging.* Nat Methods, 2008. **5**(9): p. 805-11.
68. Thestrup, T., et al., *Optimized ratiometric calcium sensors for functional in vivo imaging of neurons and T lymphocytes.* Nat Methods, 2014. **11**(2): p. 175-82.
69. Lutcke, H., et al., *Optical recording of neuronal activity with a genetically-encoded calcium indicator in anesthetized and freely moving mice.* Front Neural Circuits, 2010. **4**: p. 9.
70. Atwood, B.K., et al., *Expression of G protein-coupled receptors and related proteins in HEK293, AtT20, BV2, and N18 cell lines as revealed by microarray analysis.* BMC Genomics, 2011. **12**: p. 14.
71. von Engelhardt, J., et al., *Functional characterization of intrinsic cholinergic interneurons in the cortex.* J Neurosci, 2007. **27**(21): p. 5633-42.
72. Gallopin, T., et al., *Cortical sources of CRF, NKB, and CCK and their effects on pyramidal cells in the neocortex.* Cereb Cortex, 2006. **16**(10): p. 1440-52.
73. Fields, R.D., *Nonsynaptic and nonvesicular ATP release from neurons and relevance to neuron-glia signaling.* Semin Cell Dev Biol, 2011. **22**(2): p. 214-9.

74. Hipkin, R.W., et al., *Agonist-induced desensitization, internalization, and phosphorylation of the sst2A somatostatin receptor.* J Biol Chem, 1997. **272**(21): p. 13869-76.
75. Coplan, J.D., et al., *Cerebrospinal fluid concentrations of somatostatin and biogenic amines in grown primates reared by mothers exposed to manipulated foraging conditions.* Arch Gen Psychiatry, 1998. **55**(5): p. 473-7.
76. Svoboda, K. and R. Yasuda, *Principles of two-photon excitation microscopy and its applications to neuroscience.* Neuron, 2006. **50**(6): p. 823-39.
77. Ooi, A., et al., *A Guide to Transient Expression of Membrane Proteins in HEK-293 Cells for Functional Characterization.* Front Physiol, 2016. **7**: p. 300.
78. Shetzline, M.A., et al., *Vasoactive intestinal polypeptide type-1 receptor regulation. Desensitization, phosphorylation, and sequestration.* J Biol Chem, 2002. **277**(28): p. 25519-26.
79. Lang, S., et al., *Somatostatin concentrations in cerebrospinal fluid and brain tissue of patients with refractory epilepsy.* Mol Chem Neuropathol, 1992. **17**(3): p. 239-47.
80. Kao, Y.J., M. Ghosh, and A. Schonbrunn, *Ligand-dependent mechanisms of sst2A receptor trafficking: role of site-specific phosphorylation and receptor activation in the actions of biased somatostatin agonists.* Mol Endocrinol, 2011. **25**(6): p. 1040-54.
81. Ghosh, M. and A. Schonbrunn, *Differential temporal and spatial regulation of somatostatin receptor phosphorylation and dephosphorylation.* J Biol Chem, 2011. **286**(15): p. 13561-73.
82. Funk, C.M., et al., *Role of Somatostatin-Positive Cortical Interneurons in the Generation of Sleep Slow Waves.* J Neurosci, 2017. **37**(38): p. 9132-9148.
83. Arnold, M.A., et al., *Temporal patterns of somatostatin immunoreactivity in the cerebrospinal fluid of the rhesus monkey: effect of environmental lighting.* J Neurosci, 1982. **2**(6): p. 674-80.
84. Berelowitz, M., et al., *The diurnal variation of immunoreactive thyrotropin-releasing hormone and somatostatin in the cerebrospinal fluid of the rhesus monkey.* Endocrinology, 1981. **109**(6): p. 2102-9.
85. Bouabe, H. and K. Okkenhaug, *Gene targeting in mice: a review.* Methods Mol Biol, 2013. **1064**: p. 315-36.
86. Madisen, L., et al., *A toolbox of Cre-dependent optogenetic transgenic mice for light-induced activation and silencing.* Nat Neurosci, 2012. **15**(5): p. 793-802.
87. Taniguchi, H., et al., *A resource of Cre driver lines for genetic targeting of GABAergic neurons in cerebral cortex.* Neuron, 2011. **71**(6): p. 995-1013.
88. Viollet, C., et al., *Somatostatin-IRES-Cre Mice: Between Knockout and Wild-Type?* Front Endocrinol (Lausanne), 2017. **8**: p. 131.
89. Lin, J.Y., *A user's guide to channelrhodopsin variants: features, limitations and future developments.* Exp Physiol, 2011. **96**(1): p. 19-25.
90. Berndt, A., et al., *High-efficiency channelrhodopsins for fast neuronal stimulation at low light levels.* Proc Natl Acad Sci U S A, 2011. **108**(18): p. 7595-600.
91. Adesnik, H., et al., *A neural circuit for spatial summation in visual cortex.* Nature, 2012. **490**(7419): p. 226-31.

92. Ting, J.T. and G. Feng, *Development of transgenic animals for optogenetic manipulation of mammalian nervous system function: progress and prospects for behavioral neuroscience.* Behav Brain Res, 2013. **255**: p. 3-18.
93. Chen, N., H. Sugihara, and M. Sur, *An acetylcholine-activated microcircuit drives temporal dynamics of cortical activity.* Nat Neurosci, 2015. **18**(6): p. 892-902.
94. Porter, J.T., et al., *Selective excitation of subtypes of neocortical interneurons by nicotinic receptors.* J Neurosci, 1999. **19**(13): p. 5228-35.
95. Poorthuis, R.B., L. Enke, and J.J. Letzkus, *Cholinergic circuit modulation through differential recruitment of neocortical interneuron types during behaviour.* J Physiol, 2014. **592**(19): p. 4155-64.
96. Fu, Y., et al., *A cortical circuit for gain control by behavioral state.* Cell, 2014. **156**(6): p. 1139-1152.
97. Feniuk, W., et al., *Selective somatostatin sst(2) receptor blockade with the novel cyclic octapeptide, CYN-154806.* Neuropharmacology, 2000. **39**(8): p. 1443-50.
98. Akerboom, J., et al., *Genetically encoded calcium indicators for multi-color neural activity imaging and combination with optogenetics.* Front Mol Neurosci, 2013. **6**: p. 2.
99. Bethge, P., et al., *An R-CaMP1.07 reporter mouse for cell-type-specific expression of a sensitive red fluorescent calcium indicator.* PLoS One, 2017. **12**(6): p. e0179460.
100. Silberberg, G. and H. Markram, *Disynaptic inhibition between neocortical pyramidal cells mediated by Martinotti cells.* Neuron, 2007. **53**(5): p. 735-46.
101. Obermayer, J., et al., *Lateral inhibition by Martinotti interneurons is facilitated by cholinergic inputs in human and mouse neocortex.* Nat Commun, 2018. **9**(1): p. 4101.
102. de Lanerolle, N.C., et al., *Hippocampal interneuron loss and plasticity in human temporal lobe epilepsy.* Brain Res, 1989. **495**(2): p. 387-95.
103. Buckmaster, P.S. and F.E. Dudek, *Neuron loss, granule cell axon reorganization, and functional changes in the dentate gyrus of epileptic kainate-treated rats.* J Comp Neurol, 1997. **385**(3): p. 385-404.
104. Tallent, M.K. and C. Qiu, *Somatostatin: an endogenous antiepileptic.* Mol Cell Endocrinol, 2008. **286**(1-2): p. 96-103.
105. Zhang, W., et al., *Surviving hilar somatostatin interneurons enlarge, sprout axons, and form new synapses with granule cells in a mouse model of temporal lobe epilepsy.* J Neurosci, 2009. **29**(45): p. 14247-56.
106. Halabisky, B., et al., *Excitatory input onto hilar somatostatin interneurons is increased in a chronic model of epilepsy.* J Neurophysiol, 2010. **104**(4): p. 2214-23.
107. Kobayashi, M. and P.S. Buckmaster, *Reduced inhibition of dentate granule cells in a model of temporal lobe epilepsy.* J Neurosci, 2003. **23**(6): p. 2440-52.
108. Sun, C., et al., *Selective loss of dentate hilar interneurons contributes to reduced synaptic inhibition of granule cells in an electrical stimulation-based animal model of temporal lobe epilepsy.* J Comp Neurol, 2007. **500**(5): p. 876-93.
109. Marti, M., et al., *Somatostatin release in the hippocampus in the kindling model of epilepsy: a microdialysis study.* J Neurochem, 2000. **74**(6): p. 2497-503.
110. Wanscher, B., et al., *Increased somatostatin and enkephalin-like immunoreactivity in the rat hippocampus following hippocampal kindling.* Neurosci Lett, 1990. **118**(1): p. 33-6.

111. Luscher, C. and P.A. Slesinger, *Emerging roles for G protein-gated inwardly rectifying potassium (GIRK) channels in health and disease.* Nat Rev Neurosci, 2010. **11**(5): p. 301-15.
112. Mayfield, J., Y.A. Blednov, and R.A. Harris, *Behavioral and Genetic Evidence for GIRK Channels in the CNS: Role in Physiology, Pathophysiology, and Drug Addiction.* Int Rev Neurobiol, 2015. **123**: p. 279-313.
113. Ehrengruber, M.U., et al., *Activation of heteromeric G protein-gated inward rectifier K+ channels overexpressed by adenovirus gene transfer inhibits the excitability of hippocampal neurons.* Proc Natl Acad Sci U S A, 1997. **94**(13): p. 7070-5.
114. Luscher, C., et al., *G protein-coupled inwardly rectifying K+ channels (GIRKs) mediate postsynaptic but not presynaptic transmitter actions in hippocampal neurons.* Neuron, 1997. **19**(3): p. 687-95.
115. Scanziani, M., *GABA spillover activates postsynaptic GABA(B) receptors to control rhythmic hippocampal activity.* Neuron, 2000. **25**(3): p. 673-81.
116. Wiser, O., et al., *Modulation of basal and receptor-induced GIRK potassium channel activity and neuronal excitability by the mammalian PINS homolog LGN.* Neuron, 2006. **50**(4): p. 561-73.
117. Lujan, R., J. Maylie, and J.P. Adelman, *New sites of action for GIRK and SK channels.* Nat Rev Neurosci, 2009. **10**(7): p. 475-80.
118. Logothetis, D.E., et al., *The beta gamma subunits of GTP-binding proteins activate the muscarinic K+ channel in heart.* Nature, 1987. **325**(6102): p. 321-6.
119. Reuveny, E., et al., *Activation of the cloned muscarinic potassium channel by G protein beta gamma subunits.* Nature, 1994. **370**(6485): p. 143-6.
120. Wickman, K.D., et al., *Recombinant G-protein beta gamma-subunits activate the muscarinic-gated atrial potassium channel.* Nature, 1994. **368**(6468): p. 255-7.
121. Lesage, F., et al., *Molecular properties of neuronal G-protein-activated inwardly rectifying K+ channels.* J Biol Chem, 1995. **270**(48): p. 28660-7.
122. Inanobe, A., et al., *Molecular cloning and characterization of a novel splicing variant of the Kir3.2 subunit predominantly expressed in mouse testis.* J Physiol, 1999. **521 Pt 1**: p. 19-30.
123. Wickman, K., et al., *Brain localization and behavioral impact of the G-protein-gated K+ channel subunit GIRK4.* J Neurosci, 2000. **20**(15): p. 5608-15.
124. Huang, C.L., S. Feng, and D.W. Hilgemann, *Direct activation of inward rectifier potassium channels by PIP2 and its stabilization by Gbetagamma.* Nature, 1998. **391**(6669): p. 803-6.
125. Hibino, H., et al., *Inwardly rectifying potassium channels: their structure, function, and physiological roles.* Physiol Rev, 2010. **90**(1): p. 291-366.
126. Petit-Jacques, J., J.L. Sui, and D.E. Logothetis, *Synergistic activation of G protein-gated inwardly rectifying potassium channels by the betagamma subunits of G proteins and Na(+) and Mg(2+) ions.* J Gen Physiol, 1999. **114**(5): p. 673-84.
127. Bodhinathan, K. and P.A. Slesinger, *Molecular mechanism underlying ethanol activation of G-protein-gated inwardly rectifying potassium channels.* Proc Natl Acad Sci U S A, 2013. **110**(45): p. 18309-14.

128. Baukrowitz, T., et al., *PIP2 and PIP as determinants for ATP inhibition of KATP channels.* Science, 1998. **282**(5391): p. 1141-4.
129. Zhang, H., et al., *Activation of inwardly rectifying K+ channels by distinct PtdIns(4,5)P2 interactions.* Nat Cell Biol, 1999. **1**(3): p. 183-8.
130. Soom, M., et al., *Multiple PIP2 binding sites in Kir2.1 inwardly rectifying potassium channels.* FEBS Lett, 2001. **490**(1-2): p. 49-53.
131. Lopes, C.M., et al., *Alterations in conserved Kir channel-PIP2 interactions underlie channelopathies.* Neuron, 2002. **34**(6): p. 933-44.
132. Zhou, W., et al., *Mechanism underlying bupivacaine inhibition of G protein-gated inwardly rectifying K+ channels.* Proc Natl Acad Sci U S A, 2001. **98**(11): p. 6482-7.
133. Whorton, M.R. and R. MacKinnon, *X-ray structure of the mammalian GIRK2-betagamma G-protein complex.* Nature, 2013. **498**(7453): p. 190-7.
134. Whorton, M.R. and R. MacKinnon, *Crystal structure of the mammalian GIRK2 K+ channel and gating regulation by G proteins, PIP2, and sodium.* Cell, 2011. **147**(1): p. 199-208.
135. Hansen, S.B., X. Tao, and R. MacKinnon, *Structural basis of PIP2 activation of the classical inward rectifier K+ channel Kir2.2.* Nature, 2011. **477**(7365): p. 495-8.
136. Brooks, B.R., et al., *CHARMM: the biomolecular simulation program.* J Comput Chem, 2009. **30**(10): p. 1545-614.
137. Wu, E.L., et al., *CHARMM-GUI Membrane Builder toward realistic biological membrane simulations.* J Comput Chem, 2014. **35**(27): p. 1997-2004.
138. Best, R.B., et al., *Optimization of the additive CHARMM all-atom protein force field targeting improved sampling of the backbone phi, psi and side-chain chi(1) and chi(2) dihedral angles.* J Chem Theory Comput, 2012. **8**(9): p. 3257-3273.
139. Jo, S., T. Kim, and W. Im, *Automated builder and database of protein/membrane complexes for molecular dynamics simulations.* PLoS One, 2007. **2**(9): p. e880.
140. Hess, B., et al., *GROMACS 4: Algorithms for Highly Efficient, Load-Balanced, and Scalable Molecular Simulation.* J Chem Theory Comput, 2008. **4**(3): p. 435-47.
141. Humphrey, W., A. Dalke, and K. Schulten, *VMD: visual molecular dynamics.* J Mol Graph, 1996. **14**(1): p. 33-8, 27-8.
142. Glaaser, I.W. and P.A. Slesinger, *Dual activation of neuronal G protein-gated inwardly rectifying potassium (GIRK) channels by cholesterol and alcohol.* Sci Rep, 2017. **7**(1): p. 4592.
143. Guo, Y., G.J. Waldron, and R. Murrell-Lagnado, *A role for the middle C terminus of G-protein-activated inward rectifier potassium channels in regulating gating.* J Biol Chem, 2002. **277**(50): p. 48289-94.
144. Xiao, J., X.G. Zhen, and J. Yang, *Localization of PIP2 activation gate in inward rectifier K+ channels.* Nat Neurosci, 2003. **6**(8): p. 811-8.
145. Aryal, P., et al., *A discrete alcohol pocket involved in GIRK channel activation.* Nat Neurosci, 2009. **12**(8): p. 988-95.
146. Adney, S.K., et al., *A Critical Gating Switch at a Modulatory Site in Neuronal Kir3 Channels.* J Neurosci, 2015. **35**(42): p. 14397-405.
147. Rjasanow, A., et al., *Ion channel regulation by phosphoinositides analyzed with VSPs-PI(4,5)P2 affinity, phosphoinositide selectivity, and PI(4,5)P2 pool accessibility.* Front Pharmacol, 2015. **6**: p. 127.

148. Sui, J.L., J. Petit-Jacques, and D.E. Logothetis, *Activation of the atrial KACh channel by the betagamma subunits of G proteins or intracellular Na+ ions depends on the presence of phosphatidylinositol phosphates.* Proc Natl Acad Sci U S A, 1998. **95**(3): p. 1307-12.
149. Kobayashi, T., et al., *Ethanol opens G-protein-activated inwardly rectifying K+ channels.* Nat Neurosci, 1999. **2**(12): p. 1091-7.
150. Lewohl, J.M., et al., *G-protein-coupled inwardly rectifying potassium channels are targets of alcohol action.* Nat Neurosci, 1999. **2**(12): p. 1084-90.
151. Dai, G., et al., *Osmoregulatory inositol transporter SMIT1 modulates electrical activity by adjusting PI(4,5)P2 levels.* Proc Natl Acad Sci U S A, 2016. **113**(23): p. E3290-9.
152. Hille, B., et al., *Phosphoinositides regulate ion channels.* Biochim Biophys Acta, 2015. **1851**(6): p. 844-56.
153. Ho, I.H. and R.D. Murrell-Lagnado, *Molecular determinants for sodium-dependent activation of G protein-gated K+ channels.* J Biol Chem, 1999. **274**(13): p. 8639-48.
154. Rohacs, T., et al., *Distinct specificities of inwardly rectifying K(+) channels for phosphoinositides.* J Biol Chem, 1999. **274**(51): p. 36065-72.
155. Aryal, P., et al., *A hydrophobic barrier deep within the inner pore of the TWIK-1 K2P potassium channel.* Nat Commun, 2014. **5**: p. 4377.
156. Meng, X.Y., et al., *The molecular mechanism by which PIP(2) opens the intracellular G-loop gate of a Kir3.1 channel.* Biophys J, 2012. **102**(9): p. 2049-59.
157. Lee, C.H., et al., *Non-basic amino acids in the ROMK1 channels via an appropriate distance modulate PIP2 regulated pHi-gating.* Biochem Biophys Res Commun, 2016. **473**(1): p. 303-310.
158. Tao, X., et al., *Crystal structure of the eukaryotic strong inward-rectifier K+ channel Kir2.2 at 3.1 A resolution.* Science, 2009. **326**(5960): p. 1668-74.
159. D'Avanzo, N., et al., *Direct and specific activation of human inward rectifier K+ channels by membrane phosphatidylinositol 4,5-bisphosphate.* J Biol Chem, 2010. **285**(48): p. 37129-32.
160. Meng, X.Y., et al., *The Molecular Mechanism of Opening the Helix Bundle Crossing (HBC) Gate of a Kir Channel.* Sci Rep, 2016. **6**: p. 29399.